PLASMONIC EFFECTS AND OPTICAL PROPERTIES OF CORE-SHELL NANOPARTICLES

By

Garoma Dhaba

A THESIS SUBMITTED TO THE GRADUATE PROGRAMS OF COLLEGE OF NATURAL AND COMPUTATIONAL SCIENCES IN PARTIAL FULFILLMENT OF THE REQUIREMENTS FOR THE DEGREE OF DOCTOR OF PHILOSOPHY IN PHYSICS (CONDENSED MATTER PHYSICS)

AT

ADDIS ABABA UNIVERSITY

ADDIS ABABA, ETHIOPIA

MAY 2023

ADDIS ABABA UNIVERSITY

DEPARTMENT OF PHYSICS

The undersigned hereby certify that they have read and recommend to the Graduate Programs for acceptance a thesis entitled "**Plasmonic Effects and Optical Properties of Core-Shell Nanoparticles**" by **Garoma Dhaba** in partial fulfillment of the requirements for the degree of **Doctor of Philosophy in Physics (Condensed Matter Physics)**.

Dated: May 2023

External Examiner: _____
Dr. Nebiyu Gemechu

Research suppervisors: _____
Dr. Belayneh Mesfin

_____
Dr. Teshome Senbeta

Internal Examiner: _____
Dr. Gashaw Beyene

Chairman: _____
Dr. Desalegn Ayehu

ADDIS ABABA UNIVERSITY

Date: May 2023

Author:	**Garoma Dhaba**		
Title:	**Plasmonic Effects and Optical Properties of Core-Shell Nanoparticles**		
Department:	**Physics**		
Degree:	**PhD**	Convocation: **May**	Year: **2023**

Permission is herewith granted to Addis Ababa University to circulate and to have copied for non-commercial purposes, at its discretion, the above title upon the request of individuals or institutions.

_____

Signature of the Author

Dedication

To the memory of my mother, *Worknesh Sori*, whom I forcibly lost while she was eagerly waiting to celebrate the graduations of her children.

Declaration

I hereby declare that this Thesis is my original work and has not been presented for a degree in any other university. All sources of material used for the thesis have been duly acknowledged.

Garoma Dhaba: _____

Email: *garoma.dhaba@gmail.com*

This thesis has been submitted for examination with our approval as University advisors.

Dr. Belayneh Mesfin: _____

Email: *belayneh.mesfin@aau.edu.et*

Dr. Teshome Senbeta: _____

Email: *teshome.senbeta@aau.edu.et*

Abbreviations and Acronyms

Ag	Silver
Au	Gold
CdSe	Cadmium selenide
EM	Electromagnetic
IR	Ifra-red
LFEF	Local Field Enhancement Factor
LSPRs	Localized Surface Plasmon Resonances
LSPs	Localized Surface Plasmons
NCs	Nanocomposites
NPs	Nanoparticles
ppm	parts per million
PSPs	Propagating Surface Plasmons
QDs	Quantum Dots
SiO_2	Silica or Silicon dioxide
SPPs	Surface Plasmon Polaritons
SPRs	Surface Plasmon Resonances
ZnSe	Zinc selenide

Acknowledgments

Above all, praise be to the Almighty God for all His invaluable support in all seasons of my study.

Then, my firs and for most gratitude goes to my supervisors, Dr. Belyaneh Mesfin and Dr. Teshome Senbeta, for their insightful professional assistance and academic support all through the duration of the study. Their commitment and patience in reading every page of my dissertation several times, their instructive comments and guidance, their follow-ups on my wanderings, their brotherly approach, and their unreserved support in many needed aspects are all unforgettable. I am also thankful to Dr. Chernet Amente and Prof. P. Singh for their advice during my PhD courses.

I would also like to thank Addis Ababa University for funding my research work and letting me pursue my PhD study there, Department of Physics for facilitating my study, and staff members of Department of Physics of the Addis Ababa University. Special thanks go to Ms. Tsilat Adinew, whose support is always sensible and generous when I need it. My gratitude is also deepest to the Oromia Education Bureau and Sebeta Special Needs Education Teachers College for sponsoring my study.

I also express my deep gratitude to my dearest wife, Ms. Abebech Gebisa, for all her patience, courage, and efforts in looking after our children, Heran Garoma, Kena Garoma, and Toran Garoma, when I was completely engaged in this pursuit. Special thanks to my father Mr. Dhaba Bergaga, all my brothers and sisters for all their supports and encouragements.

Finally, I want to acknowledge all my friends and colleagues for their inspirations and encouragements. There are many others whose input is unforgettable.

Contents

List of Figures

List of Tables

List of Publications

1. **Garoma Dhaba**, Belayneh Mesfin, and Teshome Senbeta (2023). *"Effects of shape on the optical properties of CdSe@ Au core-shell nanocomposites." AIP Advances,* 13(3), 035331.

2. **Garoma Dhaba**, Belayneh Mesfin, and Teshome Senbeta (2022). *"Size dependent local field enhancement factor of CdSe based core@ shell spherical nanoparticles." Materials Research Express,* 9(4), 045001.

3. Tolasa Tamasgen, **Garoma Dhaba**, Belayneh Mesfin, and Sisay Shewamare (2023). *"Local field enhancement factor of spheroidal core-shell nanocomposites with passive and active dielectric cores." Materials Research Express,* 10(4), 045005.

Abstract

The applications in the real world require specific sizes, shapes, compositions, and structures. Hence, this dissertation is devoted to the theoretical and numerical investigations of the effects of size, shape, surface plasmons, and host medium on the optical properties of core-shell nanocomposites (NCs).

Under the quasi-static approximation, we employed Laplace's equation and the Drude-Lorentz model for electric potential distributions and dielectric functions, respectively. Then we calculated the local field enhancement factor (LFEF), polarizability, absorption, scattering, and extinction cross sections for spherical, cylindrical, prolate, and oblate core-shell NCs. The study reveals that when the core radius of spherical CdSe@Ag decreases, the resonance peaks of LFEF increase and are red shifted in the inner interface and blue-shifted in the outer interface of the shell. However, whether the shell radius is kept constant or decreased, increasing the core size produces a lower LFEF, showing that the core size is a crucial parameter to change the LFEF of nanoshells. Furthermore, an increase in the size of the core results in an increased resonance peaks of LFEF only in the presence of the spacer (ZnSe) between the core (CdSe) and the shell (Ag), demonstrating that the number of layers and the size of the spacer of core-shell NCs can affect the optical characteristics. When the metal shell thickness increases at a constant core radius, an enhancement in the local field factor is observed due to plasmonic effects.

In addition, out of the four different shapes of CdSe@Au core-shell NCs studied, the LFEF, absorption, and extinction cross sections of the spherical and cylindrical structures possess two peaks, whereas oblate and prolate spheroids show three observable

peaks. Moreover, the spherical and cylindrical core-shell NCs show higher peaks of LFEF and extinction cross sections, respectively. For the same composition, the differences in shapes of core-shell NCs determine the intensity, the number, and the positions of peaks of the LFEF and optical cross sections. The study also indicated that in different shapes of core-shell NCs, the change in the dielectric function of the embedding medium produces LFEF and extinction cross sections of different properties. Our analysis reveals that increasing the magnitude of the permittivity of the embedding medium greatly enhances the LFEF of nanoshells, than does increasing the metallic shell thickness. The possibility of obtaining adjustable LFEF by varying the sizes of the components of the core-shell NCs makes them attractive for applications in nonlinear optics, photocatalysis, and optoelectronics. Furthermore, shape dependent optical properties might be promising for applications in optical detection and bio-sensing. Especially, gold coated core-shell spheroids have good potential uses in multi-channel sensing.

Chapter 1

Introduction

1.1 Nanoparticles

To transform many aspects of human life to the contemporary standards and keep up to date, nanoscience is expected to address the demanding needs by providing new approaches to scientific innovations, education, and governances. Further developments and advancements in medicine, information and communication technologies, materials, cosmetics, industries, military, aerospace, energy, environmental preservation, and water treatment are also being addressed through nanoscience [1, 2]. To achieve all these results, nanoscience uses nanotechnology, which is the manipulation of matter at the nanoscale level [3]. In order to design and synthesize nanodevices and systems with basically new characteristics and functions, nanoscience utilizes nanoparticles [4, 5]. Moreover, the chemical and physical characteristics of materials were seen to undergo significant changes as bulk materials are reduced to nanoparticles [6, 7]. Hence, nanomaterials are the cornerstones of nanoscience and nanotechnology. This being the case, researchers in the discipline have been focusing their attentions on the investigations of nanoparticles.

Nanoparticle is a general term in which “nano” refers to size, and comes from the Greek word "nanos", which means “dwarf ”, and designates a billionth of a unit [8].

Nanoparticles cover a large scope of different types of nanomaterials. In size, they range from around 1 *nm* to 100 *nm* and behave as a whole unit in terms of their transport and properties. This shows that nanoparticle normally includes a cluster of hundreds of thousands of atoms of a total size that does not exceed 100 *nm*. A virus cannot be seen with the help of optical microscopes. However, amazingly, a metal nanoparticle of the same size can be seen by human eye easily. Light imposed on such a nanoparticle causes the conduction of electrons into motion, producing plasmons, which are at the center of the discipline referred to as plasmonics. Depending on the size and shape of the particle, and the particle's immediate environment, the ringing electrons scatter light of a particular colour [9]. Nowadays, nanosized devices which are 1000 times smaller than human cells are being built.

In shape, nanoparticles occur in great varieties such as nanospheres, nanocylinders, nano ellipsoids, nanorods [10], nanowires [11], nanocubes [12], nanoprisms [13], nanostars [14], nanotubes, nanoflowers, nanoreefs [15], nanowhiskers, nanofibers, nanoboxes [16] or even amorphous [17]. In form of existence, they can be colloidal dispersion by sol-gel process, nano-islands on substrate by epitaxy, or functional nanostructures made by multi-step nanofabrication. Moreover, nanoparticles can be produced naturally by cosmological [18], geological [19], meteorological, and biological processes. In configuration, nanoparticles can be homogeneous material throughout the whole structure, or hetero-structured with two materials or more. In materials, they can be produced from metals, metal oxides, semiconductors, dielectrics, non-oxide ceramics, polymers, organics, and biomolecules [20]. Nowadays, atmospheric dusts and a number of interplanetary dusts falling on our planet at a rate of tens of thousands of tons annually, are also in the nanoparticle range [21, 22].

Since prehistory, artisans used nanoparticles. However, they were unaware of the nature of those particles. In the Greco-Roman era, glass makers and potters used nanoparticles as exemplified by the Roman Lycurgus cup of dichroic glass (4^{th} century) [23] and stained glass of church windows (from 5^{th} to 15^{th} century). The Lycurgus cup,

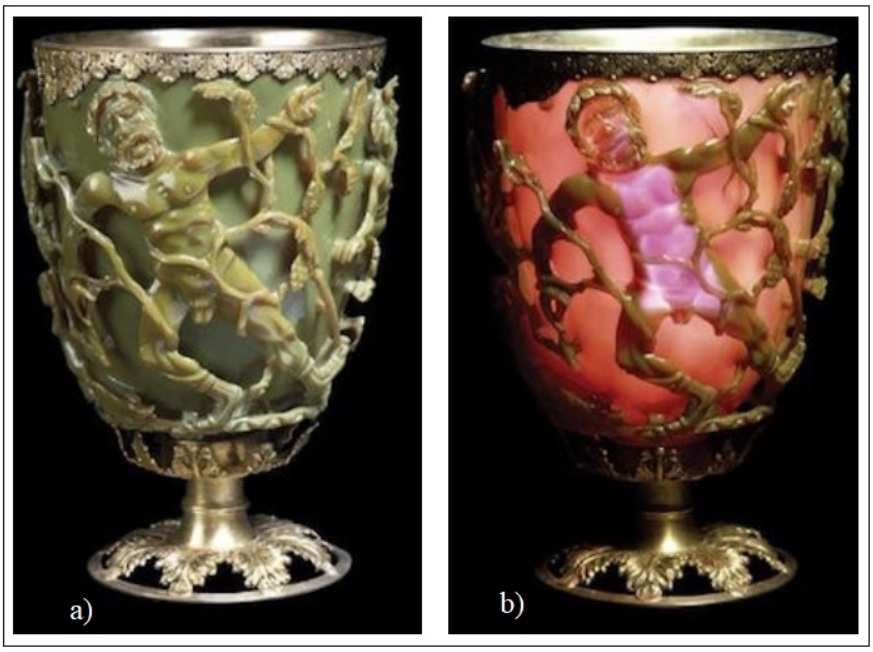

Figure 1.1: The Lycurgus cup seen in: (a) reflected light, green and (b) transmitted light, red [23].

shown in figure 1.1 exhibits various colors under different lighting conditions. It appears green (Fig. 1.1(a)) when light comes from in front of the cup and red (Fig. 1.1(b)) when light comes from behind of the cup. This property stems from the scattering and the absorption of light by embedded gold (40 ppm) and silver (330 ppm) nanoparticles present in the glass [10].

Another example is the stained glass [24]. Almost entirely for the course of its thousand year history, the phrase "stained glass" has been used to describe the windows of churches and other notable religious structures. At the first stage, it has been colored as a material by the addition of metallic salts during its production, and is typically further decorated in numerous ways. The colored glass is made into stained glass windows, where tiny pieces of glass are traditionally arranged to produce designs or pictures and kept together by lead strips. Both artistic and crafty skills are needed to create a suitable and functional design, as well as engineering expertise to put the component together. The purpose of colored glass window is to manage light, not to let people within a building view what's outside. For this reason stained glass windows

have been described as "illuminated wall decorations".

The first scientific investigation of nanoparticles took place in 1857 when Michael Faraday prepared the first pure sample of gold colloid and stated that the red color was because of the small size of these particles. He demonstrated that nanostructured gold

Figure 1.2: Faraday's Au colloid in water [26].

under certain lighting conditions produces different-colored solutions [25, 26]. It was only in 1908 that Gustav Mie formulated the precise expressions for Maxwell's equations and provided a theoretical explanation for the optical behaviour of an arbitrary-sized sphere embedded in a homogeneous material and exposed to a monochromatic plane wave [27].

With his famous talk entitled "*There is Plenty of Room at the Bottom*", Richard Feynman in 1959 gave what is considered to be the first lecture that triggered research at nanoscale level [28]. Recently, this field encompasses nanoscience and nanotechnology. Beginning in the early seventies, theoretical and experimental studies of nanoparticles are initially called "*superfine,*" "*ultrafine,*" "*ultramicroscopic*" or "*very small*" particles [23]. The after, it is generally acknowledged that the term nanotechnology was

first used by the late Professor Norio Taniguchi of the Tokyo Science University in a paper, "On the Basic Concept of 'Nanotechnology'", presented at a meeting of the Japan Society of Precision Engineering in 1974. In this paper, Taniguchi states that "Nano-technology mainly consists of the processing of separation, consolidation and deformation of materials by one atom or one molecule" [29].

Since nanoparticles have been in use, their applications may require specific shapes, sizes or size ranges. They can also incorporate different components to achieve multi-functional capabilities with high biocompatibility, specially in the case of metal nanoparticles. For example, gold nanoparticles can incorporate antibodies for selective imaging and killing cancer cells using visible light (and leaving healthy cells unaffected) [30, 31], whereas silver nanoparticles, due to its bioactive properties, are being applied for developing new biosystems with antibacterial activity [32]. Other biomedical applications of nanoparticles involve biological sequencing, cell labeling [33], hyperthermia [34], drug delivery [35], gene therapy or pharmacokinetic studies.

Among many others, the most important characteristic of nanoparticles is their small size, which results in a higher surface area-to-volume ratio. This enables the nanoparticle's surface atoms to dominate over the interior atoms. Another remarkable feature is that this small size is far less than the wavelength of infra-red and visible light and comparable to the ultraviolet. This phenomenon is important and necessary for confinement of charges and separation of energy levels, thus imparting to the nanoparticles distinctive optical properties that deviate substantially from that of bulk materials. Moreover, the plasmonic effects with metals, the quantum confinement effects with semiconductor nanoparticles (quantum dots), and photothermal effects make nanoparticles strong candidates for numerous applications within the field of optics and related disciplines.

As synthesis and characterization methods have advanced quickly, scientists have discovered that substantially modified characteristics could be possible for core-shell

nanocomposites compared to nanoparticles of single composition. The variety in structure and configuration of core-shell materials could greatly enhance their applications in a variety of disciplines. Due to theirÂăexceptional qualities, including adaptability, tunability, and stability, biocompatibility, and controllability [36–39], core-shell nanomaterials are used in a variety of fields, including optics, healthcare, environmental science, materials, catalysis, energy, and others [40, 41]. Moreover, their most prevalent uses in the area of optics include the development of robust light-emitting diodes and tuning the color of light produced by changing the bandgap of nanomaterial [42]. They can also be used to revitalize the LCD screens in our phones, tablets, TVs, and laptops. As a result, extensive studies have been conducted on core-shell nanomaterials. Since these numerous investigations are producing new properties needed for immense potential applications, there is still an increasing research interest in core-shell nanomaterials.

1.2 Statement of the problem

The interest in studying core-shell nanoparticles has been stimulated by the need to develop nanostructures and nanomaterials with the needed characteristics. These characteristics primarily involve electronic, optical, or magnetic phenomena of the nanoparticles. Core-shell NCs have been known since 1920's [43]. However, the first theoretical investigations were published only in 1951 by Aden and Kerker [44], by extending the optical characteristics of Mie theory for a coated spherical core-shell NCs. The experimental studies on core-shell NCs first appeared in 1964, when Morriss and Collins [45] employed the Aden and Kerker theory on a gold coated with silver. As metal nanoparticles attracted more and more interest, more detailed investigations started late in the 1980's, covering a wide range of core-shell NCs.

Since then, through the fine-tuning of the sizes of cores and shells of nanoparticles, several types of nanomaterials with modified properties have been obtained [46, 47]. These tailored properties are increasingly important in the development of smaller,

cheaper, faster, and more efficient optoelectronic devices. In the structure of core-shell materials, the shell passivates the nonradiative recombination sites of the core surface, improves its optical characteristics, and minimizes the chemical attack. Furthermore, the shell is used to physically separate the core from its external environment. Overcoating also prevents the leakage of core materials thereby reducing the toxicity of quantum dots [48]. Finally, this encapsulation can lead to the strengthening of quantum confinement effect which enables quantum dots reach their higher emission intensity or shift the maximum in the emission spectrum toward longer wavelengths.

For instance, cadmium selenide (CdSe) nanocrystals can emit fluorescence at different wavelengths depending on their size, being feasible to synthesize in all UV-Vis spectra and use them as emitters in optoelectronics or in (bio) chemical sensing as labels [49]. To further improve the photoluminescence efficiency of such nanocrystals, overcoating them using inorganic shell materials having similar lattice parameters and higher band gap energy is found to be successful.

In case of CdSe, preferred shell materials include zinc selenide (ZnSe), zinc sulphide (ZnS), and cadmium sulphide (CdS) [50–53]. Among these, combining CdSe and ZnSe as core-shell NCs is remarkably needed to stop interfacial misfit dislocations from evolving and hence reduce the trapping sites of electrons and holes [54]. However, no enough theoretical and numerical studies were conducted by this combination. Exclusively, using CdSe as a core and silver metal as a plasmonic shell, size dependent local field enhancement factor (LFEF) was not investigated in the presence and absence ZnSe as spacer. Moreover, when the shape of nanocomposite materials are changed alternately as spherical, cylindrical, oblate, and prolate forms, changes that could be observed in optical properties like local field enhancement, absorption, and extinction cross sections were not studied for gold coated CdSe core-shell nanocomposites (NCs) so far. Hence, this study is designed to bridge these gaps and attempted to provide theoretical and numerical findings regarding plasmonic effects and effects of size and shape on the optical properties of CdSe based core-shell NCs.

1.3 Objectives of the study

The general objective of this dissertation is to investigate the plasmonic effects and the effects of size, shape, and host medium on the optical properties of core-shell NCs. Explicitly, this study attempted to address the following specific objectives.

1. Investigate effects of core size on LFEF of CdSe@Ag spherical core-shell NCs.
2. Study plasmonic effects on the LFEF of CdSe@Ag spherical core-shell NCs.
3. Analyze the effect of inserting ZnSe as a spacer between CdSe core and Ag shell on the LFEF of spherical core-shell NCs.
4. Determine effects of shape on the extinction cross sections of CdSe@Au core-shell NCs.
5. Investigate the effect of host medium on the optical properties of various shapes of core-shell NCs.
6. Compare the optical properties of spherical, cylindrical, oblate, and prolate shape CdSe@Au core-shell NCs.

1.4 Dissertation outline

The next four chapters of this dissertation are organized as follows:

- ❒ Chapter 2: Describes the interaction of matter with electromagnetic fields and the optical responses of the interaction. Moreover, it discusses the free electron model, the harmonic oscillator model, Mie theory of scattering, basics of plasmonics, core-shell quantum dots, and Laplace's equation in spherical and ellipsoidal coordinates.
- ❒ Chapter 3: The basic theoretical models used in the study are presented in this Chapter. These include the Drude-Lorentz model,core-shell models, and the

quasi-static approach. The Chapter also discusses the technical procedures employed and the software package used in plotting the numerical results of the study.

- ❒ Chapter 4: Discusses how the size of the core, the shell, and the spacer affect the LFEF of CdSe-based core-shell nanoparticles. It also emphasizes the effect of inserting a spacer (ZnSe) on the LFEF of CdSe@ZnSe@Ag nanoparticles.

- ❒ Chapter 5: Presents the effects of shapes on the optical properties of CdSe@Au nanocomposites. It describes that spherical, cylindrical, prolate, and oblate spheroids all with the same inner and outer radii show different optical properties due to their geometries.

- ❒ Chapter 6: This chapter summarizes all the findings of the study and indicates the proposed areas for additional future research work.

Chapter 2

Optical Properties of Nanostructures

2.1 Introduction

One of the most interesting and important features of nanoparticles is their optical properties. Understanding the optical properties of materials is essential for designing optoelectronic components and applying them to nanodevices. However, the importance of explaining the optical properties of nanocomposites is given no emphasis in the classical theory of bulk systems. Hence, considering the optical properties of nanostructures as a separate theme is required. Moreover, the clear dependence of the optical properties of a nanomaterial on its size [55, 56], shape [57, 58], internal structure, and external embedding environment [59] is opening up additional capabilities for regulating materials for diverse practical applications. Due to these reasons, the optical properties of nanoscale structures are currently drawing the research attentions of many scholars.

The optical properties of nanomaterials are resulted when oscillating electromagnetic (EM) field interacts with them. At the nanoscale range, the simplest examples that can result from this type of interaction include the blue shift of absorption and the photoluminescence emission of semiconductor nanomaterials. The characteristics observed due to this interaction strongly depends on the spatial and temporal condition of elec-

tromagnetic field and polarizability of matter. Among the parameters that govern this dependency are the frequency, direction of light propagation, and the induced polarization of nanomaterials.

Optical properties of nanomaterials can solids provide tools for investigating bandgap energy, level of impurity, lattice vibrations, excitons, and some magnetic properties. Moreover, these properties are used to describe the nature, homogeneity, crystal structure, and composition of the materials and also let us know whether the materials are metals, semiconductors, or insulators. Hence, to understand and explain the optical properties of materials, studying their dielectric permittivity, local field enhancement, absorption coefficients, and extinction cross sections is essential.

In order to understand the optical properties of materials more deeply, understanding how light interacts with matter is very fundamental. Due to this, in the following sections, we presented our review by starting from scattering theory of light followed by the electrodynamic properties of materials with the help of Maxwell's equations. Responses of electrons to external forces or electromagnetic fields are also vital to study the optical responses of materials. To address this, we discussed the Drude-Sommerfeld model and the Lorentz harmonic oscillator for free and bound electrons. Moreover, the effects of plasmons on the optical properties of metallic nanomaterials and metal coated core-shell nanostructures are significant. As a result, we also extended our review to discuss some fundamental concepts about the basics of plasmonics. Local field enhancement factor, absorption cross sections, and extinction properties that are used to explain the optical properties of materials are also included in different sections of the current Chapter. Since the size, shape, surface characteristics, and environments of nanomaterials also affect their optical characteristics, the electric potential distributions in core-shell structures of spherical and spheroidal nanostructures have been reviewed using Laplace's equation.

2.2 Interaction of matter with electromagnetic field

The optical properties of materials are determined by how they interact with EM waves. This interaction can occur in various ways such as absorption, scattering, transmission and reflection.A variety of events that are not frequently referred to as scattering are eventually the consequence of scattering. These include specular and diffused reflection, refraction at interfaces, and various diffraction phenomena. Our study focused on the interaction of light with a homogeneous medium where the material heterogeneity is much smaller than the wavelength of the incident field (Fig. 2.1). To study the optical characteristics of materials, understanding the basic theory of light scattering is crucial.

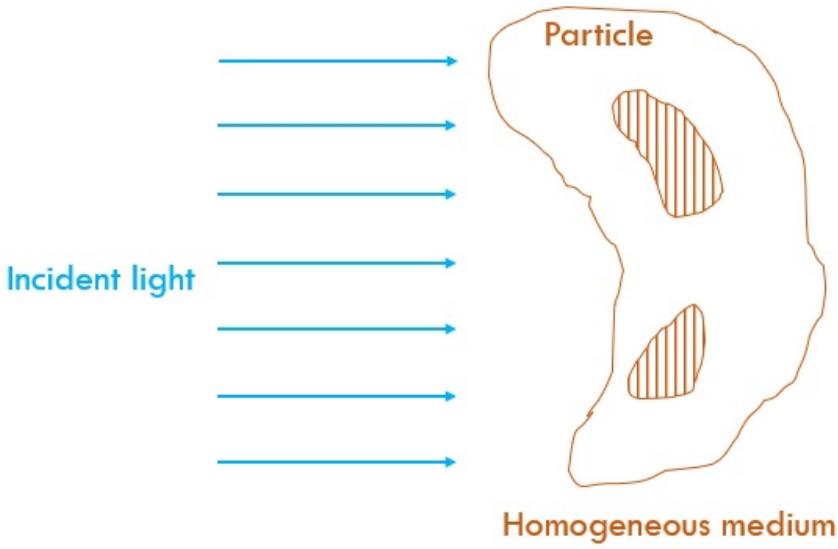

Figure 2.1: Schematic diagram showing interaction of light with matter.

2.2.1 Basic theory of scattering and absorption of light

Electrons and protons are discrete electric charges that make up matter. When an EM field illuminates a condensed material, electric charges in the material execute an oscillatory motion. At the same time, these accelerating electric charges emit EM

energy in all directions, a process called scattering (secondary radiation)[60]

$$Scattering = excitation + reradiation.$$

The scattering of electromagnetic fields by a given system is associated with its heterogeneity. Since every system, with the exception of a vacuum, is heterogeneous, all mediums scatter light. Irrespective of the heterogeneity type of a system, the basics of scattering are the same for every system.

Most of the light we see reaches our eyes in an indirect way. Looking at a cloud, or the sky, we see scattered sunlight. Even a light does not reach our eyes directly from the illuminating filament, it typically emits only the light that a ground glass bulb has dispersed. A leaf on a tree appears green as it reradiates (scatters) the green light more effectively than the red one. In addition to being scattered by the excited elementary charges, there is also an absorption by which a portion of the incident electromagnetic energy is changed into another form, such as thermal energy. The red light incident on the leaf is absorbed; this means it is no longer possible to see red light because energy has been transformed into another form. Due to scattering and absorption processes, a beam of light travelling through the medium loses energy; *i.e.*, a beam of light is attenuated. This attenuation is referred to as extinction, and can be expressed as [61]

$$Extinction = scattering + absorption.$$

2.2.2 Electrodynamic properties of materials

The initial light-matter interaction, described by the frequency dependent permittivity of materials, enters the model of electrodynamic scattering and produces distinctive spectra that are explained by the statistics and individual properties of materials. The physically appropriate parameters for describing the basics of the light-matter interaction are the photon energy $\hbar\omega$ and the material's frequency dependent electric permittivity $\varepsilon(\omega) = \varepsilon^{'}(\omega) + i\varepsilon^{''}(\omega)$. NNonetheless, when describing about the propagation

of waves through a medium, the incident wavelength λ and the complex index of refraction of the medium $\tilde{n}$ are required. These two can be related as [62]

$$\tilde{n} = n + ik = \sqrt{\varepsilon' + i\varepsilon''} \qquad \text{Maxwell's relation}$$

$$\frac{\omega}{c} = \frac{2\pi}{\lambda}(n + ik) \qquad \text{Dispersion relation}$$

where n and k are the real and the imaginary parts of the index of refraction, respectively. Similarly, $\varepsilon^{'}$ and $\varepsilon^{''}$ denote the real and the imaginary components of the electric permittivity, respectively, c is the speed of EM wave propagation.

In the presence of matter, electromagnetic field can be explained using Maxwell's equations with the source terms of charge and current densities. Since 1865 when Maxwell published his famous set of equations, the results of electromagnetic research has been formalized. It has been recognized that EM phenomena is originating from a distribution of electric charge and current, and produces electromagnetic field. To describe electromagnetic wave propagation through a material medium, the theoretical foundations for the optical characteristics of materials are expressed using Maxwell's equations. In SI units, these equations are given by

$$\nabla \cdot \mathbf{D} = \rho, \tag{2.1}$$

$$\nabla \cdot \mathbf{B} = 0, \tag{2.2}$$

$$\nabla \times \mathbf{E} = -\frac{\partial \mathbf{B}}{\partial t}, \tag{2.3}$$

$$\nabla \times \mathbf{H} = -\mathbf{J} + \frac{\partial \mathbf{D}}{\partial t}, \tag{2.4}$$

where **E**, **D**, **H**, and **B** are electric field, electric displacement, magnetic field, and magnetic induction, respectively; ρ and **J** are charge and current densities respectively.

The electric diaplacement **D** and magnetic field **H** can be defined by

$$\begin{aligned} \mathbf{D} &= \varepsilon_0 \mathbf{E} + \mathbf{P}, \\ \mathbf{H} &= \frac{\mathbf{B}}{\mu_0} - \mathbf{M}, \end{aligned} \tag{2.5}$$

where **P** and **M** are polarization (electric dipole moment per unit volume) and magnetization (magnetic moment per unit volume), respectively; ε_0 is electric permittivity in the vacuum, and μ_0 is magnetic permeability in the empty space. To make Maxwell's equation sufficient, they need to be supplemented by constitutive relations, given by [60]

$$\mathbf{J} = \sigma \mathbf{E}, \tag{2.6}$$

$$\mathbf{B} = \mu \mathbf{H}, \tag{2.7}$$

$$\mathbf{P} = \varepsilon_0 \chi \mathbf{E}, \tag{2.8}$$

where σ is the conductivity, μ is the permeability, and χ is the electric susceptibility.

2.2.3 Free-electron model

A straightforward method to the optical characteristics of conduction electrons in metals employs the Drude-Sommerfeld model. According to this approach, it is possible to obtain the property of a metal particle initially by considering how external forces affect a single free conduction electron. The macroscopic property can then be obtained by multiplying the effect on a single conduction electron by the total number of electrons. Assuming that all the electrons in the Drude-Sommerfeld model are acting in phase, it can be said that there is the strongest coupling between them.

Only three years later, when J. J. Thomson discovered the electron, the model of free-electron gas was first used by Drude to describe the optical properties, high electric conductivity, and thermal conductivity of metals [63]. He assumed that the valence electrons in the crystal are able to move freely in the crystal, and behave like the par-

ticles of an ideal gas at the temperature T of the crystal [64]. Hence, the name "free electron model" is used. The model assumes that all electron-electron and electron-ion interactions are neglected.

In this model, a gas of free electrons with n carriers per unit volume, each having an effective mass of m and charge e, is considered. The response of the carriers to spatially steady driving electric field $\mathbf{E} = \mathbf{E}_0 \exp(-i\omega t)$ with amplitude E_0 and frequency ω is described via the classical equation of motion as

$$m\frac{\partial^2 \boldsymbol{r}}{\partial t^2} + m\gamma\frac{\partial \boldsymbol{r}}{\partial t} = -e\mathbf{E}_0 e^{-i\omega t}, \tag{2.9}$$

where $\boldsymbol{r} = \boldsymbol{r}_0 \exp(-i\omega t)$ is the displacement of a particle having the same direction and frequency as that of the driving electric field, γ is damping constant related to the dissipative mechanisms caused by the random interactions between impurities of any kind and the electrons, phonons, and other imperfections of the crystal. Substituting $\boldsymbol{r} = \boldsymbol{r}_0 \exp(-i\omega t)$ in to Eqn. (2.9) and simplifying it gives

$$\boldsymbol{r} = \frac{e/m}{\omega(\omega + i\gamma)}\mathbf{E}. \tag{2.10}$$

From an oscillator's response to a time-harmonic electric field, the optical constants relevant to a group of such oscillators are easily deduced. For such an oscillator, the induced dipole moment $\boldsymbol{p}$ is $-e\boldsymbol{r}$ and the polarization is $\boldsymbol{P} = -ne\boldsymbol{r}$. By using this relation with Eqn. (2.10) we can write

$$\boldsymbol{P} = -\frac{(ne^2/m)}{\omega(\omega + i\gamma)}\mathbf{E}. \tag{2.11}$$

Comparing Eqn. (2.8) with Eqn. (2.11) gives

$$\chi = -\frac{(ne^2/m\varepsilon_0)}{\omega(\omega + i\gamma)} = -\frac{\omega_p^2}{\omega(\omega + i\gamma)} = \chi_{DS}, \tag{2.12}$$

where the bulk plasma frequency is

$$\omega_p = \sqrt{\frac{ne^2}{m\varepsilon_o}},$$

and χ_{DS} represents electric susceptibility of Drude-Sommerfeld model. Further again, from Eqns. (2.5) and (2.8), we can find the relation

$$\varepsilon = 1 + \chi_{DS}, \tag{2.13}$$

Finally, for a metal with free electrons, its dielectric function can be found by substituting the last part of Eqn. (2.12) into Eqn. (2.13) as

$$\varepsilon = 1 - \frac{\omega_p^2}{\omega^2 + i\gamma\omega}, \tag{2.14}$$

where its real and imaginary components can respectively be given as

$$\varepsilon^{'} = 1 - \frac{\omega_p^2}{\omega^2 + \gamma^2}, \qquad \varepsilon^{''} = \frac{\omega_p^2 \gamma}{\omega(\omega^2 + \gamma^2)}. \tag{2.15}$$

This is the dielectric function of the Drude-Sommerfeld model for a free-electron metal.

2.2.4 Harmonic oscillator model

The interaction of matter with electromagnetic fields is governed by the forces that the incident fields exert on the electric charges within the matter. The electrons inside the condensed matter can frequently be displaced by the incident electric field $\boldsymbol{E}$ at high frequencies. However, the ions are generally too inert to be displaced by this field with the same frequency. As a result, atoms in the condensed matter become electric dipoles, each with a dipole moment $\boldsymbol{p}$. The incoming light can also interact with ions at low frequencies in the far infra-red (IR) radiation and create dipole moments by separating the positively and negatively charged ions in opposite directions.

For a given sample material, the net polarization $\boldsymbol{P}$ is found by adding up each dipole moment in the sample. The linear relationship between $\boldsymbol{E}$ and $\boldsymbol{P}$ can be shown by Eqn. (2.8) describing the macroscopic electric susceptibility χ of the material.

The linearity in Eqn. (2.8) shows that charges that are displaced from their equilibrium position are retreated by restoring forces. As a result, a charge q_j of mass m_j executes forced oscillations in a time-harmonic electric field $\boldsymbol{E} = \boldsymbol{E}_0 \exp(-i\omega t)$. This is referred to as the *harmonic oscillator model*. The linear restoring force in displacement follows from a harmonic potential of

$$V(\boldsymbol{r}) = \sum_j \frac{1}{2} m_j \omega^2 \boldsymbol{r}_j. \tag{2.16}$$

For charge q_j with displacement $\boldsymbol{r}_j$, this condition results in harmonic oscillation. Following the balance force, we obtain

$$\sum_j m_j \frac{\partial^2 \boldsymbol{r}_j}{\partial t^2} + m_j \gamma_j \frac{\partial \boldsymbol{r}_j}{\partial t} + D_j \boldsymbol{r}_j = \sum_j q_j \boldsymbol{E}(t) \tag{2.17}$$

The term containing γ in Eqn. (2.17) represents the perturbation due to interactions with other charges and lattice defects. For a given electric field $\boldsymbol{E} = \boldsymbol{E}_0 \exp(-i\omega t)$, a time harmonic solution to Eqn. (2.17) is given by

$$\boldsymbol{r}_j = \frac{q_j}{m_j} \frac{\boldsymbol{E}_0}{\omega_j^2 - \omega^2 - i\gamma_j \omega}, \tag{2.18}$$

where $\omega_j = \sqrt{D_j / m_j}$ is the resonance frequency, and D_j is the stiffness of the j^{th} oscillator. From each dipole moment $\boldsymbol{p}_j = q_j \boldsymbol{r}_j$, the net polarization $\boldsymbol{P}$ in a given sample of V can be given by

$$\boldsymbol{P} = \frac{1}{V} \sum_j N_j \, \boldsymbol{p}_j = \frac{1}{V} \sum_j N_j \, q_j \, \boldsymbol{r}_j. \tag{2.19}$$

For all N_j and q_j in Eqn. (2.19), the susceptibility χ_j can be given by

$$\chi_j(\omega) = \frac{1}{V}\sum_j \frac{N_j\, q_j^2}{\varepsilon_0\, m_j} \frac{1}{\omega_j^2 - \omega^2 - i\gamma_j\omega}, \tag{2.20}$$

where N_j/V represents the total density of charges of q_j with mass m_j and eigenfrequency ω_j. With regard to this, χ in Eqn. (2.20) also holds true for ionic crystals, with the corresponding ionic masses and charges. The linearity assumption of Eqn. (2.8) leads to the summation of all contributions χ_j resulting in a total susceptibility χ.

The polarization $\boldsymbol{P}$ shown in Eqn. (2.8) contributes to the electric field displacement vector $\boldsymbol{D}$ as

$$\boldsymbol{D} = \varepsilon_0\boldsymbol{E}_0 + \boldsymbol{P} = \varepsilon_0(1+\chi)\boldsymbol{E}_0. \tag{2.21}$$

This equation can also be used to define the complex dielectric function as $\varepsilon(\omega)$ as

$$\varepsilon(\omega) = 1 + \chi = 1 + \sum_j \frac{\omega_{pj}^2}{\omega_j^2 - \omega^2 - i\gamma_j\omega} = \varepsilon_1(\omega) + i\varepsilon_2(\omega), \tag{2.22}$$

where

$$\omega_{pj}^2 = \frac{N_j\, q_j^2}{V m_j \varepsilon_0}. \tag{2.23}$$

The *harmonic oscillator model* in Eqn. (2.22) was formulated by H. A. Lorentz (1853-1928) at about the start of the 20$^{\text{th}}$ century.

At low frequencies, *i.e.,* as $\omega \to 0$, the real term of the dielectric function, $\varepsilon_1(0)$ yields constant and is given by

$$\varepsilon_1(0) = 1 + \sum_j \frac{\omega_{pj}^2}{\omega_j^2}. \tag{2.24}$$

Under the same condition, the imaginary term, $\varepsilon_2(0)$ vanishes. $\varepsilon_1(0)$ denotes the static electric permittivity of the material. The ratio ω_{pj}^2/ω_j^2 is constant and represents the oscillator strength f_j of the j^{th} harmonic oscillator, so that ω_{pj}^2 in Eqn. (2.22) can be replaced by $f_j\omega_j^2$.

2.2.5 Lorentz model for bound electrons

Regarding the optical properties of matter, Lorentz developed a conventional theory that states that when a material is exposed to a force of EM fields, its electrons and ions execute simple harmonic oscillations.

To understand this model, let's imagine an atom whose electrons are connected to the nucleus in a similar manner that a spring connects a small mass to a large mass. Then, for a bound electron having charge $-e$ and mass m, the equation of motion for a displacement $\boldsymbol{r} = \boldsymbol{r}_0 \exp(-i\omega t)$ is described by

$$m\frac{\partial^2 \boldsymbol{r}}{\partial t^2} + m\gamma\frac{\partial \boldsymbol{r}}{\partial t} + k\boldsymbol{r} = -e\mathbf{E}_0 e^{-i\omega t}, \tag{2.25}$$

where γ is a damping factor and k is the spring constant. For an incident time-harmonic optical electromagnetic field, $\mathbf{E} = E_0 \exp(-i\omega t)$, the dipole moment between an electron of charge $-e$ and its positive nucleus $+e$ is given by

$$\boldsymbol{p} = -e\boldsymbol{r} = -\frac{e^2/m}{\omega_o^2 - \omega^2 + i\gamma\omega}\mathbf{E}, \tag{2.26}$$

where $\omega_o = \sqrt{k/m}$ is a resonant frequency. The polarization $\boldsymbol{P}$ due to n atoms or electron-nucleus pairs per unit volume is

$$\boldsymbol{P} = n\boldsymbol{p} = \frac{ne^2/m}{\omega_o^2 - \omega^2 - i\gamma\omega}\mathbf{E}, \tag{2.27}$$

To include the interband contribution to the polarization, Eqn. (2.5) can be extended and the displacement vector $\mathbf{D}$ can be rewritten as

$$\mathbf{D} = \varepsilon_0\mathbf{E} + \boldsymbol{P}_{IB} + \boldsymbol{P}, \tag{2.28}$$

where $\boldsymbol{P}_{IB} = \varepsilon_0\chi_{IB}\mathbf{E}$ is polarization due to the interband contribution. Then, the dis-

placement vector **D** can be written further as

$$\mathbf{D} = \varepsilon_0(1 + \chi_{IB} + \chi_{DS})\boldsymbol{E}, \tag{2.29}$$

where

$$\chi_{IB} = \frac{\omega_p^2}{\omega_o^2 - \omega^2 - i\gamma\omega}.$$

Then, bound electrons' contribution to the dielectric function can be given by

$$\varepsilon_{IB} = 1 + \frac{\omega_p^2}{\omega_o^2 - \omega^2 - i\gamma\omega}, \tag{2.30}$$

with real and imaginary terms of

$$\varepsilon_{IB}^{'} = 1 + \frac{\omega_p^2(\omega_o^2 - \omega^2)}{(\omega_o^2 - \omega^2)^2 + \gamma^2\omega^2}, \quad \varepsilon_{IB}^{''} = \frac{\omega_p^2\gamma\omega}{(\omega_o^2 - \omega^2)^2 + \gamma^2\omega^2}. \tag{2.31}$$

From Eqn. (2.29), the complex dielectric function including all properties of an optical material near the visible spectrum can be written as [27]

$$\varepsilon(\omega) = (1 + \chi_{IB} + \chi_{DS}). \tag{2.32}$$

Substituting for χ_{DS} from Eqn. (2.12), this is equivalent to

$$\varepsilon(\omega) = 1 + \frac{\omega_p^2}{\omega_o^2 - \omega^2 - i\gamma\omega} - \frac{\omega_p^2}{\omega^2 + i\gamma\omega}. \tag{2.33}$$

Considering effective parameters ω_p and γ, and by introducing ε_∞ as the contribution of bound electron to the polarizability, the dielectric function of a metallic material is

$$\varepsilon(\omega) = \varepsilon_\infty - \frac{\omega_p^2}{\omega^2 + i\gamma\omega}. \tag{2.34}$$

The dielectric function which depends on the dimension of a material can be introduced through the model of limiting the mean free path between collisions of conduction electrons. When a nanoparticle gets smaller in size, its thickness finally falls below

the bulk mean free path, and electron scattering from its surfaces has a less impact, thereby broadening the peak of its plasmon resonance. If the change in the size of the nanoparticle affects the size of the mean free path of electrons, a correction for nanoshells is needed, and in this condition, γ is modified as [65]

$$\gamma(r) = \gamma_0 + A\frac{v_F}{r_{eff}}, \tag{2.35}$$

where γ_0 is the damping parameter of the bulk matter, v_F is the velocity of an electron at the Fermi level, A is the phenomenological parameter employed to match the calculated damping parameter to its experimental value. For a core-shell spherical NCs of core-radius r_1 and shell radius r_2, r_{eff} is the effective mean free path of collisions and can be calculated from [66]

$$r_{eff} = \frac{1}{2}\left[(r_2 - r_1)(r_2^2 - r_1^2)\right]^{\frac{1}{3}}. \tag{2.36}$$

2.2.6 Mie theory

For materials of larger sizes, where the quasi-static approach is not justified due to substantial phase-variations of the incident driving force field over the volume of the material, a rigorous electrodynamic approximation will take effect. With this assumption, Gustav Mie considered Maxwell's equations and solved them by considering a spherical particle interacting with an incident plane field [67]. Fundamentally, EM fields are expanded according to their multipole contributions and the coefficients that are used for expansions are calculated by using appropriate boundary conditions for electromagnetic fields at the correct interface between the metallic nanoparticle and its surrounding.

In Mie theory, the scattering and extinction cross sections of a spherical nanoparticle are given by

$$\sigma_{ext} = \frac{\lambda^2}{2\pi}\sum_{n=1}^{\infty}(2n+1)\mathrm{Re}(a_n + b_n), \tag{2.37}$$

$$\sigma_{scat} = \frac{\lambda^2}{2\pi}\sum_{n=1}^{\infty}(2n+1)\mathrm{Re}(a_n^2 + b_n^2), \tag{2.38}$$

with

$$a_n = \frac{\Psi_n(\beta)\Psi_n'(mx) - m\Psi_n(mx)\Psi_n'(x)}{\xi_n(x)\Psi_n'(mx) - m\Psi_n(mx)\xi_n'(x)}, \tag{2.39}$$

$$b_n = \frac{m\Psi_n(x)\Psi_n'(mx) - \Psi_n(mx)\Psi_n'(x)}{m\xi_n(x)\Psi_n'(mx) - \Psi_n(mx)\xi_n'(x)}, \tag{2.40}$$

where a_n and b_n are scattering coefficients, m is the ratio of the index of refraction of the spherical metal to that of host material, x represents size parameter of the particle, ξ and Ψ show *Riccati-Bessel* functions and their respective primes ($'$) denote the first differentiation of *Riccati-Bessel* functions with respect to the argument, and and n is index of summation of partial waves ($n = 1$ for dipole oscillation, $n = 2$ for quadrupole oscillation, $n = 3$ for octupole, and so on).

2.3 Plasmonics

Plasmonics is the discipline that studies the light matter interactions at metal-dielectric interfaces through surface EM excitations such as surface plasmon polaritons (SPPs) and localized surface plasmons (LSPs). Since these excitations are well localized at the interface, their effects result in a considerable EM field enhancement at the proximity of the interface. SPPs and LSPs are excellent candidates to be integrated into devices as they have interesting features that make faster and smaller than the current photonic devices. Moreover, devices made by incorporating SPPs and LSPs are also faster than their electronic counterparts of comparable in size. Thereby, they are able to fill the gap in size that exist between microelectronic and photonic devices.

The field of study in plasmonics can generally be split into two categories: the propagating and the localized plasmonic modes [68]. LSPs are observed when coherent electrons are oscillating localized to the surface of nanomaterial whereas SPPs are de-

tected at extended metal surfaces where coherent electrons are oscillating as longitudinal waves [69]. The intentions of both theoretical and experimental investigations in plasmonic research include the need for fundamental science reasons, thereby widening the scope of plasmonic applications, and the interest in developing engineered devices that function on the basis of surface plasmons. [70, 71]. However, there is no clear demarcation between these two intentions, and they even merge sometimes. Yet, several uses of plasmons have also been suggested, and some of them have already undergone experimental testing. Overall, the various investigations made so far have predicted and realized new features of LSPs and SPPs.

2.3.1 Surface plasmons

Most likely, the studies that involved the bombardment of thin metal sheets by electrons moving with very high speed are where the history of plasmon begins [72]. The results, however, were not fully understood until Pines and Bohm [73, 74] realized the collective excitations of longitudinal oscillations of electrons that might have been caused by the long-range coulombic forces associated with electrons in the valence band of thin metal sheets. As these excitations are similar to plasma oscillations of electrons in gas discharges, in 1952, Pines coined the phrase "plasmon" to explain them and stated that they possess an energy of $\hbar\omega_p$.

Rufus Ritchie [75], in 1957, examined the effect of thin metal sheet boundaries and presented a new collective excitations of energy $\hbar\omega_p/\sqrt{2}$. In experimental studies involving electron energy loss, Powell and Swan [76] discovered similar excitations only two years later. Then, Stern and Ferrell [77] ultimately explained the excitations as surface plasmons.

Maxwell's equations are used to describe how light propagates in a bulk plasma-like material. When a wave is in a plane form like $e^{i(\boldsymbol{k}\cdot\boldsymbol{r}-\omega t)}$ and is travelling through an isotropic, non-magnetic medium whose permittivity varies with frequency $\varepsilon(\omega)$,

Maxwell's equation in a source free region (*i.e.*, $\nabla \cdot \boldsymbol{D} = 0$) gives

$$\varepsilon(\omega)\boldsymbol{k} \cdot \boldsymbol{E} = 0, \tag{2.41}$$

whose two solutions are as follows:

$$\varepsilon(\omega) = 0 \quad \text{and} \tag{2.42}$$

$$\boldsymbol{k} \cdot \boldsymbol{E} = 0. \tag{2.43}$$

The first solution belongs to longitudinal oscillation resulted from collective excitation of conduction electrons. According to the explanation of Pines and Bohm, this corresponds to the bulk plasmon.

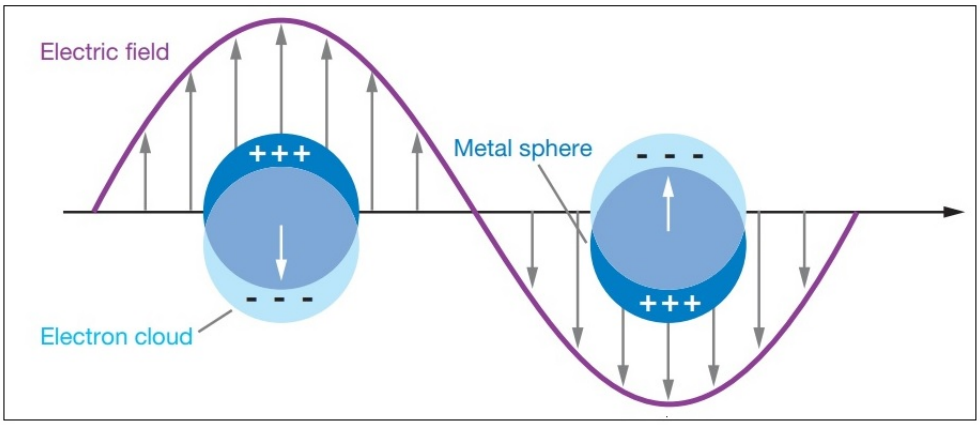

Figure 2.2: Schematic diagram illustrating localized surface plasmon [69].

It is possible to describe a metallic nanoparticle as a nanoparticle with a lattice of ionic cores through which conduction electrons are moving freely, whereas plasmons are the collective oscillation of free electron density with respect to the immovable positive ions in metals.when the field reverses its direction, the electrons align themselves in the opposite direction (Fig. 2.2). This oscillation of electron cloud depends on the applied electric field and the quantization of these oscillations is called plasmons. Hence, the interaction of photons with metal nanostructures leads to the formation of plasmons.

2.3.2 Localized surface plasmons

When the metal nanoparticle is illuminated with light, the force of the EM field causes the conduction electrons to move towards the surface, creating an electric dipole. The applied external electric field causes the free conduction electrons at the mettal surface to oscillate collectively to produce surface plasmons (SPs). The dipole in turn induces an electric field within the nanoparticle that opposes the external field of the light, drives the electrons back to the equilibrium position, and acts as a restoring force. This is analogous to a linear harmonic oscillator, where the restoring force is directly related to the displacement measured from the equilibrium position. When the driving field is removed after the electrons have been shifted from their equilibrium position, they will oscillate at a specific frequency known as the resonant frequency. For SPs, this is referred to as plasmonic frequency. The resulting phenomenon is known as surface plasmon resonance (SPRs). In 1968, Otto [78] made the initial discovery of the SPR phenomenon whereas, its commercial realization was carried out by Biacore of GE Healthcare in 1990 [79].

When the frequency of the incident light coincides with the natural frequency of conduction electrons oscillating in opposition to the restoring force, the resonance state is reached. If the collective electron oscillations of SPRs are confined to the nanoparticle's surface, the phenomenon is known as localized surface plasmon resonance (LSPRs). The effects of LSPs have two major categories: the enhancement of electrical field in the vicinity of the surface of the particle and the occurrence of maximum absorption at the resonant frequency of plasmon. The size, shape, and refractive index of the embedding medium have a significant impact on where the wavelength of LSPRs is located. These characteristics enable precise control of the optical absorption of the nanomaterial from the visible to near-IR regions. The resonance frequency for Au and Ag nanoparticles lie in the range of visible EM spectrum. This results in the brilliant colors that the particles display in reflected and transmitted light as a result resonantly enhanced scattering and absorption conditions. This property has been used for several

hundreds of years, for instance in the ornamental cups, as shown in figure 1.1.

It is also worth to note that there are many approaches to excite LSPs from plasmonic materials. A light source that is incident on the nanomaterial can excite LSPs so that the local EM field is enhanced [80]. Local oscillating sources, such as molecular electric dipoles and quadrupoles, could also induce LSPs in the vicinity of the plasmonic nanomaterials. These sources could reradiate the local field in a direction that extends several wavelengths into the far-field area.

2.3.3 Surface plasmon polaritons

Surface plasmon polariton is a propagating EM wave along a plane of metal-dielectric interface. As it moves deeper from the surface into each medium, its amplitude decays exponentially. The term "surface plasmon polariton" describes that the wave comprises the motion of charges in the metal ("surface plasmon") and EM waves in the dielectric material ("polariton") [81]. They are a kind of surface waves that propagate along the interface in much similar manner that light can be directed by optical fibers. SPPs travel over the interface until they lose all of their energy, either by metal absorption or dispersion in other regions, such as free space. In lossy metals, too, the amplitude

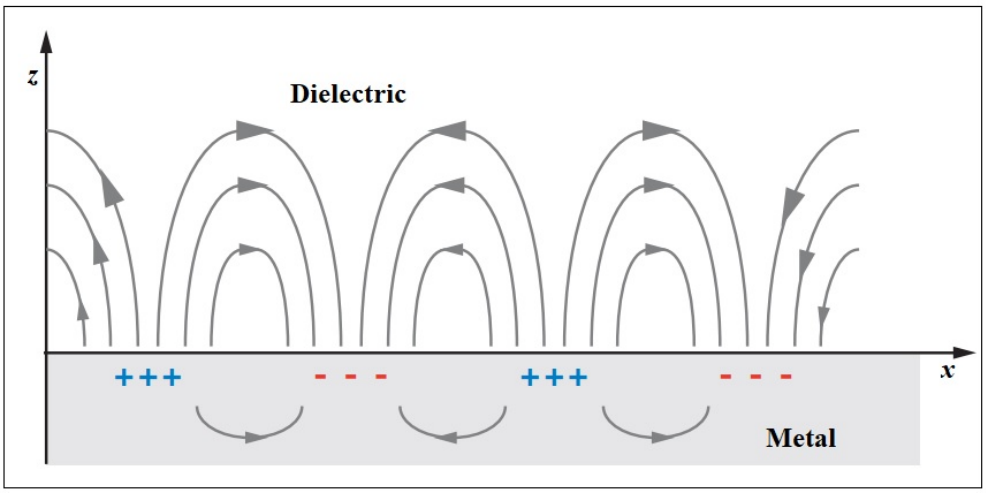

Figure 2.3: Schematic of surface plasmon polariton at metal-dielectric interface [69].

of this wave exponentially decreases in the direction it propagates. For the first time,

such propagating surface waves were explained by Zenneck in 1907 [82]. Because of their strong field confinement and enhancement effects, SPPs have found a variety of intriguing applications, such as in surface-enhanced spectroscopy, biosensing, and nano-optics. Due to mismatches in the propagation wave vectors, an incident plane wave in the dielectric cannot directly excite the SPP wave at a smooth metal-dielectric interface. Rather, the SPP can be launched through several special excitation configurations or coupling structures.

Using the Maxwell's vector equations in combination with Eqn. (2.43), the dispersion relation for a photon propagating in the medium becomes

$$k^2 = \varepsilon(\omega)\frac{\omega^2}{c^2} = \varepsilon(\omega)k_0^2, \tag{2.44}$$

where k_0 is the free space wavevector. Here, it is crucial to comprehend the meaning of the word "polariton". For the first time, the term was coined by Hopfield [83]. Polariton is "a photon coupled to the internal degrees of freedom of the medium" [84]. Alternatively, polaritons can be stated as quasi-particles that result when EM fields interact with fundamental excitations in the system. In this description, the fundamental excitation represents the bulk plasmon, whereas the associated quasi-particle denotes the bulk plasmon-polariton, which is just another name for a photon that is travelling through a material. Hence, the two solutionsto Eqn. (2.41)are corelated to the bulk plasmon and bulk plasmon-polariton.

The dispersion relation of propagating surface waves along the interface of unlike materials can most likely be solved through a classical approach by considering the lower and upper half regions that are confined to appropriate boundary conditions [85]. The layer system in figure 2.3 has metal and dielectric material interface, on which a p-polarized wave propagates along the x direction. For this single interface between these two media, let their frequency dependent permittivities be ε_1 and ε_2, and permeabilities be μ_1 and μ_2, respectively, for medium 1 (metal) and medium 2 (dielectric

material). Then, in the ith medium, the perpendicular component of the wavevector k_{zi}, can be given by [68]

$$k_{zi} = \sqrt{n_i^2 k_0^2 - k_x^2}, \tag{2.45}$$

where k_0 is a wavevector in the free space, k_x is the wavevector within the plane, and $n_i = \sqrt{\varepsilon_i \mu_i}$. We then need the denominator of the reflection and transmission of Fresnel coefficients to vanish for the single interface scenario, providing us with the dispersion relations for the bound modes of the system as,

$$\frac{k_{z2}}{\varepsilon_2} + \frac{k_{z1}}{\varepsilon_1} = 0, \tag{2.46}$$

$$\frac{\mu_2}{k_{z2}} + \frac{\mu_1}{k_{z1}} = 0, \tag{2.47}$$

for p- and s-polarized light, respectively.

Substituting Eqn. (2.45) into Eqns. (2.46) and (2.47), enables us to rewrite these dispersion relations as,

$$k_x = k_0 \sqrt{\frac{\varepsilon_1 \varepsilon_2 (\varepsilon_1 \mu_2 - \varepsilon_2 \mu_1)}{\varepsilon_1^2 - \varepsilon_2^2}}, \tag{2.48}$$

$$k_x = k_0 \sqrt{\frac{\mu_1 \mu_2 (\varepsilon_2 \mu_1 - \varepsilon_1 \mu_2)}{\mu_1^2 - \mu_2^2}}. \tag{2.49}$$

For non-magnetic ($\mu_1 = \mu_2 = 1$) media, the dispersion relation for p-polarized (parallel polarized) surface propagating waves is given by [68]

$$k_x = k_0 \sqrt{\frac{\varepsilon_1 \varepsilon_2}{\varepsilon_1 + \varepsilon_2}}. \tag{2.50}$$

As SPP moves along the metal-dielectric interface, it is attenuated. As a result of this attenuation, their energy propagation length decreases and the performance of devices that make use of these surface EM waves is degraded. Ohmic losses in the metal are key mechanisms for the extinction of SPP as it moves along a plane of metal-dielectric interface. The incorporation of thin metallic film into a multilayer composite enclosed

with dielectric layers [86–89] is one of the strategies to increase the propagation distances of SPP.

2.4 Effective permittivity of composite materials

Shell nanostructures are frequently used for colloidal quantum dots (QDs) as they can significantly improve their optical properties. They also improve stability with regard to photodegradation and safeguard the fundamental optical qualities against alterations in the immediate environment [90]. Therefore, modeling the dielectric function of a composite system by using the strategy of Maxwell Garnett homogenization is preferred [91]. This strategy gives the correct effective dielectric function and polarizability for the whole composite structure in the quasistatic regime.

2.4.1 Effective permittivity of spherical inclusions

Let us consider the mixture of dielectric material and host matrix where spherical inclusions of permittivity ε_i are randomly positioned within the embedding medium of permittivity ε_e, as in figure 2.4. Let f represent the fraction of the total volume that the inclusion phase occupies. Then, $(1-f)$ will be the fraction of the volume left unoccupied. Each components of the material mixture have their own names: the inclusion part is known as *guest* whereas the embedding host is referred to as *host*, or *matrix*, and the mixing principle is known as the *Maxwell Garnett* formula [92].

Let the average field and the flux density be related by ε_{eff} as

$$< \mathbf{D} >= \varepsilon_{eff} < \mathbf{E} > . \tag{2.51}$$

In terms of volume fractions, this can be further given by

$$< \mathbf{D} >= f\varepsilon_i \mathbf{E}_i + (1-f)\varepsilon_e \mathbf{E}_e. \tag{2.52}$$

$$< \mathbf{E} >= f\mathbf{E}_i + (1-f)\mathbf{E}_e, \tag{2.53}$$

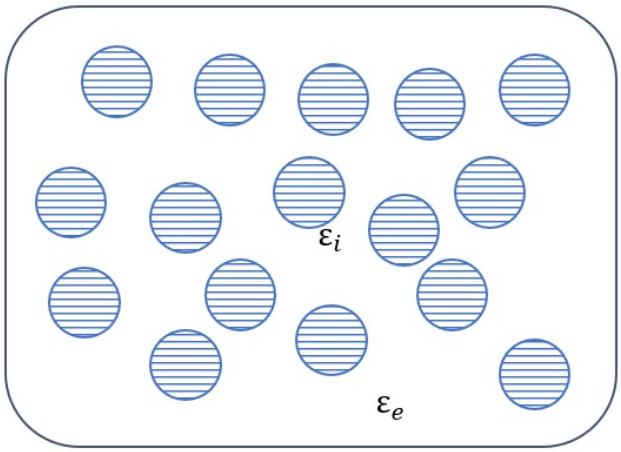

Figure 2.4: Schematics of inclusions of dielectric spheres in the dielectric host.

where $\mathbf{E}_i$ and $\mathbf{E}_e$ are the internal and external fields, respectively. Then the effective permittivity can be given by

$$\varepsilon_{eff} = \frac{f\varepsilon_i A + \varepsilon_e(1-f)}{fA + (1-f)}, \tag{2.54}$$

where $A = \mathbf{E}_i/\mathbf{E}_e$ (the ratio between the fields). Taking the field ratio $A = 3\varepsilon_e/(\varepsilon_i + 2\varepsilon_e)$ [93], one of the possible expression for the effective permittivity is

$$\varepsilon_{eff} = \varepsilon_e + 3f\varepsilon_e \frac{\varepsilon_i - \varepsilon_e}{\varepsilon_i + 2\varepsilon_e - f(\varepsilon_i - \varepsilon_e)}, \tag{2.55}$$

called Maxwell Garnett mixing formula. Eqn. (2.55) can be rewritten as

$$\frac{\varepsilon_{eff}}{\varepsilon_e} = 1 + 3f \frac{\varepsilon_i/\varepsilon_e - 1}{\varepsilon_i/\varepsilon_e + 2 - f(\varepsilon_i/\varepsilon_e - 1)}. \tag{2.56}$$

Two variables, the inclusion permittivity in relation to the environment $\varepsilon_i/\varepsilon_e$ and the fraction of volume of the inclusions f, can be used to calculate the effective permittivity in relation to ε_e. The limiting processes for the ceasing inclusion phase can be satisfied by the strategy of homogenization as

$$f \to 0 \qquad \Rightarrow \qquad \varepsilon_{eff} \to \varepsilon_e \tag{2.57}$$

and for the vanishing host medium

$$f \to 1 \qquad \Rightarrow \qquad \varepsilon_{eff} \to \varepsilon_i. \tag{2.58}$$

From the relation $A = \mathbf{E}_i/\mathbf{E}_e$, we can write

$$\mathbf{E}_i = \frac{3\varepsilon_e}{\varepsilon_i + 2\varepsilon_e}\mathbf{E}_e. \tag{2.59}$$

In studying the optical properties of materials, we know that polarizability (α) is an important concept. When an even electric field $\mathbf{E}_e$ permeates a homogeneous region of permittivity ε_e, electric dipole source is formed. External electric field and polarizability can be linearly related as

$$\boldsymbol{p} = \alpha \mathbf{E}_e, \tag{2.60}$$

where $\boldsymbol{p}$ is electric dipole. Hence, the simplest way to gauge the reaction of an inclusion to an electric field is to determine its polarizability. Within the inclusion, the dipole moment depends on the volume, internal field, and the dielectric contrast between the inclusion and the environment and can be given by [92]

$$\boldsymbol{p} = \int (\varepsilon_i - \varepsilon_e)\mathbf{E}_i dV, \tag{2.61}$$

where V denotes the volume of the sphere. Using Eqns. (2.59) to (2.61), we can write the dipole moment as

$$\boldsymbol{p} = (\varepsilon_i - \varepsilon_e)\frac{3\varepsilon_e}{\varepsilon_i + 2\varepsilon_e}\mathbf{E}_e \, V = 4\pi\varepsilon_e a^3 \frac{\varepsilon_i - \varepsilon_e}{\varepsilon_i + 2\varepsilon_e}\mathbf{E}_e, \tag{2.62}$$

where a is the radius of the sphere. From Eqn. (2.62), the polarisability of a homogeneous sphere of permittivity ε_i in a homogeneous environment of permittivity ε_e is given by

$$\alpha = 4\pi\varepsilon_e a^3 \frac{\varepsilon_i - \varepsilon_e}{\varepsilon_i + 2\varepsilon_e}. \tag{2.63}$$

2.4.2 Effective permittivity of a layered sphere

A spherical core-shell composite is a type of partially nonhomogeneous structure whose exact polarizability can be calculated. Let us analyze a composite of core-shell system comprising of a dielectric core of radius r_1 with dielectric permittivity ε_1 and a shell of radius r_2 with thickness t and dielectric permittivity ε_2. Moreover, let us assume that the core-shell composite system are randomly distributed in a solid dielectric of permittivity ε_e, as shown in figure 2.5. The optical characteristics of such composite core-

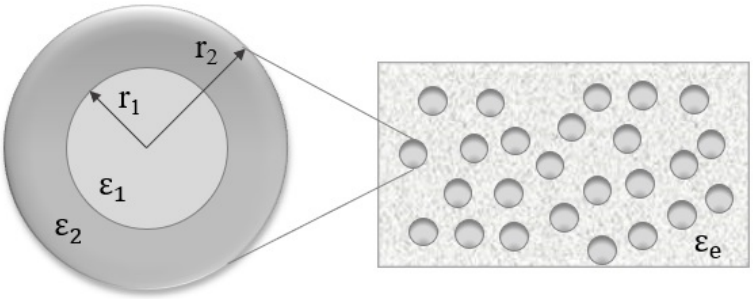

Figure 2.5: Schematics of distribution of nanoshells in external host matrix.

shell structure can be explained by replacing the homogeneous spherical core-shell particle equal outer radius (radius r_2 = r_1 +t) with dielectric material of permittivity ε_{eff} expressed as [94]

$$\varepsilon_{eff} = \varepsilon_2 \frac{(2\varepsilon_2 + \varepsilon_1) + 2f(\varepsilon_1 - \varepsilon_2)}{(2\varepsilon_2 + \varepsilon_1) + f(\varepsilon_2 - \varepsilon_1)}, \tag{2.64}$$

where $f = (r_1/r_2)^3$ is the core volume fraction.

In electromagnetic literature, the polarizability for such type of sphere is given by [90]

$$\alpha = 4\pi r_2^3 \frac{(\varepsilon_2 - \varepsilon_e)(\varepsilon_1 + 2\varepsilon_2) + f(\varepsilon_1 - \varepsilon_2)(2\varepsilon_2 + \varepsilon_e)}{(\varepsilon_2 + 2\varepsilon_e)(\varepsilon_e + 2\varepsilon_2) + 2f(\varepsilon_2 - \varepsilon_e)(\varepsilon_1 - \varepsilon_2)}. \tag{2.65}$$

It is worth to note that all values of the filling factor f between 0 and 1 can satisfy this expression.

2.5 Plasmonic materials

Plasmonic materials are nanomaterials that support surface plasmons [95, 96]. If we let the dielectric permittivity of a metal nanoparticle be ε_M, then, in a specific wavelength range, all metallic materials with a negative real part $Re[\varepsilon_M]$ and a positive imaginary part $Im[\varepsilon_M]$ of the dielectric function could be regarded as plasmonic materials [97–99]. Physically, the intrinsic absorption loss in light scattering processes decreases as $Im[\varepsilon_M]$ gets smaller [100].

If we consider a spherical metal nanoparticle embedded in a host matrix with electric permittivity ε_d, then, under the quasistatic approximation, the electric field in the interior and exterior regions of the nanoparticle can be given by [101–103]

$$E_{\text{in}} = \frac{3\varepsilon_d}{\varepsilon_M + 2\varepsilon_d} E_0, \tag{2.66}$$

$$E_{\text{out}} = E_0 + \frac{3\mathbf{n}(\mathbf{n}\cdot\boldsymbol{p}) - \boldsymbol{p}}{4\pi\varepsilon_0\varepsilon_d} \left(\frac{1}{r}\right)^3, \tag{2.67}$$

with r representing the distance from the surface of the particle, $\mathbf{n}$ is the unit vector along the point of interest, ε_0 is the permittivity of the free space, and E_0 is the amplitude of the incoming field.

Within the nanoparticle, the field is uniform, which, for metal nanoparticles, is generally not the case. The quasistatic approximation is no longer applicable for nanoparticles of larger sizes because the internal field distribution is inhomogeneous. In addition to the incident field, Eqn. (2.67) also comprises the local field distribution at the proximity of the surface of the nanoparticle. The distribution of this field leads to the local field enhancement.

To find out the expressions for absorption, scattering, and extinction cross sections in the quasistatic approximation, we investigate a nanoparticle exposed an oscillating electromagnetic field $\boldsymbol{E} = E_0 \exp(-i\omega t)$. The dipole moment induced by this oscillat-

ing field can be expressed as $\boldsymbol{p} = \varepsilon_0 \varepsilon_d \alpha E_0$, where the polarizability (complex) α of the nanoparticle in the electrostatic theory is given by

$$\alpha = 4\pi r^3 \frac{\varepsilon_M - \varepsilon_d}{\varepsilon_M + 2\varepsilon_d}. \tag{2.68}$$

Hence, under the condition

$$|\varepsilon_M + 2\varepsilon_d| = \text{minimun}, \tag{2.69}$$

the polarizability, the internal, and the external fields of the nanoparticle exhibit resonance properties. When $(\varepsilon_M + 2\varepsilon_d)$ approaches zero, the fields approach their maximum. This shows that $\text{Re}[\varepsilon_M]$ is nearly equal to $-2\varepsilon_d$ whereas the $\text{Im}[\varepsilon_d]$ is approximated to zero. This shows that, only materials with positive and close to zero $\text{Im}[\varepsilon_d]$ and moderate value of negative $Re[\varepsilon_M]$ could support robust LSPRs. Hence, it follows that from transition metals, elements such as gold, silver, and copper might satisfy these strict requirements to support surface plasmon with minimal intrinsic losses.

Moreover, applying boundary conditions and using the Laplace's equation ($\nabla^2 \Phi = 0$), electric potential distributions inside and outside the same material are given by [93]

$$\Phi_{\text{in}} = \frac{-3\varepsilon_d}{\varepsilon_M + 2\varepsilon_d} E_0 \, r \cos\theta, \tag{2.70}$$

$$\Phi_{\text{out}} = -E_0 \, r \cos\theta + \frac{\varepsilon_M - \varepsilon_d}{\varepsilon_M + 2\varepsilon_d} E_0 \, r^3 \, \frac{\cos\theta}{r^2}. \tag{2.71}$$

Here, Φ_{out} indicates the summation of the incident field and the dipole positioned at the nanparticle center, *i.e.*, the dipole moment induced by the incident field within the sphere is proportional to $|E_0|$. Therefore, enhanced polarization in α shows resonant improvements in the dipolar and internal fields, resulting in the widespread application of nanoparticles in optical equipment.

It is fascinating to notice from an optics perspective that improved polarization in α

also has another effect on how light is scattered and absorbed by nanoparticles [60]. For a nanosphere of volume V, radius R, and dielectric function $\varepsilon_M = \varepsilon_1 + i\varepsilon_2$ in the quasi-static approach, the absorption and scattering cross sections are, respectively given by [101]

$$C_{abs} = k\, Im\{\alpha\} = 4k\pi R^3 Im\left\{\frac{\varepsilon_M - \varepsilon_d}{\varepsilon_M + 2\varepsilon_d}\right\} \tag{2.72}$$

and

$$C_{scat} = \frac{k^4}{6\pi}|\alpha|^2 = \frac{8\pi k^4 R^6}{3}\left|\frac{\varepsilon_M - \varepsilon_d}{\varepsilon_M + 2\varepsilon_d}\right|^2 = \frac{128\pi^5}{3}\frac{R^6}{\lambda^4}\left|\frac{\varepsilon_M - \varepsilon_d}{\varepsilon_M + 2\varepsilon_d}\right|^2, \tag{2.73}$$

where $k = 2\pi/\lambda$ is the wave number. Both Eqns. (2.72) and (2.73) demonstrate that absorption and scattering cross sections show resonance behavior at $Re[\varepsilon_M] = -2\varepsilon_d$. From the theory of light scattering, the extinction cross section is given by

$$C_{ext} = C_{abs} + C_{scat}. \tag{2.74}$$

For nanoscale materials with size R satisfying the relation $R < 0.06\lambda$, the scattering is significantly small as compared to the absorption. Under this condition, the extinction cross section can be written as

$$C_{ext} \approxeq C_{abs}. \tag{2.75}$$

2.6 Local field enhancement

The local field, which Lorentz first described as the field at an atom, is currently believed to affect the particle property as a whole [27]. It is a field produced at an atomic site by all other atoms acting on the reference atom [104]. Like clusters of pure metals, nanoshells also exhibit local field enhancement effects [105]. The local field enhancement that results from LSP excitations can be applied in a wide variety of applications, including surface-enhanced Raman spectroscopy, surface-enhanced fluorescence, confocal microscopy, improving the performance of solar cells, and surface structuring [101].

The effect of local field enhancement strongly depends on the polarizability of the exciting radiation [106]. Particularly, the extinction properties of noble metal materials at the nanoscale level are dominated by strong surface plasmons. These resonances result when electrons in the conduction band are excited coherently by incident electromagnetic field. One of the distinctive properties of metallic nanoscale materials is their significant enhancement of local fields in close proximity to their surface. Under the quasi-static approximation, let us examine a metallic sphere of small size exposed to a plane wave of a monochromatic field

$$\mathbf{E} = E_0 \, exp\{i(kz - \omega t)\}, \tag{2.76}$$

where $\mathbf{E}$ is the incoming EM field, E_0 is amplitude of the incident field, z is the coordinate along the axis of the sphere, and k is the wave vector.The total field outside the spherical nanoparticle is the superposition of the incident field and the field scattered by the particle. In the quasi-static domain, the latter field corresponds to the field due to the dipole point. It is positioned at the center of the sphere and oscillates at the same frequency as that of the incoming field. The oscillating dipole depends on the potential $\Phi(r,\theta)$, distance r from the center, and polar angle θ in relation to the direction of the polarization of the incoming field. The amplitude of this dipole field can be derived from these dependences [60].

$$\Phi(r,\theta) = R^3 \frac{\varepsilon_M - \varepsilon_d}{\varepsilon_M + 2\varepsilon_d} E_0 \frac{\cos\theta}{r^2}, \tag{2.77}$$

where R, ε_M, and ε_d are the same as defined for Eqn. (2.72). Differentiating with respect to r and θ yields the normal $\mathbf{E}_r$ and tangential $\mathbf{E}_\theta$ components of the field as

$$\mathbf{E}_r = 2R^3 \frac{\varepsilon_M - \varepsilon_d}{\varepsilon_M + 2\varepsilon_d} E_0 \frac{\cos\theta}{r^3} \tag{2.78}$$

and

$$\mathbf{E}_\theta = R^3 \frac{\varepsilon_M - \varepsilon_d}{\varepsilon_M + 2\varepsilon_d} E_0 \frac{\sin\theta}{r^2}. \tag{2.79}$$

Based on the field-enhanced, Eqns. (2.78) and (2.79) offer the foundation for the application of metal nanoparticles. All surface-enhanced spectroscopies are driven by the modulus square of the electric field. This value could be expressed as

$$|E|^2 = R^6 \left| \frac{\varepsilon_M - \varepsilon_d}{\varepsilon_M + 2\varepsilon_d} \right|^2 E_0^2 \frac{(1+3\cos^2\theta)}{r^6}, \tag{2.80}$$

and describes the field outside the sphere for $r \geq R$. Since it is subjected to the quasi-static approximation, the field on the surface of nanoparticle ($r = R$) independent of the size of nanoparticle. In contrast, Eqn. (2.80) shows that the field outside the nanoparticle rapidly decreases as one moves away from the surface. As a result, the largest field enhancements are obtained at or near the nanoparticle surface.

As described in Section 2.5, when the sum of the denominators ($\varepsilon_M + 2\varepsilon_d$) approaches zero, the fields inside the nanoparticle and near its surfaces are greatly boosted. The real component of the permittivity for several metals is negative in the visible spectrum, showing that the condition $Re[\varepsilon_M] = -2\varepsilon_d$ is satisfied for certain wavelengths. At the resonance of this wavelength, the field amplitudes are significantly increased, given that the imaginary component of the permittivity $Im[\varepsilon_M]$, is minimal.

From Eqn. (2.80), the local field enhancement factor, $|F|^2$ can be defined as [101]

$$|F|^2 = \frac{|E|^2}{|\mathrm{E}_0|^2} = \left| \frac{\varepsilon_M - \varepsilon_d}{\varepsilon_M + 2\varepsilon_d} \right|^2 \frac{R^6(1+3\cos^2\theta)}{r^6}. \tag{2.81}$$

In this expression, ignoring the angular dependence is acceptable because the modulus square of electric field gradually decreases as $|E|^2 \propto 1/r^6$. In this perspective, the local field enhancement F, is given by [107]

$$F = \frac{\varepsilon_M - \varepsilon_d}{\varepsilon_M + 2\varepsilon_d} \frac{R^3}{r^3}. \tag{2.82}$$

2.7 Core-shell nanocomposites

There are several types of core-shell nanoparticles with many different uses. Their classification is based on their properties and applications. Thus, carefully categorizing core-shell NCs as per these criteria and investigating their characteristics is not an easy task. In this section, we tried reviewing core-shell nanoparticles according to their material characteristics. In a broader perspective, it is obvious that organic or inorganic material can be utilized to form the core or shell of a core-shell composite. According to their material properties from which they are made of, core-shell nanoparticles can be divided into four main classes: (i) inorganic-inorganic; (ii) inorganic-organic; (iii) organic-inorganic; (iv) Organic-organic [108].

Inorganic-inorganic core-shell categories are extensively used to increase semiconductor efficiency, quantum dots, optoelectronics, information storage, optical bioimaging, catalysis, etc. Additionally, among various types of inorganic-inorganic core-shell nanomaterials, generally, cores and shells can be made from silica, metal oxide, metal, or other inorganic materials. Some of the examples include CdSe-CdS, Au-SiO_2, CdSe-ZnS, CdTe-CdSe, CdSe-ZnSe-ZnS, and CdSe-SiO_2.

Inorganic-organic nanocomposites have a core comprised of metal, a metallic compound, metal oxide, silica, and a polymer or other high density organic material as a shell on top. Some examples of this type of core-shell NCs include Au-PSMA, Fe_3O_4-PEG, Fe-PIB, SiO_2-PS, where PSMA, PEG, PIB and PS denote polystyrene methacrylate, polyethylene glycol, polyisobutylene, and polystyrene, respectively. Coating the inorganic material with an organic layer has numerous advantages. One illustration is that the improved oxidation stability of a metal core can prevent the oxidation of surface atoms to metal oxide in a typical environment [109, 110]. Moreover, they can also show improved biocompatibility for use in biological applications [111–114].

The other type of core-shell NCs is organic-inorganic type which are structurally just

the reverse of inorganic-organic core-shell type explained above. These kinds of materials typically possess both the inorganic and organic features [115].
The inorganic material, particularly a metal oxide coating on an organic material, is advantageous in a number of ways, including enhanced material strength [116], oxidation resistance, thermal stability, colloidal stability [117], and other types of resistance [118]. These particles can also increase the brittleness of inorganic particles and simultaneously exhibit polymeric features such as outstanding optical qualities, flexibility, and toughness [119]. Because of their plentiful uses in numerous areas of material science, such as paints, magnetic fluids, catalysis, microelectronics, and biotechnology, this form of core-shell nanoparticles has recently been shown to be of significant study interest [120].

The fourth category are organic-organic core-shell NCs. In this classification, the core and shell materials comprise a polymer or another organic material. They are referred to as "smart particles" and have a variety of uses in various disciplines, such as drug delivery [121], biosensing [122], chemical separation [123], biomaterials [124, 125], and catalysis [126]. The importance of coating one polymer with another improves the physical behavior for instance, toughness of the material as a whole [127]. Few examples of this kind of core-shell NCs are polyphenylene-PEO and PTBA-PS where, PEO and PTBA are polyethylene oxide and poly-tert-butyl acrylate, respectively.

2.8 Quantum dots

A quantum dot consists of a semiconductor core which is necessary for the fundamental optical characteristics such as emission and absorption of light. The luminescence of quantum dots is caused by the quantum confinement and defects in the crystalline structure of quantum dots [128]. From this perspective, quantum dots can be tuned like metal nanoparticles to absorb and/or scatter different colors (Fig. (2.6)).

Quantum confinement effect refers to electrons and holes being spatially restricted in

Figure 2.6: Schematic of tuned QDs absorbing and scattering different colors.

a material whose dimensions fall within the range of or smaller than the exciton Bohr radius of that material.The bulk exciton Bohr radius is the physical separation that naturally exists in a crystal between the electron in the conduction band and the hole it creates in the valence band. Under quantum confinement conditions, energy levels may be treated as discrete and the band gap becomes size dependent, increasing as the nanocrystal size decreases.

On the other hand, the defects on the surface of the nanocrystal can reduce luminescence of the dots because atoms on the quantum dot surface have dangling bonds which trap electrons after absorbing a quantum of energy. Relaxation of the electron-hole system occurs in this case by nonradiative way and as a result the luminescence quantum yield of quantum dots is significantly reduced. For these reasons it is crucial to manage the quality of a quantum dot surface by overcoating it with the second semiconductor layer or shell [129].

Depending on the the alignment of the edge of the conduction and valence bands, core-

shell QDs are categorized into four major classes as follows: type I, inverse type I, type II, and inverse type II (Fig. 2.7). It can be observed as we move from type I to type

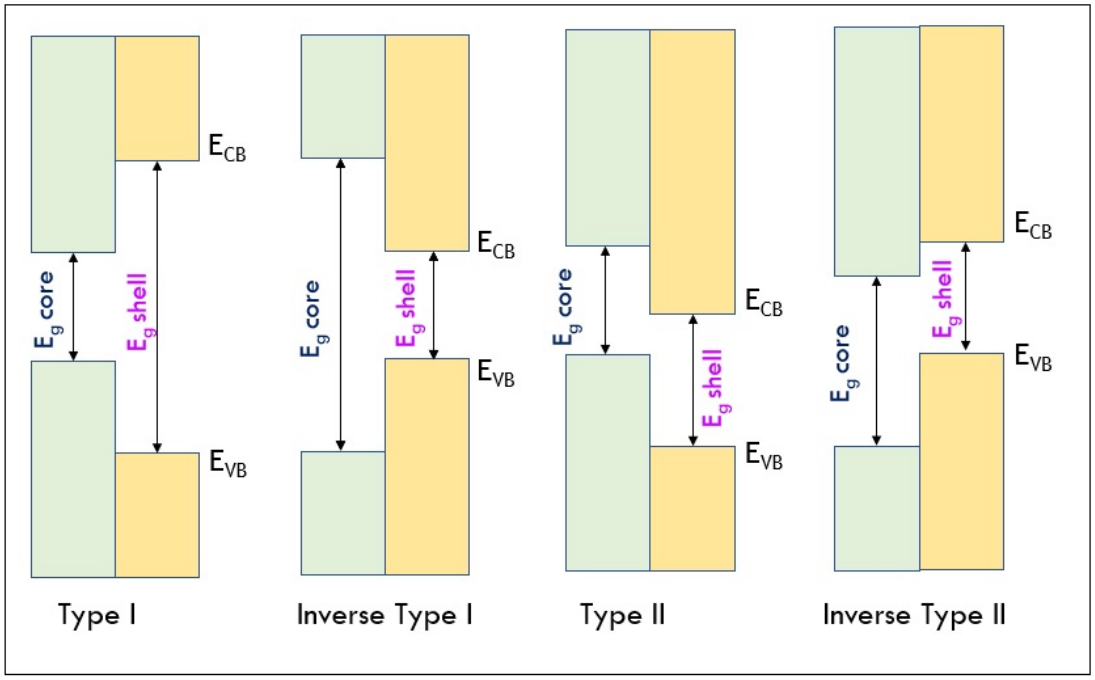

Figure 2.7: Schematic representation of band alignment of various types of core-shell QDs [130]

II, the bandgap difference between core and shell reduces and the exited electrons are spatially separated from each other. In type I core-shell QDs, the bandgap energy of the core material is narrower than of the shell material. Since the conduction and valence band boundaries of the core are situated within the energy gap of the shell, the electrons and holes are constrained within the core region.

Moreover, the valence band of the core in type I is located at higher energy than that of shell. This type of configuration of energy levels is important to restrict electrons and holes within the core material. The purpose of coating with shell is to passivate the core surface thereby improving its overall optical properties. Separating the more optically active core surface from its surroundings is another function of the shell. Moreover, the larger bandgap shell material improves the stability against photo bleaching of the core of semiconductor material. However, when the shell layer becomes thicker, the

material surface activity of the core surface decreases, thereby lowering the quantum yield. When the thickness of the shell layer increases, a small red shift is observed in the UV-vis absorption spectra [108].

As clearly explained (Table: 2.1), both hole and electron charges in inverse type I are

Table 2.1: Characteristics of various types of core-shell QDs [108,131,132].

Parameter	Type I	Inverse Type I	Type II	Inverse Type II
Bandgap	The band gap of the shell material is wider than the band gap of the core material. The electrons and holes are confined within the core region.	The band gap of the core is greater than the band gap of the shell. The band gap of the shell falls within band gap of the core.	Valence band edge of the core is within the band gap of the shell or conduction band edge of the shell is within the band gap of the core.	Conduction band edge of the core is within the band gap of the shell or valence band edge of the shell is within the band gap of the core.
Positions of excited electrons and holes	Excited electrons and holes are completely confined within the core region.	Excited electrons and holes are partially or completely confined in the shell depeding on the thickness of the shell.	One carrier is mostly confined to the core, the other confined to the shell, leading to electrons and holes on different sides of the heterojunction.	One of the excited electrons or holes are delocalized in the core-shell structure, and the other one is confined within the core.
Limitations	Increasing the shell thickness reduces the material surface activity of the core surface leading to a decrease in a photoluminescence emission.	Both the excited electrons and holes may leak to the surface.	Prolonged photoluminescence decay time due to the lower overlap of the electron and hole wavefunctions.	The excited electron or hole can be absorbed leading to reduced decay time, one carrier is mostly confined to the core, the other to the shell.
Examples	CdSe/CdS, CdSe/ZnS, CdTe/CdS	CdS/CdSe, ZnS/CdSe, CdS/HgS	ZnTe/ZnSe, PbSe/CdSe, PbTe/CdTe	InP/CdS, PbS/CdS

partially delocalized on the shell materials and emission wavelengths can be tuned by altering the shell thickness. These kinds of materials have lower quantum yields and higher resistance against photo bleaching. However, its quantum yield can be increased by coating another larger bandgap semiconductor material. In type II QDs, either the conduction or valence band of the core could be generally found within the bandgap of the shell (Fig. 2.7). Because of this, one carrier is primarily contained in the core, whereas the other is primarily contained in the shell. Hence, the electrons and holes on the various sides of the heterojunction tend to be spatially separated by the energy gradient present at the interfaces. (Table: 2.1) [133]. Due to this spatial separation of the electrons and holes, this type of QD is anticipated to exhibit numerous novel

features, including longer exciton decay times than type I NCs. For instance, these arrangements can provide access to wavelengths that a single material cannot otherwise access. In addition, due to the separation of charges in the lowest excited states, type II nanomaterials are more suited for photovoltaic or photoconduction applications.

Since core-shell composites have a lower effective band gap than comparable pure core and shell materials, the optical properties of such materials can easily be controlled by varying the thickness of the shell. The efficiency of semiconductor nanomaterials can be determined largely by two essential parameters, namely, the quantum yield and the response time. For semiconductor materials, quantum yield can be defined as the ratio of emitted to absorbed photons. The quantum yield is typically small for a single semiconductor particle. However, the quantum yield rises when the specific material is covered with a composite of higher band gap energy semiconducting material [50, 52, 134].

2.9 Importance of core-shell nanoparticles

Since core-shell nanoparticles have evolved at the interface between materials chemistry and numerous other fields, including electronics, biomedicine, pharmaceuticals, optics, and catalysis, they are steadily gaining more and more attention. They are extremely useful materials with improved properties. Under some conditions, the qualities resulting from the core or shell materials are found to be very unique. New and desirable properties can be achieved by altering the constituent materials or the core to shell ratio [47]. By coating the core with the shell material, the characteristics of the core particles such as reactivity or thermal stability can be altered thereby improving the overall particle stability and dispersibility. Ultimately, the composite system exhibits distinctive qualities resulting from the various materials used in combination. This is particularly essential with regards to the inherent capacity to adjust the surface functionalities andÂă satisfy the various application needs [135, 136]. The advantage of coating on the core material include surface modification, the ability to improve

functioning, stability, and dispersibility, controlled core release, decreased consumption of precious resources, and more.

The study of many researchers demonstrate that core-shell composites can be utilized in diverse applications [137] including biomedical [138–140], pharmaceutical, [136], in catalysis [141], electronics [142, 143], photoluminescence enhancement [144, 145], producing photonic crystals [146], etc. Specifically, in the biomedical industry, most of these particles are utilized for bioimaging [147–150], controlled release of drugs [151, 152], targeted drug delivery [150, 153], labelling of cells [154, 155], and tissue engineering purposes [152, 156].

In addition to modifying material properties as desired, core-shell materials are also essential from an economic perspectives. A precious material can be coated over a cheaper one to use less of the expensive material than producing the same sized pure material. Moreover, hollow particles can be produced by using core-shell composites as a template after the core has been removed via calcination or dissolution.

Chapter 3

Theoretical Models and Methods

This Chapter describes the basic theoretical models and methods used in this study. Moreover, technical procedures employed and software resources used in plotting the numerical results of the study are also presented.

3.1 Theoretical bases

After Maxwell's unification of electricity and magnetism in 1864 and the discovery of the electromagnetic nature of light, a possibility opened to connect between the optical and dielectric properties of matter. This means that the effective optical properties of heterogeneous matter could be derived from polarisability considerations of the inclusions in the mixture. For nanocomposites, Maxwell Garnett derived the famous relation between the effective dielectric constant of a medium where spherical particles, having given optical properties, occupy randomly positioned a given volume fraction in the host medium [91]. Since then, the analyses of the effective properties of mixtures became more well-defined and exact by the early 20^{th} century. In this dissertation, since the materials of our study consist of nanocomposite systems, we have used the Maxwell garnet formalism for effective permittivity and polarizability.

One of the ways to the optical properties of materials is to consider their dielectric functions. The initial interaction of light with matter, expressed by the frequency dependent

dielectric function of the particle material, enters the electrodynamic scattering model and yields characteristic spectra that are determined by the material specific properties, the particle specific topological properties and statistics. The enormous practical advantage of any electrodynamic scattering model is that it enables one to compute numerically the optical response for arbitrary realistic particle materials. The Lorentz model is a widely used model in solid state physics, and it predicts the frequency dependence of the permittivity function. Another special case of the Lorentz model is the Drude model, used to describe the optical properties of metals.

Paul Drude used Maxwell's theory and Sommerfeld model [79] to explain the properties of electrons in metals [157] and the model has also been adapted for semiconductors [158, 159]. Over the years, this fact has brought to think in terms of a model in which the electrons are relatively free and can move under the influence of electric fields. It is the simplest classical treatment of optical properties of metals and is based on the kinetic theory of an electron gas in a solid. It is assumed that all the electrons have the same average kinetic energy [160], and the model neglects electron-electron interactions and interband (interzone) transitions. As a result, the dielectric behavior of metals is specified by the collective excitation of the free electron charges under influence of an external EM field.

Another model is the Drude-Lorentz model which takes into account the separated interband, *i.e.*, bound electron effects. It extends the range of the method validity by inserting the separated interband expressions into the Drude model. In this model, the bound electrons in a metal contribute to harmonic oscillators and the dielectric function behavior. Due to this, for the mathematical and numerical analyses of metal dielectric functions in our study, we have used Drude-Lorentz model, particularly that is represented by Eqn. (2.34) in combination with Eqns. (2.35) and (2.36).

3.2 Core-shell models

The core-shell type nanoparticles can be broadly defined as comprising a core (inner material) and a shell (outer layer material). These can consist of a wide range of different combinations in close interaction, including inorganic-inorganic, inorganic-organic, organic-inorganic, and organic-organic materials. The choice of shell material of the core-shell nanoparticle is generally strongly dependent on the end application and use [108].

Different classes of core-shell nanoparticles are shown schematically in Figure (3.1).

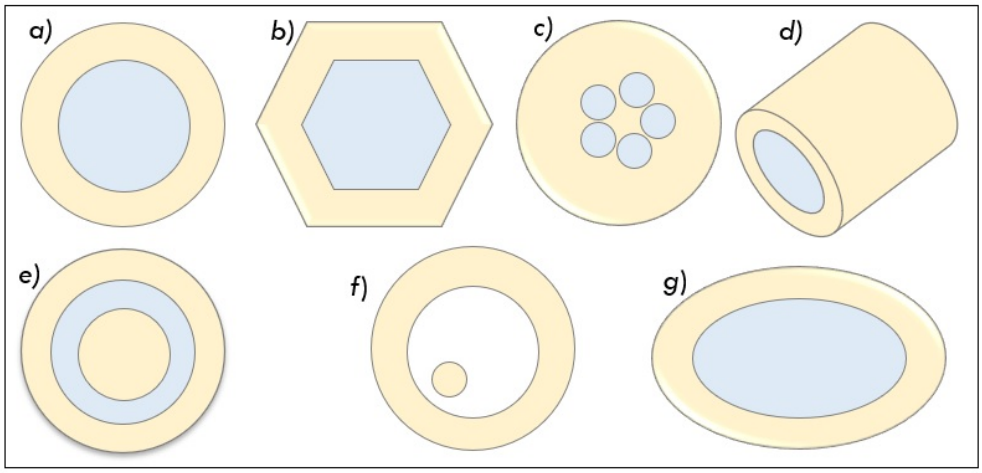

Figure 3.1: Schematics of different core-shell nanoparticles. (a) Spherical, (b) hexagonal, (c) multiple core, (d) cylindrical, (e) nanomatryushka or multilayered metallodielectric, (f) movable core in hollow shell, and (f) ellipsoidal core-shell nanoparticles.

Concentric spherical core-shell nanoparticles are the most common where a simple spherical core particle is completely coated by a shell of a different material.

Different shaped core-shell nanoparticles have also given rise to immense research interest because of their different novel properties. Different shaped core-shell nanoparticles are generally formed when a core is nonspherical as shown in figure (3.1(b)). Core-shell structures of multiple core type particles are formed when a single shell material is coated onto many small core particles together as shown in figure (3.1(c)). Concentric nanoshells of alternative coating of dielectric core and metal shell mate-

rial onto each other (A-B-A type) are also one of the possible models, as shown in figure (3.1(e)). Here, nanoscale dielectric spacer layers separate the concentric metallic layers. These types of particles are also known as multilayered metallodielectric nanostructures or nanomatryushka and are mainly important for their plasmonic properties [161–164]. In our study, we used the models presented in figure 3.1(a), (d), (e), and (g), where in case (e), our schematic model consists of three layers of different materials. Specifically, we used the spherical core-shell models of CdSe@Ag and CdSe@ZnSe@Ag to investigate the effects of size on the LFEF of core-shell structure. To study how the optical properties of core-shell NCs are affected by the shape of nanostructures, we have also studied spherical, cylindrical, prolate, and oblate CdSe@Au core-shell NCs.

3.3 Laplace's equation in various coordinate systems

Changing the morphology of NCs resulted in changing the symmetry order, which has a dramatic effect on the distribution of the polarization charges over the surface area of the nanostructures [131, 165, 166]. Many-fold symmetry nanoparticles exhibit most interesting selective optical features in the visible and near infrared ranges. Their morphologies exhibit different polarization factors along each symmetry axis. The solution to such problems can be found using Laplace's equation.

3.3.1 Laplace's equation in spherical coordinates

Laplace's equation is one of the most significant equations in a wide variety of fields including thermodynamics and electrodynamics. It can be used to solve problems in various coordinate systems such as rectangular, cylindrical, spherical, and polar forms. To find the expressions for electric potentials in different regions of spherical core-shell nanocomposites, let us start by considering a source free medium, where Laplace equation is given by

$$\nabla^2 \Phi = 0. \tag{3.1}$$

Writing this for spherical coordinate system (r, θ, ϕ), the Laplace's equation becomes

$$\frac{1}{r}\frac{\partial^2}{\partial r^2}(r\Phi) + \frac{1}{r^2 \sin\theta}\frac{\partial}{\partial\theta}\left(\sin\theta\frac{\partial\Phi}{\partial\theta}\right) + \frac{1}{\mathrm{r}^2\sin^2\theta}\frac{\partial^2\Phi}{\partial\phi^2} = 0 \tag{3.2}$$

The, by applying the Legendre equation and Legendre polynomials with all the associated assumptions and conditions, the general solution of Eqn. (3.2) is given by [93]

$$\Phi(\mathrm{r},\theta) = \sum_{l=0}^{\infty}(A_l r^l + B_l r^{-l-1})P_l(cos\ \theta), \tag{3.3}$$

where the coefficients A_l and B_l can be determined by the boundary conditions.

Let the external field $\mathbf{E} = \mathbf{E}_0 \exp(-i\omega t)$ is incident on a multilayer core-shell NCs of spherical symmetry, as shown in Fig. 3.2. From the boundary condition at infinity,

$$\Phi = -\mathbf{E}_0\, z = -\mathbf{E}_0\, r\cos\theta.$$

The unknown amplitudes A and B fields in each region can be determined by using

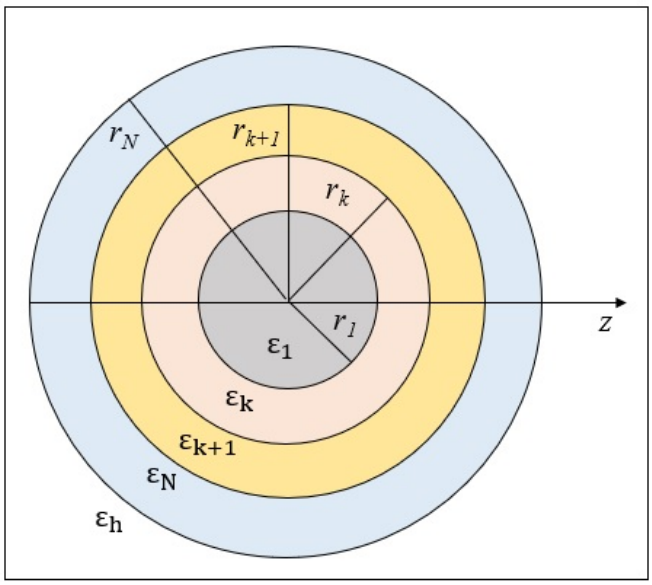

Figure 3.2: Multilayer spherical core-shell

boundary conditions. If the potential in the k^{th} region with dielectric permittivity ε_k is

Φ_k, then from the continuity of tangential electric fields

$$\frac{\partial \Phi_k}{\partial \theta} = \frac{\partial \Phi_{k+1}}{\partial \theta} \qquad \text{at } r = r_{k+1}. \tag{3.4}$$

Similarly, from normal component of the electric field displacement, the boundary condition satisfies

$$\varepsilon_{\mathrm{k}} \frac{\partial \Phi_k}{\partial r} = \varepsilon_{k+1} \frac{\partial \Phi_k + 1}{\partial r} \qquad \text{at } r = r_{\mathrm{k+1}}. \tag{3.5}$$

From N boundaries, there are $2N$ equations to find the unknowns. Outside the most outer shell (in the embedding host), only the dipole field amplitude is unknown. The constant field component is the known incident field. As an example, let us apply this formula for $N = 1$ (homogeneous sphere) and $N = 2$ (core and single shell) cases and find the expression for electric potential distribution, Φ_i in each region.

For the homogeneous sphere ($N = 1$)

$$\Phi_1 = -E_0 \frac{3\varepsilon_h}{\varepsilon_1 + 2\varepsilon_h} r \cos\,\theta, \tag{3.6}$$

and

$$\Phi_h = -E_0 r \cos\,\theta + E_0 \left(\frac{\varepsilon_1 - \varepsilon_h}{\varepsilon_1 + 2\varepsilon_h} \right) \frac{r_1^3}{r^2} \cos\,\theta. \tag{3.7}$$

For spherical core and single shell ($N = 2$)

$$\Phi_1 = -\frac{9\varepsilon_2 \varepsilon_h}{(\varepsilon_1 + 2\varepsilon_2)(\varepsilon_2 + 2\varepsilon_h) + 2f(\varepsilon_1 - \varepsilon_2)(\varepsilon_2 - \varepsilon_h)} E_0\, r \cos\,\theta, \tag{3.8}$$

$$\Phi_2 = -E_0 \frac{3\varepsilon_3 \left[(\varepsilon_1 + 2\varepsilon_2) + 2(\varepsilon_1 - \varepsilon_2)\, (\frac{r_1}{r})^3 \right]}{(\varepsilon_1 + 2\varepsilon_2)(\varepsilon_2 + 2\varepsilon_h) + 2f(\varepsilon_1 - \varepsilon_2)(\varepsilon_2 - \varepsilon_h)}\, r \cos\,\theta, \tag{3.9}$$

and

$$\Phi_h = -E_0\, r \cos\,\theta + E_0 \frac{[(\varepsilon_1 + 2\varepsilon_2)(\varepsilon_2 - \varepsilon_3) + f(\varepsilon_1 - \varepsilon_2)(\varepsilon_3 + 2\varepsilon_2)]}{(\varepsilon_1 + 2\varepsilon_2)(\varepsilon_2 + 2\varepsilon_h) + 2f(\varepsilon_1 - \varepsilon_2)(\varepsilon_2 - \varepsilon_h)}\, \frac{r_2^3}{r^2} \cos\,\theta. \tag{3.10}$$

where $f = (r_1/r_2)^3$.

3.3.2 Laplace's equation in ellipsoidal coordinates

In uniform external electric field, problems related to ellipsoids can be solved by relating the ellipsoidal coordinates with Cartesian system. Let us consider core-shell ellipsoid of N layers all with different dielectric permittivites, and the whole NCs embedded in a host medium of permittivity ε_h as shown in Fig. 3.3.

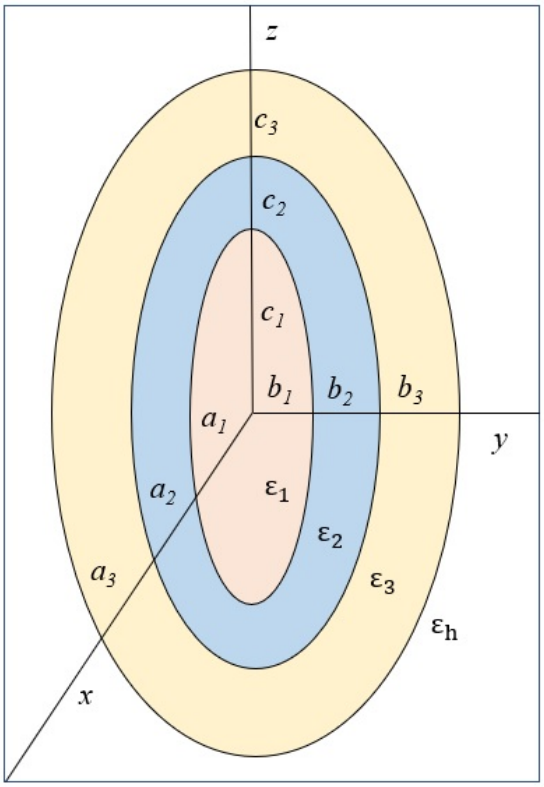

Figure 3.3: Multilayer ellipsoidal core-shell

The incident field is directed along the z-axis of the ellipsoid. To solve for internal fields in the multilayers of ellipsoidal core-shell NCs by Laplace's equation, the boundaries between the layers have to be constant-coordinate surfaces in the ellipsoidal coordinate system (confocal), so that we can use separation of variables. The equation

that relates these coordinates can be given by

$$\frac{x^2}{a^2+u^2}+\frac{y^2}{b^2+u^2}+\frac{z^2}{c^2+u^2}=1 \quad (a>b>c). \tag{3.11}$$

This equation has three different real roots ξ, η, and ζ which lie in the ranges of

$$\xi \geq -c^2,\ -c^2 \geq \eta \geq -b^2,\ -b^2 \geq \zeta \geq -a^2. \tag{3.12}$$

These three roots are the ellipsoidal coordinates of the point x, y, and z. The coordinate ξ is the root that lies in the range $\xi \geq -c^2$ shows that c is the smallest of the ellipsoid axes a, b, and c. The surfaces of constant ξ, η, and ζ are respectively ellipsoids and hyperboloids of one and two sheets, all confocal with the ellipsoid

$$\frac{x^2}{a^2}+\frac{y^2}{b^2}+\frac{z^2}{c^2}=1. \tag{3.13}$$

One surface of each of the three families passes through each point in space, and the three surfaces are orthogonal. The confocality requirement of the multilayer ellipsoid means that the semiaxes a_i, b_i, and c_i of each of the N ellipsoidal boundaries have to satisfy the following:

$$a_i^2-a_j^2=b_i^2-b_j^2=c_i^2-c_j^2 \tag{3.14}$$

for all pairs i, j. Using the one to one correspondence relation between (x,y,z) and the three roots (ξ,η,ζ), we can find

$$\begin{aligned} x^2 &= \frac{(a^2+\xi)(a^2+\eta)(a^2+\zeta)}{(b^2-a^2)(c^2-a^2)}, \\ y^2 &= \frac{(b^2+\xi)(b^2+\eta)(b^2+\zeta)}{(a^2-b^2)(c^2-b^2)}, \\ z^2 &= \frac{(c^2+\xi)(c^2+\eta)(c^2+\zeta)}{(a^2-c^2)(b^2-c^2)}. \end{aligned} \tag{3.15}$$

The surfaces $\xi =$ constant are confocal ellipsoids, and the particular ellipsoid $\xi = 0$ coincides with the boundary of the particle (Fig. 3.4(a)). The surfaces $\eta =$ constant are

hyperboloids of one sheet (Fig. 3.4(b)) and the surfaces $\zeta =$ constant are hyperboloids of two sheets (Fig. 3.4(c)) (adopted from [167]).

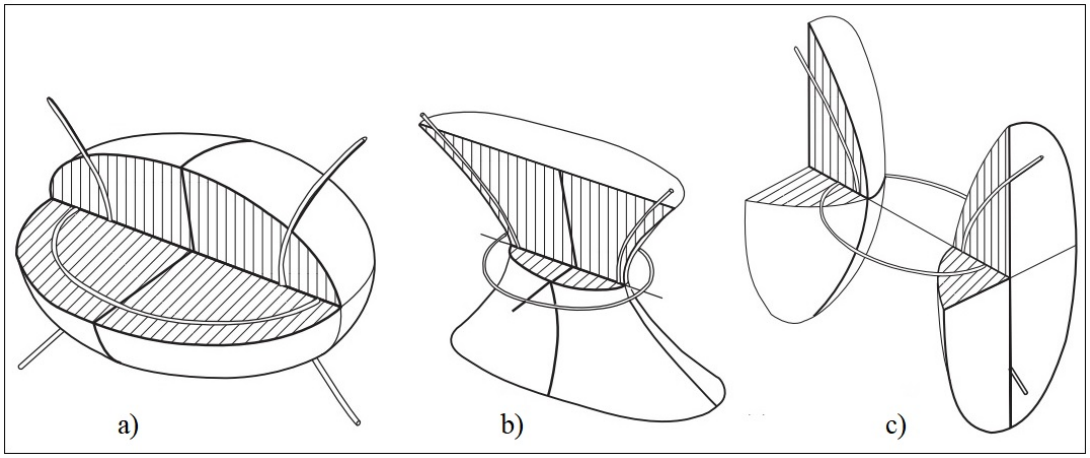

Figure 3.4: Conics. (a) An ellipsoid, (b) a hyperboloid of one sheet, and (c) a hyperboloid of two sheets, reproduced from [158].

In ellipsoidal coordinate, the potential of uniform incident field of amplitude E_0 directed along z- axis (c -axis of the layered ellipsoid) is

$$\Phi_0 = -E_0 z = -E_0 \sqrt{\frac{(c^2+\xi)(c^2+\eta)(c^2+\zeta)}{(a^2-c^2)(b^2-c^2)}}. \tag{3.16}$$

To obtain the expression for the potential in the presence of the ellipsoid, separate the incident potential from the total potential Φ as

$$\Phi = \Phi_0 F(\xi). \tag{3.17}$$

In this function, the dependence of potentials on η and ζ are the same as in Φ_0. This helps to satisfy the boundary condition at $\xi = 0$ for arbitrary η and ζ. Hence, $F(\xi)$ is the only dependent on ξ, and can be approached from Laplace's equation. In ellipsoidal coordinates, Laplace's equation is given by [60]

$$(\eta-\zeta)f(\xi)\frac{\partial}{\partial\xi}\left(f(\xi)\frac{\partial\Phi}{\partial\xi}\right)+(\zeta-\xi)f(\eta)\frac{\partial}{\partial\eta}\left(f(\eta)\frac{\partial\Phi}{\partial\eta}\right)+(\xi-\eta)f(\zeta)\frac{\partial}{\partial\zeta}\left(f(\zeta)\frac{\partial\Phi}{\partial\zeta}\right)=0 \tag{3.18}$$

Substituting Eqn. (3.17) in to Laplace's equation, we can write for $F(\xi)$ as [168]

$$\frac{d^2F}{d\xi^2}+\frac{dF}{d\xi}\frac{d}{d\xi}\log\left[R_\xi(\xi+c^2)\right]=0. \tag{3.19}$$

The Laplace equation with this kind of separable potential has two solutions. One solution of this equation is F = constant, and the other is

$$F(\xi)=\int_\xi^\infty \frac{d\xi}{(\xi+c^2)R(s)}, \tag{3.20}$$

where

$$R(s)=\sqrt{(s+a^2)(s+b^2)(s+c^2)}. \tag{3.21}$$

At sufficiently large distances from the particle ($\xi \gg a^2$), the perturbing potential is negligible and hence, $\xi \approx r^2$. Due to confocality, the parameters a, b and, c can be a_i, b_i, and c_i of the ellipsoidal surfaces. Solving for $F(\xi)$ and substituting in to Eqn. (3.17) gives the general solution of potential in the homogeneous region as

$$\Phi=\Phi_0\left[C-\frac{D}{2}\int_\xi^\infty \frac{ds}{(s+c_1^2)R_1(s)}\right], \tag{3.22}$$

with

$$R_1(s)=\sqrt{(s+a_1^2)(s+b_1^2)(s+c_1^2)}, \tag{3.23}$$

where a_1, b_1, and c_1 are the semiaxes of the whole scatterer ellipsoid, the coefficients C and D are to be determined from the boundary conditions.

Applying the boundary conditions, the tangential electric field comes from the derivative of the potential with respect to the coordinates η and ζ. Hence, the potential and the factor

$$C-\frac{D}{2}\int_\xi^\infty \frac{ds}{(s+c_1^2)R_1(s)}, \text{ have to be continuous.}$$

The normal displacement field has also to be continuous across a boundary. The normal

component of the displacement **D** is

$$\mathbf{n}\cdot\mathbf{D} = -\varepsilon\frac{1}{h_\xi}\frac{\partial\Phi}{\partial\xi}, \tag{3.24}$$

where h_ξ is the metric coefficient of the ellipsoidal coordinate system

$$h_\xi = \frac{\sqrt{(\xi-\eta)(\xi-\zeta)}}{2R_1(\xi)} \tag{3.25}$$

Considering the potential in Eqn. (3.22), the equation of continuity applies to the following quantity [169]

$$\varepsilon\frac{\partial}{\partial\xi}\left(\sqrt{\xi+c_1^2}\left[C-\frac{D}{2}\int_\xi^\infty\frac{ds}{(s+c_1^2)R_1(s)}\right]\right), \tag{3.26}$$

where the term $\sqrt{\xi+c_1^2}$ comes from the z- dependent potential, Φ_0. Now, differentiating it indicates that the expression

$$\varepsilon\left[C+\frac{D}{R_1(\xi)}-\frac{D}{2}\int_\xi^\infty\frac{ds}{(s+c_1^2)R_1(s)}\right] \tag{3.27}$$

is continuous across a boundary.

We can generalize this to the potential in the k$^{\text{th}}$ region as

$$\Phi_k = -E_0 z\left[C_k-\frac{D_k}{2}\int_\xi^\infty\frac{ds}{(s+c_1^2)R_1(s)}\right], \tag{3.28}$$

where C_k denotes the constant field amplitude, or the propagating wave, D_k stands for the dipole term. The term ε_k and ε_{k+1} are permittivities of ellipsoid with semiaxes a_{k+1}, b_{k+1}, and c_{k+1} , where the coordinate ξ has the value ξ_{k+1}. Using the boundary condition, we have

$$C_k-\frac{D_k}{2}\int_{\xi_{k+1}}^\infty\frac{ds}{(s+c_1^2)R_1(s)} = C_{k+1}-\frac{D_{k+1}}{2}\int_{\xi_{k+1}}^\infty\frac{ds}{(s+c_1^2)R_1(s)} \tag{3.29}$$

and

$$\varepsilon_k \left[C_k + \frac{D_k}{R_1(\xi_{k+1})} - \frac{D}{2} \int_{\xi_{k+1}}^{\infty} \frac{ds}{(s+c_1^2)R_1(s)} \right] = \varepsilon_{k+1} \left[C_{k+1} + \frac{D_{k+1}}{R_1(\xi_{k+1})} - \frac{D}{2} \int_{\xi_{k+1}}^{\infty} \frac{ds}{(s+c_1^2)R_1(s)} \right] \tag{3.30}$$

Since a_1, b_1, and c_1 are bases of the coordinate system, the value of ξ at the boundary of the ellipsoid is zero (i.e., $\xi_1 = 0$). Therefore, at the lower limit ξ_1 we can write

$$\int_{\xi_1}^{\infty} \frac{ds}{(s+c_1^2)R_1(s)} = \int_0^{\infty} \frac{ds}{(s+c_1^2)\sqrt{(s+a_1^2)(s+b_1^2)(s+c_1^2)}} = \frac{2}{a_1 b_1 c_1} L_z^{(1)}, \tag{3.31}$$

where $L_z^{(1)}$ is the depolarization factor $z-$axis. Generally, the depolarization factors along all the three axes of the ellipsoid in the i^{th} region are given by

$$\begin{aligned} L_x^{(i)} &= \frac{a_i b_i c_i}{2} \int_0^{\infty} \frac{ds}{(s+a_i^2)R_1(s)}, \\ L_y^{(i)} &= \frac{a_i b_i c_i}{2} \int_0^{\infty} \frac{ds}{(s+b_i^2)R_1(s)}, \\ L_z^{(i)} &= \frac{a_i b_i c_i}{2} \int_0^{\infty} \frac{ds}{(s+c_i^2)R_1(s)}. \end{aligned} \tag{3.32}$$

where

$$L_x + L_{yx} + L_z = 1. \tag{3.33}$$

For the sphere ($a = b = c$), from the symmetry, we can write

$$L_x = L_y = L_z = \frac{1}{3}. \tag{3.34}$$

For a cylinder with its axis in the $x-$direction ($a \to \infty$), we have

$$L_x = 0, \qquad L_y = L_z = \frac{1}{2}. \tag{3.35}$$

3.4 Quasi-static approximation

If the size "a" of a given particle is much smaller than the wavelength, λ, of the incident driving field, the variation of the phase of this field across the particle is negligible, so an incident plane wave can be approximated by a constant field. This is known as the quasi-static approximation, because it allows retardation effects to be ignored. Under this approximation, Maxwell's equations can then be solved in terms of an electric potential, Φ, where $E = -\nabla\Phi$. For a driving field applied in the z-direction, the applied potential is $\Phi = -Ez$, or, in polar coordinates, $\Phi = -E\ r\cos\theta$. Potentials inside and outside of the metal particle can be written in terms of Legendre polynomials $P(\theta)$ as [170]

$$\Phi_{in}(r,\theta) = \sum_{l=1}^{\infty} A_l\ r^l P_l(\cos\theta), \qquad \text{for } r \leq a$$

and

$$\Phi_{out}(r,\theta) = -E\ r\cos\theta + \sum_{l=1}^{\infty} B_l\ r^{-(l+1)} P_l(\cos\theta), \qquad \text{for } r \geq a,$$

where a is the radius of the particle.

Applying the boundary conditions that the potential and the normal component of $\boldsymbol{D}$ are continuous at $r = a$, we get

$$\begin{aligned}
&l = 0: \ \ A_0 = B_0 = 0, \\
&l = 1: \ \ A_1 = \frac{-3\varepsilon_{out}}{\varepsilon_{in} + 2\varepsilon_{out}} E, \quad B_1 = \frac{(\varepsilon_{in} - \varepsilon_{out})}{\varepsilon_{in} + 2\varepsilon_{out}} E\, a^3, \\
&l > 1: \ \ \frac{-\varepsilon_{out}}{\varepsilon_{in}} \frac{l+1}{l} = 1, \ \ A_l = \frac{B_l}{a^{2l+1}}.
\end{aligned}$$

In these expressions, ε_{in} is the dielectric function of the metal particle and ε_{out} is the dielectric function of the surrounding medium. For a spherical nanoparticle of radius a placed in the external embedding medium, ε_{in} represents the dielectric function of the sphere, while ε_{out} is the permittivity of the host medium.

There is no constant ($l = 0$) term, as such a term would represent a net charge on the

particle. For $l = 1$, there is a response at any frequency, provided there is a driving field to excite the particle. However, when $Re[\varepsilon_{in} + 2\varepsilon_{out}] = 0$, A_1 and B_1 take on large values. In the absence of damping (*i.e.*, for $Im[\varepsilon_{in}] = Im[\varepsilon_{out}] = 0$), the coefficients become singular, indicating that a mode exists that is excited for arbitrarily small driving fields. For $l > 1$, the response is independent of E, indicating that higher order modes cannot be excited by a constant field. The metal nanoparticle thus acts like a dipole.

Under the quasi-static approach, we calculated LFEF, absorption and extinction cross-sections in spherical, cylindrical and ellipsoidal core-shell NCs. By using the optical constants of the materials used in the study, the graphs that show the optical properties are plotted using the statistical software package called Mathematica. Finally, all the results are discussed and conclusions are drawn for each of the findings.

Chapter 4

Size Dependent Local Field Enhancement Factor of CdSe Based Core-Shell Spherical Nanoparticles

4.1 Introduction

Recent studies show that core-shell nanocomposites have attracted increasing research interest due to their outstanding properties such as versatility, tunability, and stability [171, 172]. A core-shell nanocomposite consists an inner core and outer shell(s) that is composed of different materials. The combination of different material properties in a single core-shell system leads to several novel properties for potential applications in various fields such as electronics, optics, biomedicine, environmental science, materials, energy, magnetism, and catalysis [173, 174]. Moreover, the properties of these core-shell materials can be easily tuned by varying the size, shape, morphology as well as the type of the core, shell, and embeding medium [175–177].

Among the widely studied core-shell nanocomposites is the CdSe-based quantum dots (QDs). In particular, the emission intensity of CdSe QDs can be increased several times when it is capped with a ZnS shell to form a CdSe-ZnS core-shell structure [178]. In addition, CdSe nanocrystals are considered as the most promising emitting materials

in the visible spectral region because their emission color can dramatically be adjusted from blue to red. Wide band gap semiconductors such as ZnS, CdS, and ZnSe can be used as the shell material [179] to cap a CdSe core. But, among these semiconductors, ZnSe over coated CdSe nanoparticles have shown advantages that not only the bandgap of ZnSe (2.72 eV) is larger than that of CdSe (1.76 eV), but also it has shown low toxicity as compared to CdS and ZnS [180]. Moreover, its lattice parameter and binding energy are 5.67 A^o and 20 meV respectively, while the band gap alignment is of type I, where both electrons and holes are confined in the CdSe core [181–183]. The lattice parameter mismatch of ZnSe relative to the CdSe core (6.3%) is significantly smaller when compared with the most commonly used ZnS shell (10.6%) material [184, 185]. All these material parameters make ZnSe an excellent shell material to cap a CdSe core in a core-shell nanocomposite.

In support of this, experimental studies show that when CdSe is covered with ZnSe, the optical properties of the combination is enhanced [186]. It was also reported that CdSe@ZnSe core-shell quantum dot are novel materials incorporating CdSe core in a ZnSe shell [53]. For instance, the photoluminescence intensity of a CdSe@ZnSe core-shell nanocomposites can be significantly enhanced by coating (capping) the CdSe core with a few layers of ZnSe shell [187]. But, to the best of our knowledge, few or no theoretical and numerical studies were carried out to support those many experimental works. Moreover, as the heterostructures formed with metal and semiconductor composite nanostructures provide another efficient opportunity for tuning the unique optical properties of nanoparticles [188], the plasmonic effects are also found to be interesting. For CdSe based core-shell nanocomposites, the effect of the sizes of the core, the shell (metal), and the spacer (semiconductor) on the local field enhancement factor (LFEF) were not further studied yet. Hence, this study focuses on the theoretical and numerical investigations of the size dependent LFEF of CdSe@Ag and CdSe@ZnSe@Ag core-shell spherical nanoparticle embedded in the host matrix, SiO_2.

4.2 Theoretical models and calculations

4.2.1 Core and single shell spherical nanoparticles

When the size of a particle is much smaller than the wavelength of the incident electromagnetic radiation [189], the electric field may be considered to be spatially uniform over the whole range of the particle [190]. Consequently, the particle may be represented by an oscillating dipole and this is known as the quasi-static approximation [60, 191]. This approximation is important for a qualitative understanding of the interaction of light with nanoparticles as it considerably simplifies the mathematical analysis.

In this paper, we considered a model of spherical core@shell nanoparticle in the quasi-static limit. In this approach, the electrostatic solution can easily be calculated by solving the Laplace's equation. In our model, we separately considered CdSe@Ag and CdSe@ZnSe@Ag both embedded in a dielectric material. As shown in Fig. 4.1, the radius of the core is r_1 and its dielectric permittivity is ε_1. The shell is characterized by the radius r_2 and dielectric permittivity ε_2 (where $r_1 < r_2$). The embedding material (SiO_2) has an electric permittivity ε_3. The expressions needed to calculate the electric potential in the system under the quasi-static approach is given by [192, 193]. According to Eqns. (3.8), (3.9), and (3.10), the electric potential in the dielectric core, the shell, and the surrounding medium can be written as

$$\Phi_1(r,\theta) = -E_o A_1 r\cos\theta, \quad (r \le r_1), \tag{4.1}$$

$$\Phi_2(r,\theta) = -E_o\left(A_2 r - \frac{B_2}{r^2}\right)\cos\theta, \quad (r_1 \le r \le r_2), \tag{4.2}$$

$$\Phi_3(r,\theta) = -E_o\left(r - \frac{B_3}{r^2}\right)\cos\theta, \quad (r \ge r_2), \tag{4.3}$$

where $\Phi_1(r,\theta)$, $\Phi_2(r,\theta)$, and $\Phi_3(r,\theta)$ are the electric potentials in the dielectric core, metallic shell, and embedding medium, respectively. E_0 is the incident electric field (chosen along z-axis), r and θ are the spherical coordinates of the observation point. The unknown coefficients A_1, A_2, B_2, and B_3 are to be calculated from the continuity

conditions of the potential and the displacement vector at the interfaces of the dielectric core/metal and metal/embedding medium.

The local electric field E_1 induced in the dielectric core of the nanocomposite is related to the incident electric field, E_0, by the following equation [194]:

$$E_1 = A_1 E_0.$$

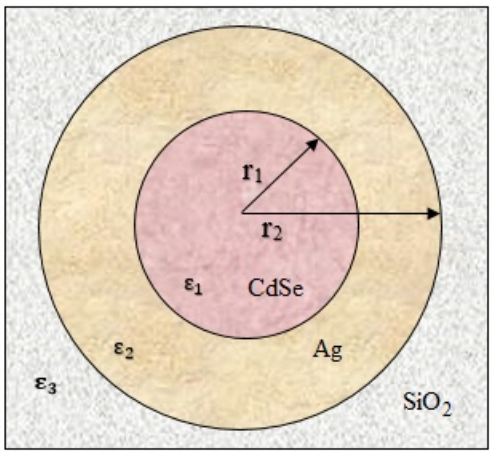

Figure 4.1: Schematics of core and single shell spherical nanoparticle embedded in host matrix.

In this equation ($E_1 = A_1 E_0$), the coefficient A_1 can be shown to be given by

$$A_1 = \frac{Q\varepsilon_2\varepsilon_3}{p\Delta} = F, \tag{4.4}$$

where $Q = n^2/(n-1)$ and $p = 1-(r_1/r_2)^3$ is the volume fraction of the metal coated particle. Also, n represents the dimension of the problem, which for a spherical nanoinclusion is 3. In Eqn. (4.4), Δ is given by

$$\Delta = \varepsilon_2^2 + q\varepsilon_2 + \varepsilon_1\varepsilon_3, \tag{4.5}$$

where

$$q = \left(\frac{3}{2p} - 1\right)\varepsilon_1 + \left(\frac{3}{p} - 1\right)\varepsilon_3.$$

In this study, we used silver metal as a shell material. From the Drude-Lorentz model, the electric permittivity of a metal from Eqn. (2.34) is given by

$$\varepsilon_2 = \varepsilon_\infty - \frac{\omega_p^2}{\omega(\omega + i\gamma)}, \tag{4.6}$$

where ε_∞ is the phenomenological parameter that represents the contribution of bound electrons to polarizability, ω_p is the bulk electron plasma frequency, and γ is a parameter associated with damping in the bulk material. Clearly, Eqn. (4.6) has real and imaginary parts which can be rewritten as

$$\varepsilon_2 = \varepsilon_2^{'} + i\varepsilon_2^{''}, \tag{4.7}$$

where

$$\varepsilon_2^{'} = \varepsilon_\infty - \frac{\omega_p^2}{\omega^2 + \gamma^2}, \qquad \varepsilon_2^{''} = \frac{\omega_p^2 \gamma}{\omega^2 + \gamma^2}.$$

Now, substituting eqns. (4.5) and (4.7) into Eqn. (4.4), we find that F becomes a complex function. Rather, it would be convenient to deal with the real quantity $|F|^2$, which is called the enhancement factor. It can be presented as [**?**]:

$$|F|^2 = \frac{81\varepsilon_3^2}{4p^2}\left(\frac{\varepsilon_2^{'2} + \varepsilon_2^{''2}}{(\varepsilon_2^{'2} - \varepsilon_2^{''2} + q\varepsilon_2^{'} + \varepsilon_1\varepsilon_3)^2 + \varepsilon_2^{''2}(q + 2\varepsilon_2^{'})^2}\right). \tag{4.8}$$

Alternatively, an equivalent expression to Eqn. (4.8) can be obtained from the relation $E = -\nabla\Phi$ using Eqn. (3.8) for E_1 and then taking the square of the ratio of E_1 to E_0.

4.2.2 Triple layer spherical nanoparticles

Here, let's first consider a concentric n-layer nanocomposite that consists of multiple nanoscale layers of controllable thickness. The electrostatic potential for each of the regions (layers) satisfy the Laplace's equation which is given by $\nabla^2\Phi_i = 0$, where Φ_i is the electric potential associated with the electric field induced inside and outside the nanocomposite, i is the region where electric potential is to be determined. Let, the

dielectric function of the i^{th} region can be represented by ε_i.

The potential distribution in the different regions of the n-layered nanocomposite is obtained by solving the Laplace's equation. Accordingly, the potential Φ_i in each region is given by [195]:

$$\Phi_i(r,\theta) = \left(A_i r + \frac{B_i}{r^2}\right)\cos\theta, \tag{4.9}$$

where A_i and B_i are the coefficients correspond to the electric monopole and dipole terms, respectively. These coefficients, A_i and B_i are to be determined by employing the appropriate boundary conditions for the continuities of the tangential and normal components of the electric field and the displacement vector, respectively [196]. In our case, the spherical coordinates (r,θ) are used, where r is the radial distance and θ is the polar angle, while the direction of the applied field E_0 is chosen along the z-axis. Then, the electric field E_i in the i^{th} region for the concentric spherical n-layered nanocomposite is obtained using the equation $\overrightarrow{E}_i = -\nabla\Phi_i(r,\theta)$, where $\Phi_i(r,\theta)$ is given by Eqn. (4.9) [197]. Hence, the field takes the following form:

$$\overrightarrow{E_i} = A_i(-\cos\theta\hat{e}_r + \sin\theta\hat{e}_\theta) + B_i r^{-3}(2\cos\theta\hat{e}_r + \sin\theta\hat{e}_\theta), \tag{4.10}$$

where $i = 1,2,...,n$ with n being the number of layers and $\hat{e}_r$ and $\hat{e}_\theta$ are the unit vectors in the r and θ directions, respectively.

Next, we consider a triple layered ($n = 3$) core-shell nanostructure in which region one with $i = 1$ is a semiconductor core (CdSe) of dielectric function ε_1, while the outer region is the embedding medium (SiO_2) with real dielectric constant $\varepsilon_{n+1} = \varepsilon_4$. The dielectric functions of the spacer (ZnSe) and the metallic shell (Ag) are ε_2 and ε_3, respectively. Similarly, the radii of the dielectric core, the spacer, and the metallic shell are denoted by r_1, r_2, and r_3, respectively.

For triple layered nanocomposite, there are four regions [198]. Thus, by extending Eqn. (4.10) to spherical nanocomposite, the expressions for the electric fields in each

region are as follows:

$$\overrightarrow{E_1} = A_1(-\cos\theta\hat{e}_r + \sin\theta\hat{e}_\theta) + B_1 r^{-3}(2\cos\theta\hat{e}_r + \sin\theta\hat{e}_\theta), \tag{4.11}$$

$$\overrightarrow{E_2} = A_2(-\cos\theta\hat{e}_r + \sin\theta\hat{e}_\theta) + B_2 r^{-3}(2\cos\theta\hat{e}_r + \sin\theta\hat{e}_\theta), \tag{4.12}$$

$$\overrightarrow{E_3} = A_3(-\cos\theta\hat{e}_r + \sin\theta\hat{e}_\theta) + B_3 r^{-3}(2\cos\theta\hat{e}_r + \sin\theta\hat{e}_\theta), \tag{4.13}$$

$$\overrightarrow{E_4} = A_4(-\cos\theta\hat{e}_r + \sin\theta\hat{e}_\theta) + B_4 r^{-3}(2\cos\theta\hat{e}_r + \sin\theta\hat{e}_\theta), \tag{4.14}$$

where $A_4 = -E_0$ and A_1, A_2, A_3, B_2, B_3 and B_4 are unknowns to be determined by imposing the appropriate boundary conditions. In particular, the coefficient $B_1 = 0$, since the magnitude of the electric field in the dielectric core is constant.

To investigate the LFEF inside the concentric sphere, it is suffice to determine the electric field induced inside the dielectric core. This means that (since $B_1 = 0$), we only need to determine the coefficient A_1 found in Eqn. (4.11). Hence, employing the relevant boundary conditions at the interfaces, this coefficient can be shown to have the following form

$$A_1 = -\frac{27}{2}\frac{\varepsilon_2\varepsilon_3\varepsilon_4}{f_2 M}E_0 = F, \tag{4.15}$$

where

$$M = y_1{\varepsilon_3}^2 + y_2\varepsilon_3 + y_3,$$

$$f_2 = 1 - \left(\frac{r_2}{r_3}\right)^3,$$

$$y_1 = f_1(\varepsilon_1 - \varepsilon_2) + 3\varepsilon_3,$$

$$y_2 = \left(\frac{3}{f_2} - 1\right)\left[3\left(\frac{\varepsilon_1}{2} + \frac{2\varepsilon_4}{3}\right)\varepsilon_2 + f_1(\varepsilon_1 - \varepsilon_2)(\varepsilon_4 - \varepsilon_2)\right] + \varepsilon_2(f_1(\varepsilon_1 - \varepsilon_2) - \varepsilon_4 - \frac{3}{2}\varepsilon_2),$$

$$y_3 = \varepsilon_2\varepsilon_4(3\varepsilon_1 + 2f_1(\varepsilon_2 - \varepsilon_1)),$$

where

$$f_1 = 1 - \left(\frac{r_1}{r_2}\right)^3.$$

Substituting Eqn. (4.15) into Eqn. (4.11), the magnitude of induced field inside the

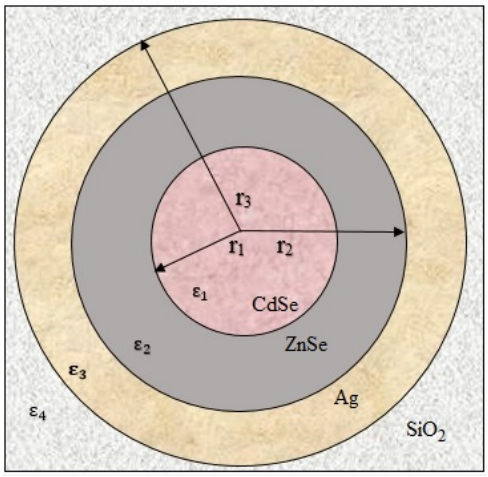

Figure 4.2: Triple layer spherical nanostructure embedded in host matrix.

dielectric core is found to be

$$E_1 = E = \frac{27}{2}\frac{\varepsilon_2\varepsilon_3\varepsilon_4}{f_2 M}E_0. \tag{4.16}$$

The coefficient of E_0 in Eqn. (4.15) is the local field enhancement factor (F). That is,

$$F = \frac{E}{E_o} = \frac{27}{2}\frac{\varepsilon_2\varepsilon_3\varepsilon_4}{f_2 M}, \tag{4.17}$$

and the modulus square of the LFEF becomes:

$$|F|^2 = \left|\frac{27}{2}\frac{\varepsilon_2\varepsilon_3\varepsilon_4}{f_2 M}\right|^2. \tag{4.18}$$

The optical properties of metals can be described by the Drude-Sommerfeld model of the frequency-dependent dielectric function, $\varepsilon(\omega)$ [199]. In our case (i.e., Eqn. (4.18)), ε_3 represents the dielectric permittivty of the silver metal and can be written as (Eqn. (2.34))

$$\varepsilon_3 = \varepsilon_\infty - \frac{\omega_p^2}{\omega(\omega + i\gamma)}. \tag{4.19}$$

For silver, $\omega_p = 1.37 \times 10^{16} Hz, \varepsilon_\infty = 9.01\ eV$, and $\omega = 2\pi c/\lambda$ is the angular frequency of applied electromagnetic field, c is the speed of electromagnetic wave [200] and γ

is a parameter associated with damping [201]. If the mean free path of electron in the nanostructre depends on size of the nanocomposites, then its damping parameter differs from its bulk counterpart, and hence, γ in Eqn. (4.19) can be by given Eqn. (2.35) as

$$\gamma = \gamma_0 + A\frac{v_F}{r_{eff}}, \tag{4.20}$$

where γ_0 is the damping constant of the bulk material (for Ag: $\gamma_0 = 3.23 \times 10^{13}\ Hz$), v_F is the velocity of an electron at the Fermi surface ($v_F = 1.4 \times 10^6\ m/s$ for silver), A is an empirical parameter, usually set to be unity, r_{eff} is the effective mean free path of electrons and is calculated using Eqn. (2.36) as:

$$r_{eff} = \frac{1}{2}[(r_3 - r_2)(r_3^2 - r_2^2)]^{\frac{1}{3}}. \tag{4.21}$$

4.3 Results and discussions

4.3.1 Core and single shell nanoparticles

In this section, we investigated the local field enhancement factor for the core and single shell CdSe@Ag nanoparticles. Figures 4.3 and 4.4 depict the graphs of the enhancement factor for different core, shell, and nanoparticle (NP) sizes as a function of wavelength plotted using Eqn. (4.8).

From figure 4.3(a), it is observed that as the size (r_1) of the core (CdSe) of the nanocomposite is reduced from 10 *nm* to 2 *nm* for a fixed radius ($r_2 = 20$ *nm*) of the silver (Ag) metal, the peaks of the resonances are increased by 18.2 folds (increased from about $1,743$ at 452 *nm* to $31,760$ at 478 *nm*) at the interface between CdSe@Ag. This is observed when the core radius is relatively the smallest (2 *nm*) and the metal shell thickness is the largest (18 *nm*), where 18 *nm* is the difference of the two radii (20 *nm* $-$ 2 *nm* $=$ 18 *nm*). From this, one can see that when the core radius decreases and the shell thickness increases simultaneously at constant shell radius (20 *nm*), the local field is enhanced and the surface plasmon peaks shift to the higher energy. This result agrees with other research findings that when the core size is made smaller, the

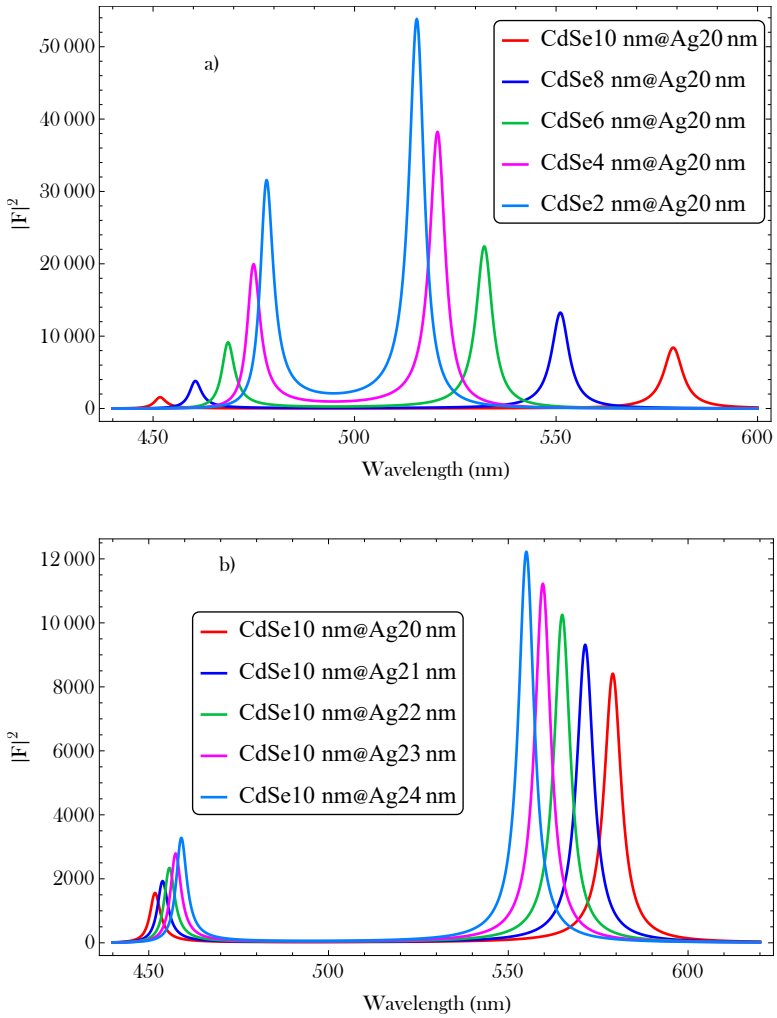

Figure 4.3: LFEF of CdSe@Ag: (a) when the size of the NP is fixed at 20 *nm* as the size of the core decreases and (b) when the size of the core is fixed at 10 *nm* as the shell thickness increases.

resonance peaks are enhanced [202, 203]. This may be explained with the fact that as the shell thickness increases, the hybridization between the two plasmon frequencies of the inner and outer surfaces decrease, leading to the blue shift.

Moreover, the metal content of the particle increases with decrease in the core radius so that there are more electrons to participate in the oscillation. As a result, the coupling of localized surface plasmon resonance becomes stronger and leads to local field enhancement. Our findings are in good agreement with the previous findings [204–206]. For the same core-shell nanoparticle parameters, the field enhancement factor has increased by about 6.3 times (nearly increased from $8,558$ at 579 *nm* to $53,960$ at

514 *nm*) at the interface between the shell (Ag) and the host matrix (SiO_2). From figure 4.3(a), it is observed that the resonance peaks shift towards the longer wavelength (red shift) of the visible region of electromagnetic spectrum at the inner interface of CdSe@Ag, and towards the shorter wavelength at its outer interface. Taking the ratio of the magnitudes of the resonance peaks of the outer interface to the inner interface of CdSe@Ag, the local electric field is enhanced by about 1.7 factor (from $53,960$ to $31,760$). Moreover, the result also reveal that the local field enhancement factor of the CdSe@Ag has been increased with the decrease in the core size.

Furthermore, figure 4.3(b) shows that keeping the core size constant ($r_1 = 10$ *nm*) and increasing the NP size from 20 *nm* to 24 *nm* enhanced the LFEF from about $8,434$ to $12,270$. This enhancement is accompanied with a blue shift of the enhancement peaks from 579 *nm* to 555 *nm* in the outer interface of silver ($Ag@SiO_2$). Note that comparison of figures 4.3(a) and 4.3(b) shows that the LFEF is higher when the size of the core is reduced than when the thickness of the shell is increased. This might indicate that the quantum confinement is more significant than the plasmonic effect for the local field enhancement.

However, when both the core and the shell radii increase simultaneously ($r_1 = 5$ *nm* to 9 *nm* and $r_2 = 12$ *nm* to 16 *nm*), the resonance peaks are significantly lowered from about $12,270$ at 555 *nm* to $6,550$ at about 603 *nm* at the interface of $Ag@SiO_2$ (Fig. 4.4(a)). Also, when the sizes of both the core and the shell changes simultaneously by equal amounts (*i.e.*, $\Delta r = 4$ *nm*), the amplitudes of the resonance peaks are reduced from $3,316$ at 460 *nm* to about 918 at 446 *nm* at the interface of CdSe@Ag region.

For the nanoparticle considered under this section, the simultaneous increase in the radii of the core and the shell could not help to increase the local enhancement factor for the core-shell nanoparticle. This can be attributed to the fact that, when the shell size increases, charge separation distance also increases, leading to the decrease in the electric field inside the nanoparticle. In the other case, when the radius of the core is increased from 3 *nm* to 7 *nm*, while reducing the size of the shell from 17 *nm* to 13 *nm*, the local field enhancement factor is reduced from $42,660$ to $7,237$ (Fig. 4.4(b)).

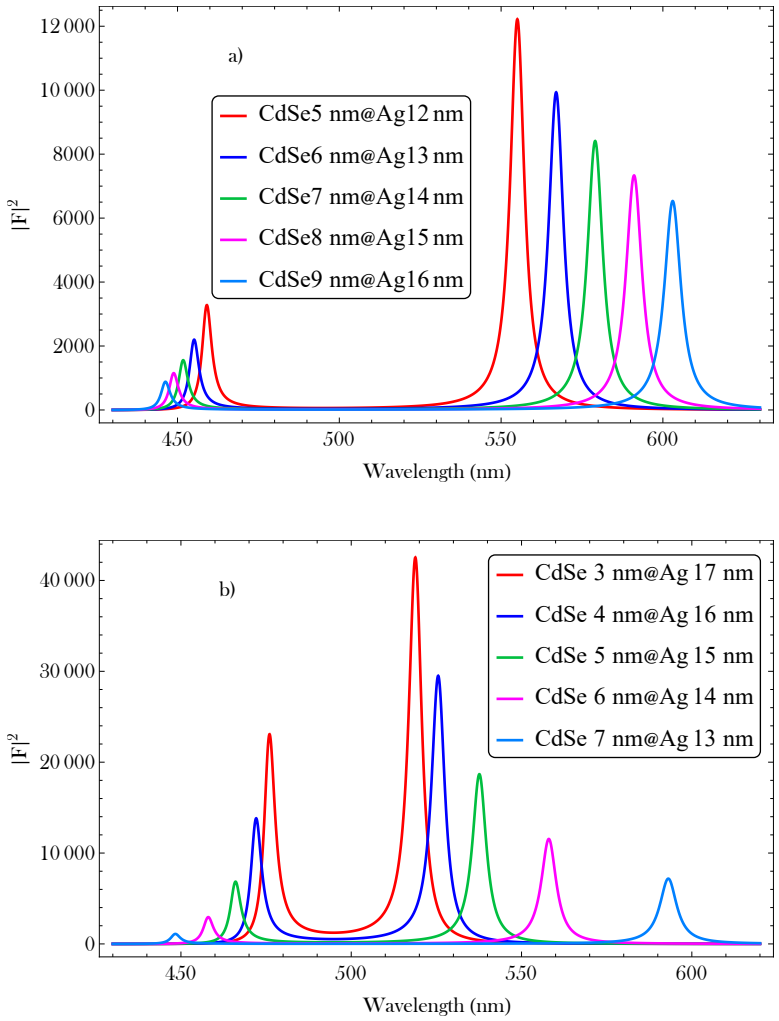

Figure 4.4: LFEF of CdSe@Ag Nanoparticle: (a) when core and the NP sizes are both increasing and (b) when core size is increasing and the shell thickness is decreasing.

Whether the shell size is constant or decreased, increasing the core size led to lower field enhancement factor for the material under the study. Hence, it is observed that the core size of the nanoparticle is a crucial parameter to increase or decrease the field enhancement factor for the core and single shell CdSe@Ag spherical nanoparticle. All these results show that the local field enhancement factor of CdSe@Ag nanoparticle becomes controllable by carefully altering the size of the core radius.

4.3.2 Triple layered core@shell nanoparticles

In the second part of this study, ZnSe was placed as a spacer between the CdSe core and Ag shell and the local electric field enhancement was analyzed using Eqn. (4.18). The size of ZnSe ($r_2 = 10$ *nm*) is fixed and the sizes of the core (r_1) and the NP (r_3) were varied (Fig. 4.5(a)). As the core and the NP sizes increase ($r_1 = 5$ *nm* to 9 *nm*; $r_3 = 12$ *nm* to 16 *nm*), two sets of resonance peaks were observed. The two resonances are associated with the inner and outer interfaces of silver shell, respectively.

In the absence of the ZnSe spacer, the intensities of the local field enhancements decrease with increase in the core and the NP sizes (*i.e.*, Fig. 4.4(a)). However, when the spacer was placed in between CdSe and Ag, the magnitudes of the resonance peaks showed increasing effect for the same increase in the core size and for the same size of the whole NP (Fig. 4.5(a)). This result reveals that the spacer has an increasing effect on the LFEF of core-shell nanoparticle even when the core size is increasing. Previous researches show that the thickness of the dielectric spacer controls the plasmonic response of the three layered nanoparticles [41, 207]. Thus, one of the reasons for the increase in the local field enhancement in this study might be due to the decrease in the thickness of the spacer layer (ZnSe). As illustrated in figure 4.5(a), when the core radius and the shell thickness are increasing, the spacer layer is decreasing from 5 *nm* to 1 *nm*. That is, the decrease in the thickness of the spacer layer provides a platform for strong plasmonic coupling between the core and the outer metal shell nanomaterial leading to the enhancement of the local field. For all the dimensions indicated in figure 4.5(a), the second set of the resonance peaks show a blue shift within the visible range of electromagnetic spectrum.

In figure 4.5(b), the core and the NP sizes were fixed and the size of ZnSe was varied from $r_2 = 10$ *nm* to 10.8 *nm*. In this process, still two peaks were observed but the resonance peaks were found to decrease with an increase in the size of the spacer. Among all the size combinations, comparatively the largest peak is obtained when the spacer size is the thinnest. Previous experimental studies show that when thin layer of ZnSe is

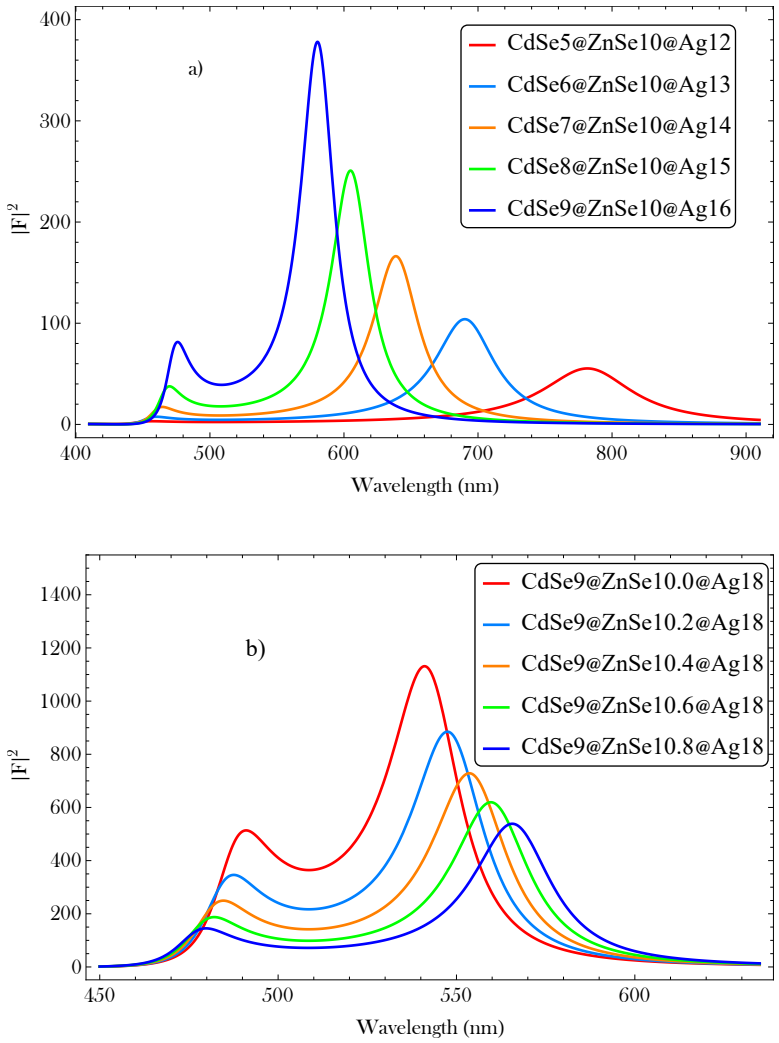

Figure 4.5: LFEF of CdSe@ZnSe@Ag: (a) when core and the shell sizes are increasing and spacer thickness is decreasing and (b) when spacer size is increasing at fixed core and shell sizes.

deposited on CdSe, its emission efficiency increases [181]. When it becomes thicker, the defects on the ZnSe surface may induce the nonradiative transitions, thereby decreasing the emission intensity [187]. Our theoretical and numerical analysis also show similar results that when relatively the thinnest ZnSe is used as spacer on the CdSe core, the LFEF increases. However, when the spacer thickness increases, the peaks of the resonances decreases and are red shifted (Fig. 4.5(b)). Comparison of Figs. 4.5(a) and 4.5(b) shows that the core and the spacer sizes have different effects on the field enhancement factor of core@shell spherical NPs. In figure 4.6(a), the radii of the core

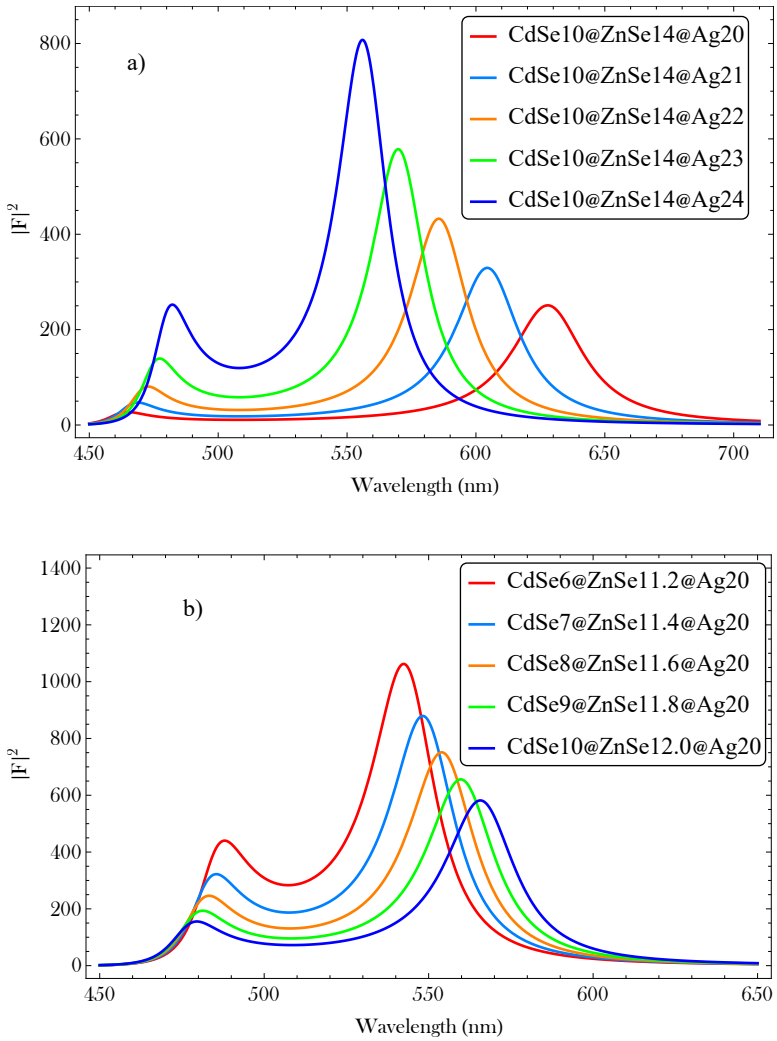

Figure 4.6: LFEF of CdSe@ZnSe@Ag: (a) when shell size is increasing at fixed sizes of the core and spacer and (b) when core size is increasing and spacer thickness is decreasing at fixed NP size.

($r_1 = 10\ nm$) and the spacer ($r_2 = 14\ nm$) are fixed and the shell size was increased from $r_3 = 20\ nm$ to $24\ nm$. The result shows that the field enhancement factor increases with an increase in the metallic shell size which might be related to the surface plasmon resonance [197, 199]. This is similar to Fig. 4.3(b) in all aspects except the presence of the spacer (ZnSe). For the two layer NP (Fig. 4.3(b)), the resonance peaks are higher and are achieved at shorter wavelengths whereas in the triple layer case (Fig. 4.6(a)), the peaks are lower and are located at relatively longer wavelengths. When the core size increases and the spacer thickness decreases with constant NP (core + shell)

size ($r_2 = 20\ nm$), the field enhancement factor decreases (Fig. 4.6(b)). In this process, the resonance peaks in the outer interface of the metal shell were red shifted. Although the amplitudes were not the same, the peak positions of results in figure 4.6(a) were nearly reversed in figure 4.6(b).

In figure 4.7(a), the core and the spacer sizes are constant and the metal shell size is increasing. This results in increased field enhancement factor.

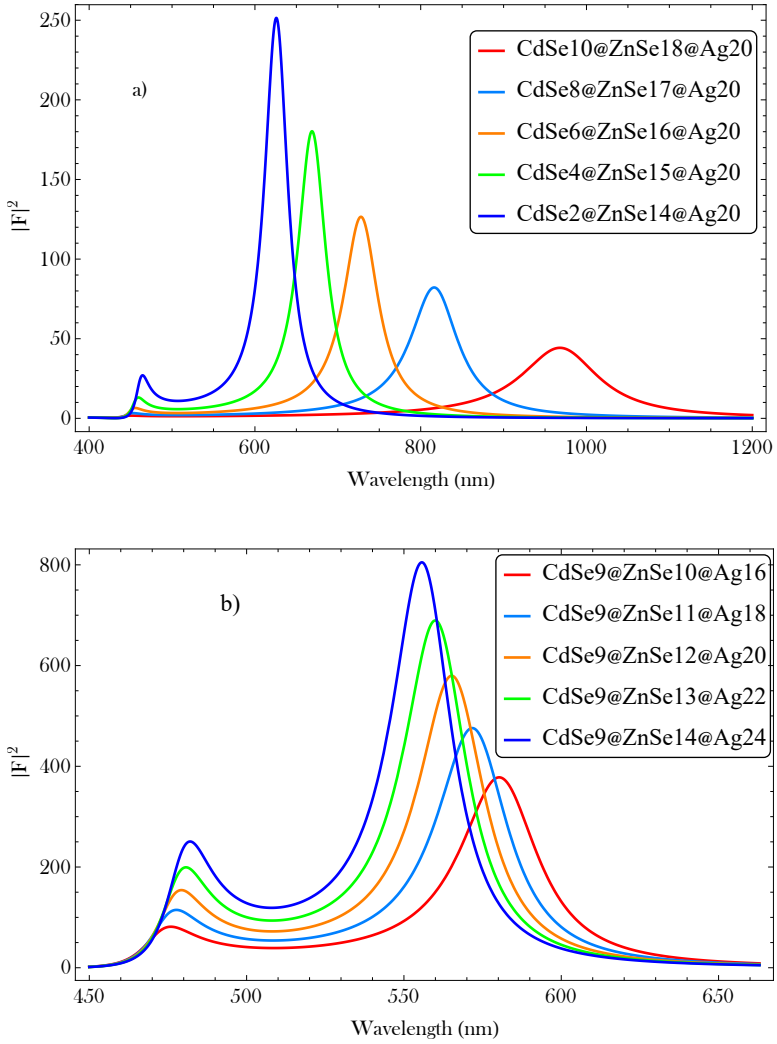

Figure 4.7: LFEF of CdSe@ZnSe@Ag: (a) when core size is decreasing and spacer thickness is increasing at fixed size of NP and (b) when spacer and shell thicknesses are increasing at fixed core size.

In the two layer NP, a blue shifted and significantly enhanced local field can be obtained in the visible range of the spectrum by decreasing the core size (Fig. 4.3(a)).

However, in the presence of spacer between the core and the metal shell of the same NP size, relatively smaller field enhancement is observed with significant blue shift from infra-red (IR) to the visible spectral region (Fig. 4.7(a)). Keeping the core size fixed and simultaneously increasing the spacer and the metal shell thicknesses also show enhancement of the LFEF with the blue shift of the resonance peaks (Fig. 4.7(b)). Nevertheless, the magnitudes of the peaks were more pronounced in the latter case. Comparing the results of double and triple layered nanoparticles explored in this study, LFEF was enhanced with increasing the core size in the presence of spacer (ZnSe). But this was not observed in the core and single shell nanostructure. Increasing the metallic shell radius (keeping others constant) shows increased LFEF both in the double (Fig. 4.3(b)) and the triple (Fig. 4.6(a)) layered nanostructures except that the increment was larger for two layered NP than the triple layered NP by the factor of about 15.3 (i.e., 12,270 to 800). When the core and the NP sizes increase simultaneously for double layered NP (Fig. 4.4(a)), the LFEF decreases accompanied with red shift while the LFEF increases and are blue shifted for the triple layered one (Fig. 4.5(a)). This indicates that in triple layered core-shell spherical nanoaprticle, enhancement of the local field can be achieved at higher energy.

In addition to the effects of core, spacer, and shell sizes on the LFEF of CdSe@Ag spherical nanoparticles, we have also investigated how the LFEF is affected by the type of embedding medium (Fig. (4.8)). The result shows that when the magnitude

Table 4.1: Effects of host medium and shell thickness on the LFEF of spherical nanoshell.

permittivity of host medium			Metal shell thickness		
ε_h	λ (nm)	Peak 2	$\Delta r\ (nm)$	λ (nm)	Peak 2
2.5	579	8,433	10	579	8,379
3.5	614	10,970	11	571	8,797
4.5	649	12,400	12	565	10,260
5.5	682	13,110	13	560	11,230
6.5	715	13,380	14	555	12,230

of the dielectric function of the host medium increases, the intensity of the LFEF also increases, and red shifts. Comparing the result of figure 4.3(b) with that of figure 4.8

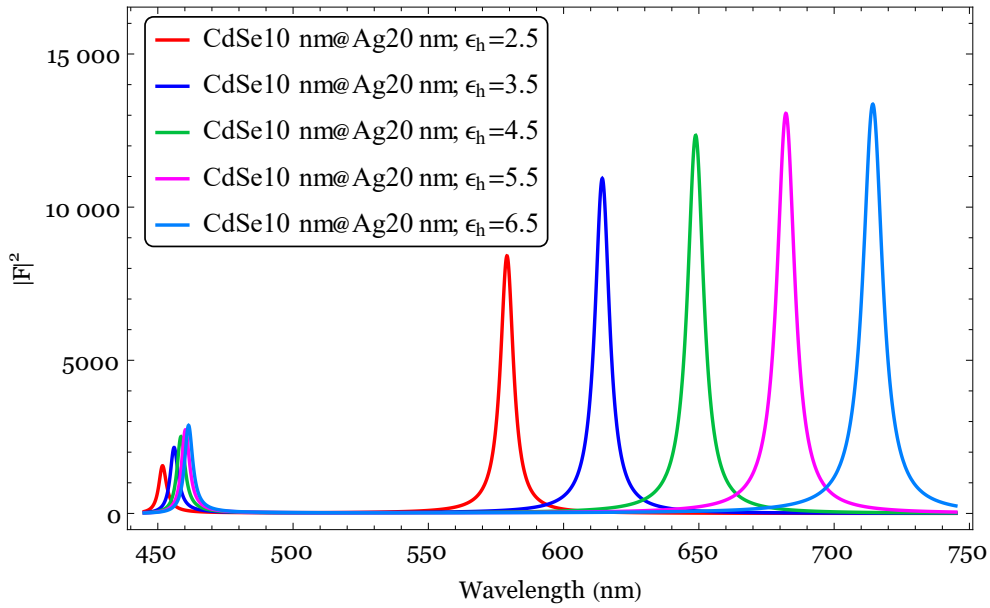

Figure 4.8: LFEF of CdSe@Ag in a varying host dielectric function.

as shown in Table 4.1, increasing the dielectric function of the embedding medium by a magnitude of 1 greatly enhances the LFEF of CdSe@Ag nanopartcles, than does increasing the metallic shell thickness by 1 *nm*.

Hence, it could be said that host matrix comparatively with larger magnitude of dielectric permittivity results in larger intensity in LFEF of dielectric core-metallic shell spherical nanoparticles. From this analysis, it might be worthy to mention that while designing spherical dielectric core-metallic shell nanoparticles for different purposes that require larger field enhancement, using dielectric medium of larger electric permittivity can save the consumption of large amounts of noble metals like Ag.

4.4 Conclusions

In this study, the local field enhancement factor of CdSe@Ag and CdSe@ZnSe@Ag core-shell nanoparticles were studied theoretically and numerically by changing the sizes of each components. For a fixed size of the NP, the local field enhancement fac-

tor of CdSe@Ag was increased with the decrease in the size of the core. Moreover, the resonance peaks were red shifted and blue shifted, respectively, in the inner and outer interfaces. By increasing the size of metallic shell while keeping the core size constant, similar patterns of resonance peaks were obtained except that the degree of enhancements were larger in the former case. Increasing the core size produces lower field enhancement factor whether the shell thickness is constant or decreased in size. This may indicate that the core size is a crucial parameter to change the field enhancement factor of the dielectric core and metallic shell nanoparticle. Alternatively, it is also possible to largely enhance the local field of nanoshells by keeping the core and shell sizes constant and increasing the dielectric function of the host matrix in which the nanoshell is embedded. While designing spherical nanoshells for various purposes that require larger local field enhancement, it seems advisable to use host matrix of larger electric permittivity than larger metallic shell thickness.

For triple layered spherical core-shell nanopartile, setting the ZnSe radius constant, the resonance peak increases with an increase in the size of the core which was not observed in the case of two layered core-shell nanocomposites having the same core and NP sizes. In triple layered core-shell spherical nanoparticle, an increase in the size of the spacer led to a decrease in the field enhancement factor of the nanocomposite. For fixed sizes of the core and the NP, the lower the size of the spacer produces the higher the field enhancement factor. On the other hand, increasing the thickness of the shell size increases the magnitude of the resonance peaks. Similarly, increasing the thicknesses of both the spacer and the shell sizes also increased the field enhancement factor. In conclusion, the sizes of the core, the spacer, and the shell have vigorous effects on the local field enhancement factor of core-shell nanoparticles. The possibility of obtaining size dependent LFEF by adjusting the sizes of nanoparticles make these nanocomposites attractive for applications in optoelectronics and nonlinear optics.

Chapter 5

Effects of Shape on the Optical Properties of CdSe-Au Core-Shell Nanocomposites

5.1 Introduction

Nowadays, the optical properties of nanoparticles are central to many applications in the areas of light-emitting diodes, photocatalysis, biochemical sensing, solar energy conversions, bio-sensors, degradation of harmful chemicals, and medical diagnostics [208–211]. In studying these nanoparticle structures, metallo-dielectric core-shell nanoparticles, composed of a dielectric core and a metal shell, have attracted a great amount of interest in plasmonics due to the wide tunability of the plasmon resonances [212]. As the plasmon resonances of core-shell nanoparticles are sensitive to their geometry [213], the optical properties of such nanocomposites (NCs) can be controlled and modified as desired [214]. As a result of this, core-shell NCs with different shapes are currently one of the leading active research fields [215]. Several researches have been conducted experimentally, computationally, and theoretically regarding the effect of shape on the optical properties of core-shell NCs such as SiO_2@Au [216], Si@SiO_2 [217], Ag@SiO_2 [218], Fe_2O_3@SiO_2 [219], Au-Ag@TiO_2 [220], CdSe@Al_2O_3@Ag

[221], CdSe@Ag [222], ZnO@Au [223], and so on.

Among many core-shell nanoparticles, the CdSe quantum dot have been studied intensively owing to the size-dependent photoemission [224]. It was reported that higher emission efficiency and desired emission wavelength can be obtained from CdSe based quantum dots [225, 226]. When noble metals such as silver and gold are used as a shell and coated over CdSe core, it was indicated that CdSe based core-shell nanoparticle showed high electromagnetic field enhancement [227].

However, many of these studies were investigated by varying the sizes of the quantum dot and not the shapes. Even where shapes were considered, many of the systems studied so far have been either spherical or cylindrical or spheroidal or at most two of the shapes at a time. To the best of our knowledge, the optical properties of CdSe@Au core-shell NCs has not been studied by changing their shapes alternately as spherical, cylindrical, oblate, and prolate spheroids. Thus, in the present study, we theoretically and numerically investigated the local field enhancement factor, absorption, and extinction cross-sections of spherical, cylindrical, oblate, and prolate shaped core-shell NCs each consisting cadmium selenide (CdSe) as a dielectric core and gold (Au) as a metallic shell with the whole system embedded in SiO_2 host medium.

5.2 Theoretical models and calculations

5.2.1 Spherical core@shell nanocomposites

Changing the shapes of core-shell NCs can help to control their optical properties that determines the effectiveness of the nanostructure. In this section, we considered a spherical core-shell nanocomposite shown in figure 5.1. The dielectric core (CdSe) has a radius r_1 with dielectric function ε_1. The metallic shell (Au) has a radius r_2 and frequency dependent dielectric function ε_2 with the whole nanocomposite embedded in a dielectric host matrix (SiO_2) of dielectric function ε_3.

When an electromagnetic wave with electric field intensity E_0 is incident on this core-shell nanoparticle along $z-$axis, the local electric field in the dielectric core under the

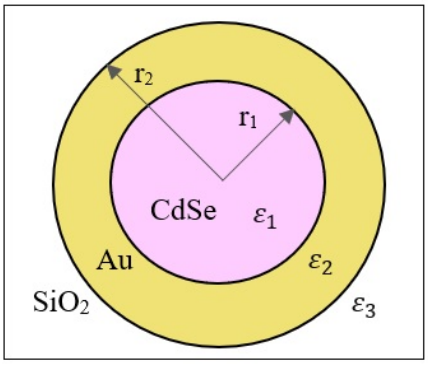

Figure 5.1: Schematic of spherical core-shell nanocomposite embedded in host matrix.

quasi-static approximation can be given using using Eqn. (3.8) as

$$E_1 = \frac{9\varepsilon_2\varepsilon_3}{(\varepsilon_1+2\varepsilon_2)(\varepsilon_2+2\varepsilon_3)+2f(\varepsilon_1-\varepsilon_2)(\varepsilon_2-\varepsilon_3)}E_0, \tag{5.1}$$

where $f = (r_1/r_2)^3$. For the sake of simplicity, let's represent the denominator in Eqn. (1) by:

$$2p\Delta, \tag{5.2}$$

where

$$\Delta = \varepsilon_2^2 + q\varepsilon_2 + \varepsilon_1\varepsilon_3, \quad q = \left(\frac{3}{2p}-1\right)\varepsilon_1 + \left(\frac{3}{p}-1\right)\varepsilon_3, \quad p = 1-f. \tag{5.3}$$

Hence, Eqn. (5.1) can be written as:

$$E_1 = \frac{9\varepsilon_2\varepsilon_3}{2p\Delta}E_0. \tag{5.4}$$

The coefficient of E_0 in Eqn. (5.4) is called local field enhancement factor (LFEF), A and can be given by:

$$A = \frac{E_1}{E_0} = \frac{9\varepsilon_2\varepsilon_3}{2p\Delta} = F. \tag{5.5}$$

In Eqn. (5.5), ε_2 is a complex frequency dependent electric permittivity of the metal shell and it can be written as:

$$\varepsilon_2 = \varepsilon_2^{'} + i\varepsilon_2^{''}, \tag{5.6}$$

where $\varepsilon_2^{'}$ and $\varepsilon_2^{''}$ are the real and imaginary parts, respectively. Now, substituting Eqns. (5.3) and (5.6) in to Eqn. (5.5) and taking its modulus square, the LFEF in the dielectric core, as shown in Eqn. (4.8) is given by

$$|F|^2 = \frac{81\varepsilon_3^2}{4p^2}\left(\frac{\varepsilon_2^{'2}+\varepsilon_2^{''2}}{(\varepsilon_2^{'2}-\varepsilon_2^{''2}+q\varepsilon_2^{'}+\varepsilon_1\varepsilon_3)^2+\varepsilon_2^{''2}(q+2\varepsilon_2^{'})^2}\right). \tag{5.7}$$

When electromagnetic radiation interacts with matter (in our case, spherical core-shell nanocomposite), the scattering and absorption phenomenon arises, which are in turn determined by electrostatic polarizability, α. For the core-shell nanosphere geometry, the polarizability is given by Eqn. (2.65) as

$$\alpha = 4\pi r_2^3\left[\frac{(\varepsilon_2-\varepsilon_3)(\varepsilon_1+2\varepsilon_2)+f(\varepsilon_1-\varepsilon_2)(\varepsilon_3+2\varepsilon_2)}{(\varepsilon_2+2\varepsilon_3)(\varepsilon_1+2\varepsilon_2)+2f(\varepsilon_1-\varepsilon_2)(\varepsilon_2-\varepsilon_3)}\right]. \tag{5.8}$$

From this, the absorption and scattering cross-sections can be given by Eqns. (2.72) and (2.73) as

$$C_{abs} = kIm\left[\alpha\right], \quad C_{scat} = \frac{k^4}{6\pi}\left|\alpha\right|^2, \tag{5.9}$$

where $k = \frac{2\pi}{\lambda}\sqrt{\varepsilon_3}$ is the wavevector in the medium.

5.2.2 Cylindrical core@shell nanocomposites

Recently, investigating the optical properties of coated NCs associated with their shapes has been given significant attention [228]. Based upon this ample interest, let us consider coated cylindrical core-shell nanoparticle embedded in host medium as shown in figure 5.2. In this scheme, we assumed the cylinder is infinitely extended along the $z-$axis.

Based on the quasistatic approximation and by solving the Laplace's equation, the electric field in the core, the shell, and the host medium can be obtained as follows [229]:

$$\overrightarrow{E_1} = \left(1-\frac{A_1}{E_0}\right)\overrightarrow{E_0}, \tag{5.10}$$

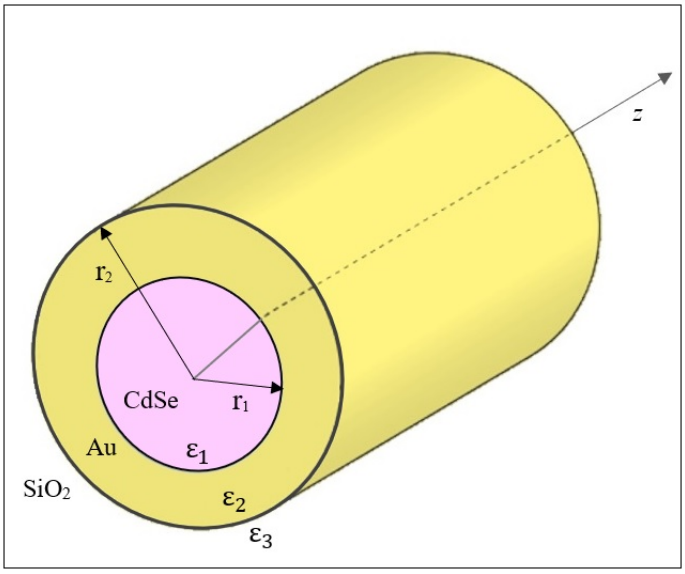

Figure 5.2: Schematic of cylindrical core-shell nanocomposite embedded in host matrix.

$$\overrightarrow{E_2} = \left(1 - \frac{A_2}{E_0}\right)\overrightarrow{E_0} + \frac{B_2}{r^2}(\cos\varphi\hat{e}_r + \sin\varphi\hat{e}_\varphi), \tag{5.11}$$

$$\overrightarrow{E_3} = \overrightarrow{E_0} + \frac{B_3}{r^2}(\cos\varphi\hat{e}_r + \sin\varphi\hat{e}_\varphi), \tag{5.12}$$

where r denotes the position vector of the observation point, φ is the included angle incident field makes with the position vector r. $\hat{e}_r$ and $\hat{e}_\varphi$ are unit vectors in the r and φ directions, respectively.

The coefficients A_1, A_2, B_2, and B_3 can be given by [230]:

$$A_1 = \frac{\varepsilon_2(\varepsilon_2 - 3\varepsilon_3) + \varepsilon_1(\varepsilon_2 + \varepsilon_3) + f[(\varepsilon_1 - \varepsilon_2)(\varepsilon_2 - \varepsilon_3)]}{(\varepsilon_1 + \varepsilon_2)(\varepsilon_2 + \varepsilon_3) + f(\varepsilon_1 - \varepsilon_2)(\varepsilon_2 - \varepsilon_3)}E_0, \tag{5.13}$$

$$A_2 = -\frac{(\varepsilon_2 - \varepsilon_3)[(\varepsilon_2 - \varepsilon_1)f - (\varepsilon_2 + \varepsilon_3)]}{(\varepsilon_1 + \varepsilon_2)(\varepsilon_2 + \varepsilon_3) + f(\varepsilon_1 - \varepsilon_2)(\varepsilon_2 - \varepsilon_3)}E_0, \tag{5.14}$$

$$B_2 = \frac{2\varepsilon_3(\varepsilon_1 - \varepsilon_2)r_1^2}{(\varepsilon_1 + \varepsilon_2)(\varepsilon_2 + \varepsilon_3) + f(\varepsilon_1 - \varepsilon_2)(\varepsilon_2 - \varepsilon_3)}E_0, \tag{5.15}$$

$$B_3 = \frac{(\varepsilon_1 - \varepsilon_2)(\varepsilon_2 + \varepsilon_3)r_1^2 + (\varepsilon_1 + \varepsilon_2)(\varepsilon_2 - \varepsilon_3)r_2^2}{(\varepsilon_1 + \varepsilon_2)(\varepsilon_2 + \varepsilon_3) + f(\varepsilon_1 - \varepsilon_2)(\varepsilon_2 - \varepsilon_3)}E_0, \tag{5.16}$$

where $f = (r_1/r_2)^2$. By substituting these coefficients A_1, A_2, B_2, and B_3 in to Eqns. (5.10) to (5.12), electric field in the core, the shell, and the surrounding medium can be calculated. If we insert the expression of A_1 in to Eqn. (5.10) and simplify it, local field enhancement in the dielectric core of the composite becomes:

$$E_1 = \frac{4\varepsilon_2\varepsilon_3}{(\varepsilon_1-\varepsilon_2)(\varepsilon_2-\varepsilon_3)+f(\varepsilon_1+\varepsilon_2)(\varepsilon_2+\varepsilon_3)}E_0. \tag{5.17}$$

If we let the denominator of Eqn. (5.17) by $p\Delta$, where $p = 1-f$, $\Delta = \varepsilon_2^2 + q\varepsilon_2 + \varepsilon_1\varepsilon_3$,
$q = (2/p-1)\varepsilon_1 + (2/p-1)\varepsilon_3$, we can represent the local field of the dielectric core of the inclusion in a simple expression as follows:

$$E_1 = \frac{4\varepsilon_2\varepsilon_3}{p\Delta}E_0. \tag{5.18}$$

From this, the enhancement factor (F) in the dielectric core can be obtained as

$$F = \frac{E_1}{E_0} = \frac{4\varepsilon_2\varepsilon_3}{p\Delta}. \tag{5.19}$$

Considering the modulus squared of the enhancement factor, we get:

$$|F|^2 = \left|\frac{E_1}{E_0}\right|^2 = \frac{16\varepsilon_2^2\varepsilon_3^2}{p^2\Delta^2}. \tag{5.20}$$

In Eqn. (5.20), ε_2 (of gold) is a complex function with real ($\varepsilon_2^{'}$) and imaginary ($\varepsilon_2^{''}$) parts, as given by Eqn. (5.6). Using the Drude-Lorentz model, this dielectric function can be given by Eqn. (2.15) as:

$$\varepsilon_2^{'} = \varepsilon_\infty - \frac{\omega_p^2}{\omega^2+\gamma^2}, \qquad \varepsilon_2^{''} = \frac{\omega_p^2\gamma}{\omega^2+\gamma^2}, \tag{5.21}$$

where ε_∞, ω, ω_p, and γ are the contribution of bound electrons to polarizabiliy, frequency of incident electromagnetic wave, the bulk plasma frequency of the silver metal, and the collision frequency of free electrons, respectively.

Decreasing the size of the nanoparticle will eventually cause the thickness to become less than the bulk mean free path, and electron scattering from the surfaces of the particle will have the effect of decreasing and broadening its plasmon resonance peak(s).

In Chapter 5 of this study, we used $v_F = 1.4 \times 10^6\ m/s$, $\gamma_0 = 4.6 \times 10^{13}\ Hz$, $\omega_p = 1.37 \times 10^{16}\ Hz$, and $\varepsilon_\infty = 9.84$ for gold metal [231] into Eqns. (2.35) (2.36). By substituting the complex dielectric function of the gold metal ε_2 with its real ($\varepsilon_2^{'}$) and imaginary ($\varepsilon_2^{''}$) parts in to Eqn. (5.20), the enhancement factor of the local field for coated cylindrical nanocomposite in the dielectric core can be given by:

$$|F|^2 = \frac{16\varepsilon_3^2}{p^2}\left(\frac{\varepsilon_2^{'2}+\varepsilon_2^{''2}}{(\varepsilon_2^{'2}-\varepsilon_2^{''2}+q\varepsilon_2^{'}+\varepsilon_1\varepsilon_3)^2+\varepsilon_2^{''2}(q+2\varepsilon_2^{'})^2}\right). \tag{5.22}$$

In investigating the optical resonances of nanoshells, it is important to consider its polarizability. Thus, the polarizability of cylindrical concentric nanoshells is defined as follows [232].

$$\alpha = 4\pi\frac{(\varepsilon_1-\varepsilon_2)(\varepsilon_2+\varepsilon_3)f+(\varepsilon_1+\varepsilon_2)+(\varepsilon_2-\varepsilon_3)}{(\varepsilon_1-\varepsilon_2)(\varepsilon_2-\varepsilon_3)f+(\varepsilon_1+\varepsilon_2)(\varepsilon_2+\varepsilon_3)}. \tag{5.23}$$

From the optical absorption and scattering theories, the absorption and scattering cross sections for a single shell nanoparticle [197] can be written as in Eqn. (5.9).

5.2.3 Ellipsoidal core@shell nanocomposites

Let's consider a core-shell ellipsoid shown in figure 5.3 with principal semiaxes a_1, b_1, and c_1 for the core surface and a_2, b_2, and c_2 for the outer shell surface. Using the ellipsoidal coordinates (ξ,η,ζ) and using the Eqn. (3.11), the confocal ellipsoidal surfaces can be expressed by

$$\frac{x^2}{{a_1}^2+\xi}+\frac{y^2}{{b_1}^2+\xi}+\frac{z^2}{{c_1}^2+\xi}=1, \quad -c_1^2<\xi<\infty, \tag{5.24}$$

$$\frac{x^2}{{a_1}^2+\eta}+\frac{y^2}{{b_1}^2+\eta}+\frac{z^2}{{c_1}^2+\eta}=1, \quad -b_1^2<\eta<-c_1^2, \tag{5.25}$$

$$\frac{x^2}{{a_1}^2+\zeta}+\frac{y^2}{{b_1}^2+\zeta}+\frac{z^2}{{c_1}^2+\zeta}=1, \quad -a_1^2<\zeta<-b_1^2. \tag{5.26}$$

The coordinate ξ is normal to the surface. The variables η and ζ are the parameters of confocal hyperboloids and as such serve to measure the position on any ellipsoid $\xi =$ constant. In other words, each ellipsoidal surface is defined by a constant ξ. Therefore,

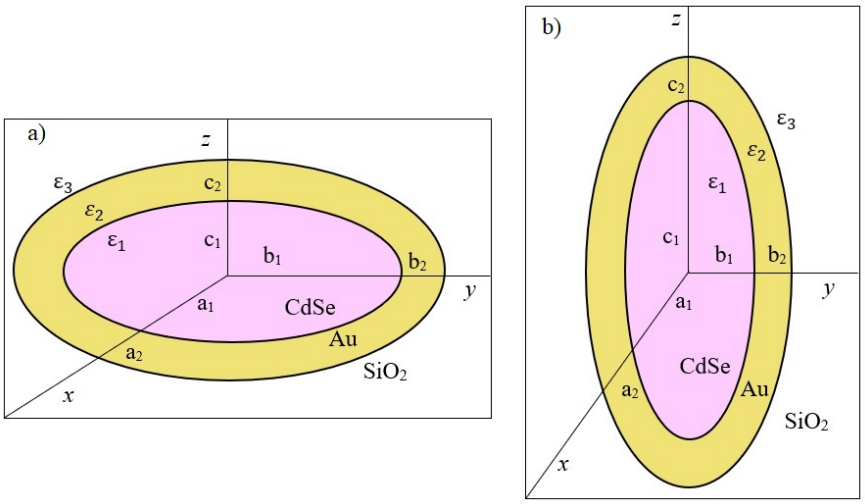

Figure 5.3: Schematic representation of: a) oblate and b) prolate spheroidal core-shell NCs.

$\xi = 0$ is the equation of the surface of inner ellipsoid and $\xi = t$ is that of the surface of the outer ellipsoid, where $a_1^2+t=a_2^2, \quad b_1^2+t=b_2^2, \quad c_1^2+t=c_2^2$.

For a given (x,y,z), if we assume $x>0, y>0, z>0$, there is a one to one correspondence between (x,y,z) and the three largest roots (ξ,η,ζ) . Solving for x, y, and z as in Eqn. (3.15), we obtain the following expressions:

$$x^2=\frac{(a_1^2+\xi)(a_1^2+\eta)(a_1^2+\zeta)}{(b_1^2-a_1^2)(c_1^2-a_1^2)},$$

$$y^2=\frac{(b_1^2+\xi)(b_1^2+\eta)(b_1^2+\zeta)}{(a_1^2-b_1^2)(c_1^2-b_1^2)},$$

$$z^2 = \frac{(c_1^2+\xi)(c_1^2+\eta)(c_1^2+\zeta)}{(a_1^2-c_1^2)(b_1^2-c_1^2)}.$$

The potential due to the applied field, which we take to be parallel to the z axis, is

$$\varphi_0 = -E_0 z = -E_0 F_1(\xi) G(\eta,\zeta)$$

where

$$F_1(\xi) = (c_1^2+\xi)^{1/2}, \quad G(\eta,\zeta) = \left[\frac{(c_1^2+\eta)(c_1^2+\zeta)}{(a_1^2-c_1^2)(b_1^2-c_1^2)}\right]^{1/2}.$$

That is, as given by Eqn. (3.16),

$$\varphi_0 = -E_0 \left[\frac{(c^2+\xi)(c^2+\eta)(c^2+\zeta)}{(a^2-c^2)(b^2-c^2)}\right]^{1/2}.$$

Under the quasi-static approximation, the distribution of electric potentials in the dielectric core, in the metal shell, and in the embedding dielectric matrix can be given by [233]:

$$\varphi_1 = D_1 F_1(\xi) G(\eta,\zeta), \quad -c^2 < \xi < 0, \tag{5.27}$$

$$\varphi_2 = [D_2 F_1(\xi) + D_3 F_2(\xi)] G(\eta,\zeta), \quad 0 \le \xi < t, \tag{5.28}$$

$$\varphi_3 = [-E_0 F_1(\xi) + D_4 F_2(\xi)] G(\eta,\zeta), \quad t \le \xi < \infty, \tag{5.29}$$

where

$$F_2(\xi) = F_1(\xi) \int_\xi^\infty \frac{dq}{(c_1^2+q) f_1(q)},$$

$$f_1(q) = [(a_1^2+q)(b_1^2+q)(c_1^2+q)]^{1/2}.$$

The coefficients D_1, D_2, D_3, and D_4 are unknown constants to be determined using the following boundary conditions. For electric potentials, the boundary conditions can be found from continuity conditions as:

$$\begin{aligned} \varphi_1 &= \varphi_2 \quad at \quad \xi = 0, \\ \varphi_2 &= \varphi_3 \quad at \quad \xi = t, \end{aligned} \tag{5.30}$$

and the normal components of the electric displacement vector can be found as:

$$\begin{aligned} \varepsilon_1 \frac{\partial \varphi_1}{\partial \xi} &= \varepsilon_2 \frac{\partial \varphi_2}{\partial \xi}, \quad at \quad \xi = 0, \\ \varepsilon_2 \frac{\partial \varphi_2}{\partial \xi} &= \varepsilon_3 \frac{\partial \varphi_3}{\partial \xi}, \quad at \quad \xi = t. \end{aligned} \tag{5.31}$$

where ε_1, ε_2, and, ε_3 are the electric permittivities of the dielectric core, metallic shell, and the host medium, respectively. By substituting Eqns. (5.27)-(5.29) in to Eqns. (5.30) and (5.31) and solving simultaneously, the unknown coefficients D_1, D_2, D_3, and D_4 can be obtained and are given by:

$$D_1 = -\frac{\varepsilon_2 \varepsilon_3}{Q} E_0, \tag{5.32}$$

$$D_2 = -\frac{[\varepsilon_3(\varepsilon_1 - \varepsilon_2)L_z^{(1)} + \varepsilon_2]}{Q} E_0, \tag{5.33}$$

$$D_3 = \frac{a_1 b_1 c_1 \varepsilon_3(\varepsilon_1 - \varepsilon_2)}{2Q} E_0, \tag{5.34}$$

$$D_4 = -\frac{a_2 b_2 c_2}{2Q} \left\{ f(\varepsilon_1 - \varepsilon_2)[L_z^{(2)}(\varepsilon_2 - \varepsilon_3) - \varepsilon_2] - (\varepsilon_2 - \varepsilon_3)[L_z^{(1)}(\varepsilon_1 - \varepsilon_2) + \varepsilon_2] \right\} E_0, \tag{5.35}$$

where $Q = p\Delta$, and

$$\Delta = \left[1 + \frac{L_z^{(2)} - L_z^{(1)}}{p} \right] - q\varepsilon_2 + \varepsilon_1 \varepsilon_3. \tag{5.36}$$

In this expression,

$$q = [1 - L_z^{(1)}/p]\varepsilon_1 + \{[L_z^{(2)} - 1]/p + 1\}\varepsilon_3$$

and

$$p = f L_z^{(2)}[L_z^{(2)} - 1] - L_z^{(1)}[L_z^{(2)} - 1], \quad f = a_1 b_1 c_1 / a_2 b_2 c_2.$$

The variables $L_z^{(1)}$ and $L_z^{(2)}$ are the geometrical factors for the inner and outer confocal ellipsoids, respectively.

Spheroids are a special class of ellipsoids, which have two axes of equal length. Hence,

only one of the geometrical factors is independent [60, 234]. The oblate spheroids are generated by rotating an ellipse about its minor axis, whereas the prolate spheroids are generated by rotating an ellipse about its major axis.

For oblate spheroid ($a_i = b_i > c_i$),

$$\begin{aligned} L_z^{(i)} &= \frac{g(e_i)}{2e_i^2}\left[\frac{\pi}{2} - \tan^{-1} g(e_i)\right] - \frac{g^2(e_i)}{2}, \\ L_x^{(i)} &= L_y^{(i)} = \frac{1}{2}\left(1 - L_z^{(i)}\right), \end{aligned} \tag{5.37}$$

where

$$g(e_i) = \sqrt{\frac{1-e_i^2}{e_i^2}}, \quad e_i^2 = 1 - \frac{c_i^2}{a_i^2}.$$

$i = 1, 2$ where 1 is for the inner spheroid and 2 for the outer spheroid.

For prolate spheroid ($a_i = b_i < c_i$),

$$\begin{aligned} L_z^{(i)} &= \frac{1-e_i^2}{2e_i^2}\left(-1 + \frac{1}{2e_i^2}\ln\frac{1+e_i}{1-e_i}\right), \\ L_x^{(i)} &= L_y^{(i)} = \frac{1}{2}\left(1 - L_z^{(i)}\right). \end{aligned} \tag{5.38}$$

where

$$e_i^2 = 1 - \frac{a_i^2}{c_i^2}.$$

Assuming that a uniform parallel electric field E_0 is directed along the z-axis, the local field in the dielectric core of the nanocomposite can be obtained with the help of $E_i = -\nabla\varphi_i$. Using this relation, the local field in the dielectric core can be given by:

$$E_1 = -\nabla\varphi_1 = K_1 E_0, \tag{5.39}$$

where K_1 is the factor that relates the local field in the dielectric core with the external incident electric field. Comparing Eqn. (5.32) with Eqn. (5.39), the coefficient of E_0, which is denoted by K_1 is called the enhancement factor (F), is given by:

$$F = \frac{\varepsilon_2\varepsilon_3}{Q}. \tag{5.40}$$

In this expression, ε_2 is the dielectric permittivity of the silver metal. From the Drude-Sommerfled model [235], this dielectric permittivity is complex and are given by Eqn. (5.21). By employing the correction of the bulk damping rate of the nanoparticle formula, the size dependent damping parameter γ for the nanospheroid can also be given by Eqn. (2.35), where its effective radius, r_{eff} is written by [236, 237]:

$$r_{eff} = [(a_2 - a_1)(b_2 - b_1)(c_2 - c_1)]^{1/3}. \tag{5.41}$$

Substituting Eqn. (5.21) into Eqn. (5.40) and considering the real quantity, the local field enhancement factor is given by:

$$|F|^2 = \frac{\varepsilon_3^2}{p^2}\left[\frac{\varepsilon_2'^2 + \varepsilon_2''^2}{\left((\varepsilon_2'^2 - \varepsilon_2''^2)(1 + \frac{L_z^{(2)} - L_z^{(1)}}{p}) - q\varepsilon_2' + \varepsilon_1\varepsilon_3\right)^2 + \varepsilon_2''^2\left(2\varepsilon_2'(1 + \frac{L_z^{(2)} - L_z^{(1)}}{p}) - q\right)^2}\right]. \tag{5.42}$$

In our analysis the nanostructure size is much smaller than the wavelength of the incident field. So the spheroidal nanocomposite is subjected to an almost uniform field. The particle then oscillates like a simple dipole with polarization proportional to the incident field. Therefore, the quasi-static approximation can be employed in the calculation. In this dipole approximation, the polarizabilities along the principal axes of the spheroids are given by [238]:

$$\alpha_1 = \alpha_2 = V\frac{\{(\varepsilon_2 - \varepsilon_3)\left[\varepsilon_2 + (\varepsilon_1 - \varepsilon_2)(L_1^{(1)} - fL_1^{(2)})\right] + f\varepsilon_2(\varepsilon_1 - \varepsilon_2)\}}{\{[\varepsilon_2 + (\varepsilon_1 - \varepsilon_2)(L_1^{(1)} - fL_1^{(2)})][\varepsilon_3 + (\varepsilon_2 - \varepsilon_3)L_1^{(2)}] + fL_1^{(2)}\varepsilon_2(\varepsilon_1 - \varepsilon_2)\}}, \tag{5.43}$$

$$\alpha_3 = V\frac{\{(\varepsilon_2 - \varepsilon_3)\left[\varepsilon_2 + (\varepsilon_1 - \varepsilon_2)(L_3^{(1)} - fL_3^{(2)})\right] + f\varepsilon_2(\varepsilon_1 - \varepsilon_2)\}}{\{[\varepsilon_2 + (\varepsilon_1 - \varepsilon_2)(L_3^{(1)} - fL_3^{(2)})][\varepsilon_3 + (\varepsilon_2 - \varepsilon_3)L_3^{(2)}] + fL_3^{(2)}\varepsilon_2(\varepsilon_1 - \varepsilon_2)\}}, \tag{5.44}$$

where $V = 4\pi a_2 b_2 c_2/3$ is the total nanocomposite particle volume.

From polarizability, the scattering and absorption cross sections of a coated nanoellip-

soid under quasi-static approximation can be expressed as [239]:

$$C_{scat} = \frac{k^4}{18\pi}\left[2|\alpha_1|^2 + |\alpha_3|^2\right], \quad C_{abs} = \frac{k}{3} Im\left[2(\alpha_1) + (\alpha_3)\right]. \tag{5.45}$$

where k is the wavenumber in the medium which strongly depends on the shape of the nanostructure, is given by [237]:

$$k = \frac{2\pi(a_2 b_2 c_2)^{1/3}}{\lambda}$$

and λ is the walelength of the incident light.

5.3 Results and discussions

In this study, all the four core-shell NCs (spherical, cylindrical, oblate, and prolate spheroids) consist of the same core (CdSe) and the same shell (Au) materials. On top of this, all of them were placed in the same host medium (SiO_2) with dielectric constant, $\varepsilon_3 = 2.5$. Moreover, their corresponding radii are set to the same values (for sphere, cylinder, and oblate spheroid: $r_1 = a_1 = b_1 = 4\ nm$ and $r_2 = a_2 = b_2 = 12\ nm$; for prolate spheroid: $c_1 = 4\ nm$ and $c_2 = 12\ nm$). Then, their optical properties were investigated according to their shapes and the results were discussed as follows.

5.3.1 Local field enhancement factor of core-shell nanocomposites

With the uniform shell thickness of 8 nm, the local field enhancements of spherical and cylindrical core-shell NCs have two peaks while those of the oblate and the prolate spheroids show three peaks, all in the visible range of spectrum (Figs. 5.4(a) and 5.4(b)). From the same figure, it could be observed that all the enhancement peaks have different intensities and wavelengths. Comparing the first (counting from the short to the long wavelength) peaks of electric field enhancements of four of them (Fig. 5.4), that of the cylindrical core-shell relatively occurs at the shortest wavelength ($\lambda = 467\ nm$) while that of the sphere is achieved at the longest wavelength ($\lambda =$

483 *nm*).

When the highest intense resonance of electric field enhancement is required, spherical core-shell nanocomposite is preferred to cylindrical and spheroidal core-shells of the same size and compositions. For the considered sizes and parameters, even the smallest value (2775) of LFEF of the spherical core-shell is 11.42 and 10.09 times larger than the biggest values of oblate (243) and prolate (275) core-shells, respectively (Table 5.1).

Table 5.1: LFEF of spherical, cylindrical, oblate, and prolate core-shell NCs.

Shape	Shell thickness (*nm*)	Peak 1		Peak 2		Peak 3	
		(*nm*)	Peak	(*nm*)	Peak	(*nm*)	Peak
Spherical	8	482	2775	552	7878	_	_
Cylindrical	8	467	397	600	2445	_	_
Oblate	8	481	34	547	227	579	243
Prolate	8	480	42	548	137	606	275

It can also be seen that the last two peaks of the field enhancements are more closer to each other for oblate spheroid ($\Delta\lambda = 32$ *nm*) than its corresponding prolate shape ($\Delta\lambda = 58$ *nm*), showing that prolate core-shell spheroid can be tuned over wider range of the spectrum (Fig. 5.4(b)). Thus, core-shell prolate spheroid nanocomposite shows greater structural tunability and larger intensity of local field enhancements than its corresponding oblate nanocomposite. This finding agrees with the previously reported study that emphasized the tunability of dielectric core-metallic shell prolate spheroid than any dielectric-metal nanostructures [240]. When peaks of the LFEF of the two forms of the spheroids are compared (Fig. 5.4(b)), nearly at $\lambda = 547$ *nm*, the intensity is larger for oblate spheroid (≈ 227) than that of the prolate shape (≈ 137). This result agrees with previous study that showed bigger magnitude of field enhancement factor for oblate than the prolate form [241]. Moreover, another similarity is also observed with the former study that for both the oblate and prolate forms, larger values of field enhancements were achieved near the wavelength of 600 *nm*. In the present study, larger field enhancement values were observed at $\lambda \approx 579$ *nm* and $\lambda \approx 606$ *nm* for

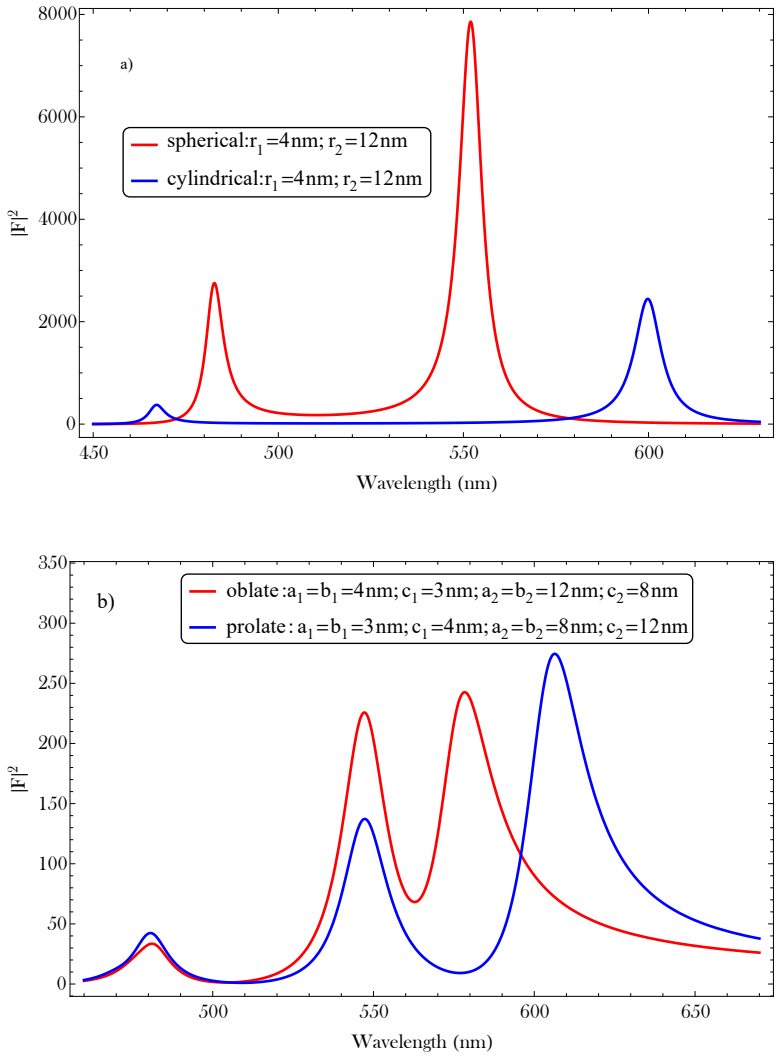

Figure 5.4: LFEF of: a) spherical and cylinderical and b) oblate and prolate core-shell NCs.

oblate and prolate forms, respectively (Table 5.1). From all these findings, it can be said that shape of NCs affects properties such as peak intensity, resonance wavelength, and number of peaks of nanostructures, which were also indicated in previous studies [242].

5.3.2 Absorption cross-sections of core-shell nanocomposites

For the same composition and the same material parameters, all the three absorption peaks of prolate spheroid are lower than that of its corresponding oblate form. Out of

these peaks, the first and the third (counting from the short to the long wavelength) peaks of the prolate are relatively red shifted as compared to the oblate one (Fig. 5.5(c)). Even when peaks of all the absorption cross-sections of the four different

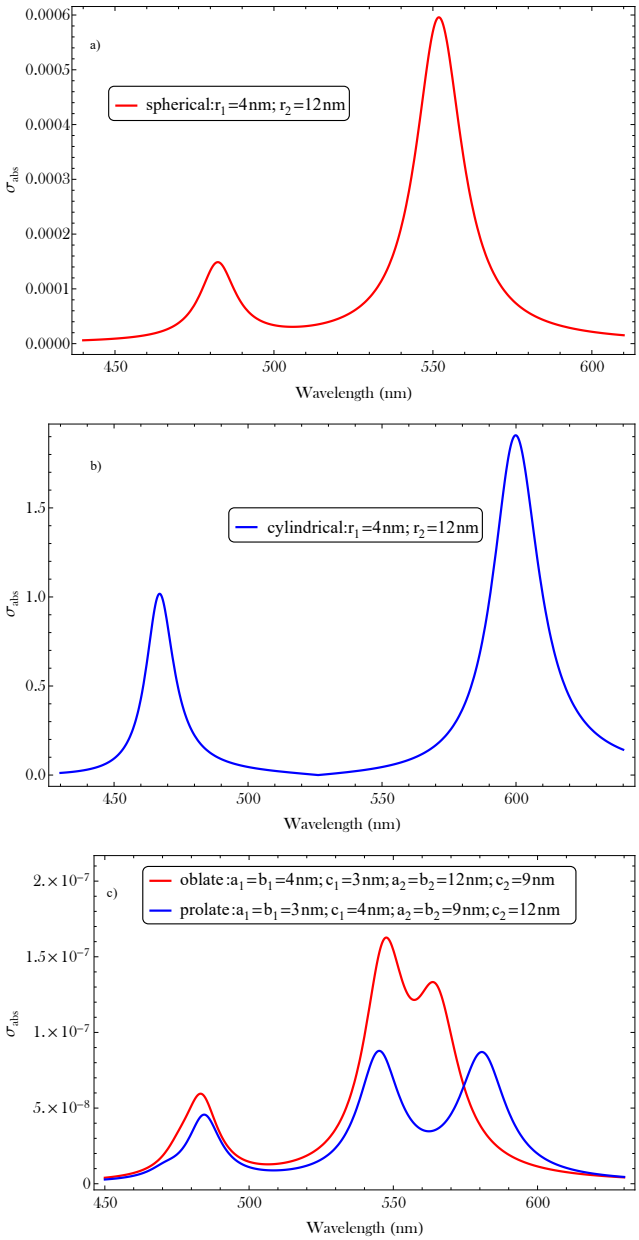

Figure 5.5: Absorption cross-sections of: a) spherical, b) cylindrical, and c) oblate and prolate core-shell NCs.

shapes of the NCs are compared (Fig. 5.5), that of the prolate spheroid is the lowest while that of the cylindrical shape is the highest. Especially, the first peak of the cylindrical shape is relatively achieved at the shortest wavelength ($\lambda \approx 467\ nm$), whereas

that of the corresponding wavelengths of the spherical, the oblate and the prolate core-shell nanoparticles are about 482 *nm*, 484 *nm*, and 485 *nm*, respectively.

The study also show that the number of peaks of absorption cross-sections also vary with the shapes of the NCs. That is, spherical and cylindrical shapes have two peaks while there are three peaks in oblate and prolate spheroidal NCs. Regarding the number of peaks and patterns of absorption cross-sections, this result is in agreement with previous findings [243]. Where the peaks are the same in number in different shape nanostructures, they are different in magnitudes, showing that the shape of core-shell NCs affects the number and the magnitudes of peaks of the absorption cross-sections.

Out of three observable peaks in the absorption spectrum of spheroidal NCs (Fig. 5.5(c)), the first peaks are attributed to the transverse resonance from the outer gold metal surface while the last two peaks are attributed to the longitudinal resonance from the inner and the outer surfaces of the same metallic shell, respectively. Similar results were also shown in previous research findings too [244]. Such gold coated three localized surface plasmon resonance peaks which are intense and are clearly separate, have good potential application in multi-channel sensing.

5.3.3 Extinction cross-sections of core-shell nanocomposites

In this study, we have also investigated the extinction cross-sections of the same NCs (Fig. 5.6 (a-c)). For the same composition, core radii, shell thickness, and embedding medium, the extinction spectra shows different number of peaks, peak values and positions for spherical, cylindrical, oblate and prolate core-shell nanoparticles. The peak values and the wavelengths at which those peaks achieved were shown in Table 5.2 for all the considered core-shell NCs.

It seems interesting to note that, for spherical and cylindrical NCs, peaks 1 and 2 of LFEF are achieved at the same frequencies with the corresponding peaks of extinction cross-sections (Tables 5.1 and 5.2). While investigating the extinction spectra, we have also seen the scattering cross-sections for those NCs. However, the peak values are so small as compared to the absorption peak values and has no significant changes on

the extinction peak magnitudes. This in turn indicates that smaller nanoparticles are

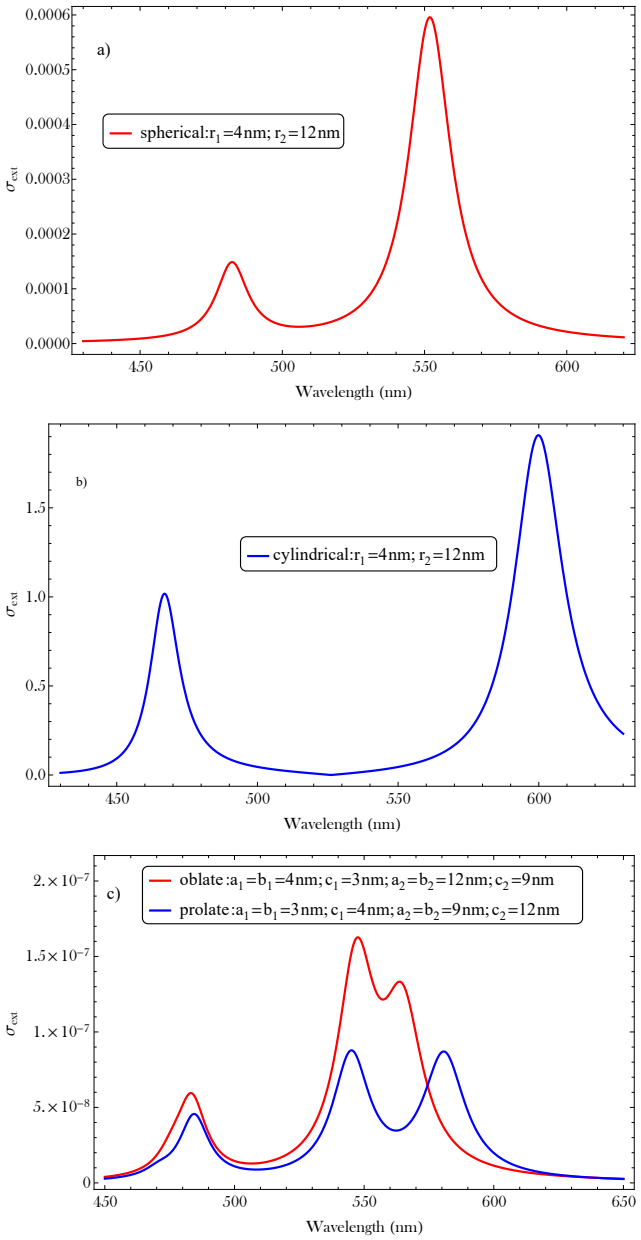

Figure 5.6: Extinction cross-sections of: a) spherical, b) cylindrical, and c) oblate and prolate core-shell NCs.

mainly absorptive than scatterers. Among all the different nanostructures presented, the cylindrical core-shell nanocomposite shows the largest extinction peak values in the visible range of electromagnetic spectrum, whereas the smallest peak value is observed for the prolate spheroid. Moreover, peaks 2 and 3 of the prolate shape show the same values which were not observed in the rest three shapes. Whatever the number

Table 5.2: Extinction cross-sections of spherical, cylindrical, oblate, and prolate core-shell NCs.

Shape	Shell thickness(nm)	Peak 1		Peak 2		Peak 3	
		(nm)	Peak	(nm)	Peak	(nm)	Peak
Spherical	8	482	0.00015	552	0.0006	_	_
Cylindrical	8	467	1.02	600	1.9	_	_
Oblate	8	484	$5.98\text{x}10^{-8}$	548	$16.3\text{x}10^{-8}$	546	$13.3\text{x}10^{-8}$
Prolate	8	485	$4.51\text{x}10^{-8}$	546	$8.77\text{x}10^{-8}$	582	$8.77\text{x}10^{-8}$

and the values of the extinction spectra, all of them lie in the visible range of electromagnetic spectrum for the different shapes indicated in figure 5.6.

The result also reveals that the resonance position of peak 1 is slightly red shifted as the shape of core-shell nanoparticles changes from cylindrical to spherical, oblate and prolate, respectively, while blue shift is observed as the shapes change in the reverse order. These shifts cause peaks 1 and 2 to come close to each other in prolate spheroid than any other shapes investigated in this study. Previous investigations also support our study that there are two extinction peaks of dielectric core-metallic shell spherical nanoparticles [245].

Here, it is interesting to note that the extinction cross-sections behave differently for different shapes of core-shell NCs. Hence, it can be said that the shape of a core-shell nanoparticles controls the resonance frequencies of its plasmon modes and hence its optical properties.

Another investigation that we made is how the extinction property of core-shell nanocomposites are affected by the dielectric function of the host medium. When the dielectric function of the host medium increases, the extinction peak of spherical nanoshell at the outer interface of the metal increases and red shifted. However, the peaks at the inner interface of the silver metal decreases. When we keep on increasing the dielectric function of the embedding medium, the intensity of the extinction cross section of the spherical nanoshell starts declining (Fig. 5.7 (a)). On the other hand, when we change the shape of the nanoshell from spherical to cylindrical, the peaks of the

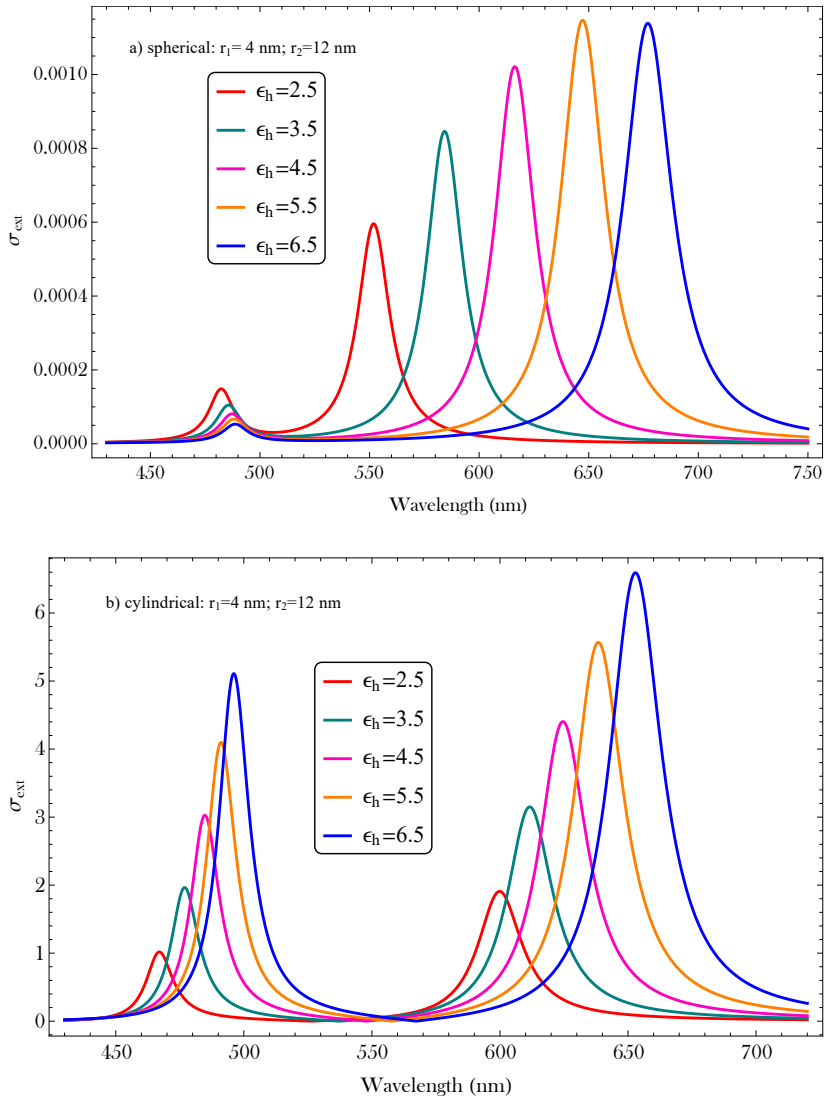

Figure 5.7: Effects of host medium on the extinction cross-sections of: a) spherical and b) cylindrical core-shell NCs.

extinction cross section continuously increase at the inner and outer interfaces of the metal, with an increase in the permittivity of the host matrix (Fig. 5.7 (b)). Hence, the absorption and scattering cross sections of the cylindrical nanoshell can be increased and decreased by increasing and decreasing the dielectric medium of the host matrix, respectively.

When the dielectric function of the host matrix increases, all the three peaks of extinction cross section of spheroidal core-shell NCs show red shift (Fig. 5.8 (a) and

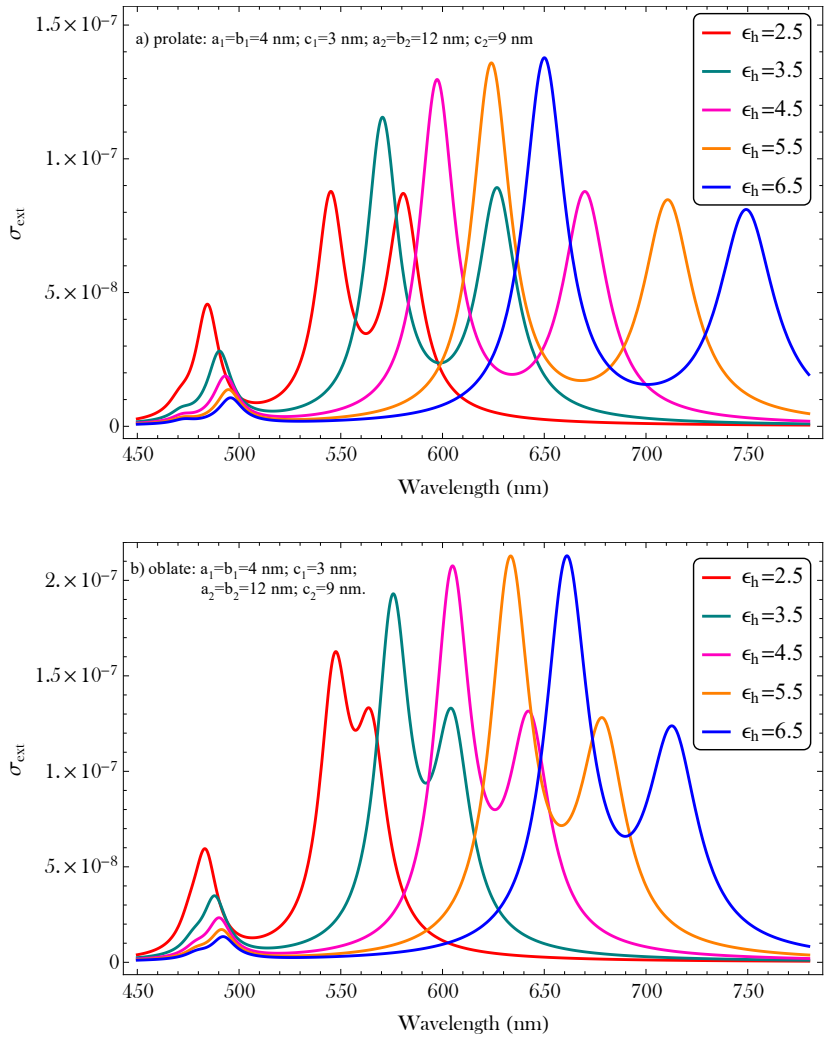

Figure 5.8: Effects of host medium on the extinction cross-sections of: a) prolate and b) oblate core-shell NCs.

(b)). Out of the three observable peaks, the first and third peaks (counted from left to right) show a decreasing tendency, while the second peaks are increasing, especially more clearly in the oblate form (Fig. 5.8 (b)). Overall, in different types of core-shell NCs, the change in the dielectric function of the embedding medium produces extinction spectra of different properties. Hence, the type of host matrix affects the optical properties of nanoshell structures.

5.4 Conclusions

We studied core- shell (CdSe@Au) spherical, cylindrical, oblate, and prolate NCs, embedded in a host medium (SiO_2). Then, we investigated their LFEF and optical cross-sections theoretically and numerically using quasistatic approximation. The results show that additional peaks are observed in LFEF, absorption, and extinction cross-sections in oblate and prolate core-shell spheroids as compared to spherical and cylindrical core-shell nanoparticles. Where the number of peaks are the same for different shapes, the values (intensities) are found to be different. From the three peaks of LFEF of the spheroids, the last two of them are more closer to each other for oblate spheroid than its corresponding prolate shape, indicating that the prolate core-shell spheroid can show greater structural tunability. Moreover, two out of the three peaks of LFEF of the prolate spheroid shows larger intensity than its corresponding oblate nanocomposite in electromagnetic spectrum. We also found that spherical core-shell nanocomposite is characterized by the highest LFEF than cylindrical and spheroidal core-shell NCs of the same size and compositions. Under this considerations, even the smallest value of LFEF of the spherical core-shell is 11.42 and 10.09 times larger than the biggest values of oblate and prolate core-shells, respectively. Another finding of our study shows, for spherical and cylindrical NCs, the first two peaks of LFEF and extinction cross-sections are achieved at the same corresponding frequencies.

The study further indicated that for the same compositions and the same material parameters, the absorption peaks of prolate spheroid are lower than and relatively red shifted as compared to its corresponding oblate form. Among all the different nanostructures presented, the cylindrical core-shell shows the largest extinction peak values in the visible range of electromagnetic spectrum, whereas the smallest peak value is observed for the prolate spheroid. In the present study, we showed the possibility of controlling the optical properties of core-shell nanoparticles by altering their shapes without changing their sizes and compositions. Moreover, the change in the dielectric function of the embedding medium also affects the extinction spectra of core-shell NCs. The same change in the pemittivity of the host medium shows different effects

in different shapes of core-shell NCs. As the intensities and positions of plasmonic resonance peaks of core-shell NCs can be tuned by altering their shapes, they are appropriate alternatives for various applications in many optical devices. Especially, gold coated surface plasmon resonance peaks observed in the core-shell spheroids have good potential application in multi-channel sensing.

Chapter 6

Summary of Major Findings and Future Work

6.1 Summary of the Work and Major Findings

The main objective of this dissertation is theoretical and numerical investigations of the plasmonic effects and the effects of size, shape, and type of host matrix on the optical properties of core-shell NCs. In the first part of our work, we studied spherical core-shell NCs of CdSe@Ag and CdSe@ZnSe@Ag by using SiO_2 as an embedding medium for each of them. Then, we analyzed the effects of the sizes (thicknesses) of the core, the spacer, and the metallic shell on the LFEF of the core-shell NCs. In the second part of this work, we investigated CdSe@Au core-shell NCs in spherical, cylindrical, prolate, and oblate shapes, all with the same inner and outer radii, and similarly by placing each of them in an external host matrix of SiO_2. In both parts of our work, we have sequentially increased the permittivity of the host medium from 2.5 to 6.5 and investigated how the LFEF and the optical cross sections of spherical, cylindrical, and spheroidal core-shell NCs change. To achieve these objectives, we used the Drude-Lorentz model and Laplace's equation under quasi-static approximation, and the major findings of the study are summarized as follows:

■ **For CdSe@Ag core-shell NCs in SiO_2 host matrix:**

☞ when the core radius decreases and the shell thickness increases simultaneously at constant shell radius, the local field is enhanced and the surface plasmon peaks shift to the higher energy.

☞ when the NP size increases by keeping its core size constant, the LFEF at the interface of Ag-SiO_2 is enhanced and is accompanied by a blue shift.

☞ the LFEF is higher when the size of the core is reduced than when the thickness of the shell is increased.

☞ when both the core and the shell radii increase simultaneously, the resonance peaks of LFEF are significantly lowered at the interface of Ag@SiO_2.

☞ whether the shell size is constant or decreased, increasing the core size led to lower LFEF, showing that the core size of the NP is a crucial parameter to increase or decrease the LFEF of CdSe@Ag spherical core-shell NPs.

☞ increasing the dielectric function of the embedding medium greatly enhances the LFEF of nanoshell particles, than does increasing the metallic shell thickness.

■ **For CdSe@ZnSe@Ag core-shell NCs in SiO_2 host matrix:**

☞ the magnitudes of the resonance peaks of LFEF rise while the radius of ZnSe is fixed and that of the core and shell increases.

☞ by increasing the spacer size at constant core and NP radii, the resonance peaks of LFEF decrease.

☞ by increasing the shell size and maintaining the radii of the core and the spacer constant, the field enhancement factor increases.

☞ among all the size combinations of the core, the spacer, and the shell, comparatively, the largest peak of LFEF is obtained when the spacer size is the thinnest.

■ **For CdSe@Au core-shell NCs of various geometries in SiO_2 host matrix:**

✍ the local field enhancements of spherical and cylindrical core-shell NCs have two peaks, while those of the oblate and the prolate spheroids show three peaks.

✍ in comparison to cylindrical and spheroidal core-shells of the same size and composition, spherical core-shell NCs exhibit the highest field enhancement.

✍ prolate spheroid core-shell nanocomposite shows greater structural tunability and a larger LFEF than its corresponding oblate nanocomposite.

✍ among the four different shapes investigated, the peaks of all the extinction cross-sections of the prolate are the lowest, while those of the cylindrical shape are the highest.

✍ the shape of a core-shell nanoparticles controls the resonance frequencies of its plasmon modes and hence its optical properties.

✍ the same change in the pemittivity of the host medium produces different optical effects in different shapes of core-shell NCs.

6.2 Future Work

To use nanoparticles in several areas of applications, investigating their various properties and understanding their characteristics is one of the hot areas of research. Theoretical and numerical studies of the optical properties of core-shell NCs are not enough to address the vast areas of nanoparticles. In addition to the effects of plasmons, sizes, and shapes of core-shell NCs, how the number of layers influences their optical properties is also an essential parameter to be considered. Their electronic and magnetic properties which can also be studied through computational and experimental methods are too important. All these indicate that there are several research agendas to be investigated. From these perspectives, some of the general directions for our future work are as follows:

- ➢ Theoretical study of the effects of the number of layers and interfacials on the optical properties of multi-layered core-shell NCs.
- ➢ Effects of shape on the optical bistabitlity of metallo-dielectric core-shell NCs.
- ➢ Effects of *Ag* doping on the electronic and optical properties of CdSe@ZnSe core-shell quantum dots.
- ➢ Magnetic and electronic properties of zinc-chalcogenide materials using first-principles calculations.

Bibliography

[1] Murugan Amudha and KK Shanmugasundaram. Biosynthesis and characterization of silver nanoparticles using the aqueous extract of vitex negundo linn. *World Journal of Pharmacy and Pharmaceutical Sciences (WJPPS)*, 3(8):1385–1393, 2014.

[2] V Srinivas. What are the uses and applications of nanoparticles? *American Journal of Preventive Medicine and Public Health*, 7(6), 2021.

[3] Mihail C Roco, Chad A Mirkin, and Mark C Hersam. Nanotechnology research directions for societal needs in 2020: summary of international study. *Journal of nanoparticle research*, 13:897–919, 2011.

[4] KS Kavitha, Syed Baker, D Rakshith, HU Kavitha, HC Yashwantha Rao, BP Harini, and S Satish. Plants as green source towards synthesis of nanoparticles. *Int Res J Biol Sci*, 2(6):66–76, 2013.

[5] M Jannathul Firdhouse, P Lalitha, Shubashini K Sripathi, et al. Novel synthesis of silver nanoparticles using leaf ethanol extract of pisonia grandis (r. br). *Der Pharma Chemica*, 4(6):2320–2326, 2012.

[6] Rakesh Kumar, Mohit Kumar, and Gaurav Luthra. Fundamental approaches and applications of nanotechnology: A mini review. *Materials Today: Proceedings*, 2023.

[7] Pınar Koç and Ahmet Gülmez. Analysis of relationships between nanotechnol-

ogy applications, mineral saving and ecological footprint: Evidence from panel fourier cointegration and causality tests. *Resources Policy*, 74:102373, 2021.

[8] Michel Vert, Yoshiharu Doi, Karl-Heinz Hellwich, Michael Hess, Philip Hodge, Przemyslaw Kubisa, Marguerite Rinaudo, and François Schué. Terminology for biorelated polymers and applications (iupac recommendations 2012). *Pure and Applied Chemistry*, 84(2):377–410, 2012.

[9] William L Barnes. Particle plasmons: Why shape matters. *American Journal of Physics*, 84(8):593–601, 2016.

[10] Stefan A Maier and Harry A Atwater. Plasmonics: Localization and guiding of electromagnetic energy in metal/dielectric structures. *Journal of applied physics*, 98(1):10, 2005.

[11] Younan Xia, Peidong Yang, Yugang Sun, Yiying Wu, Brian Mayers, Byron Gates, Yadong Yin, Franklin Kim, and Haoquan Yan. One-dimensional nanostructures: synthesis, characterization, and applications. *Advanced materials*, 15(5):353–389, 2003.

[12] Sang Hyuk Im, Yun Tack Lee, Benjamin Wiley, and Younan Xia. Large-scale synthesis of silver nanocubes: the role of hcl in promoting cube perfection and monodispersity. *Angewandte Chemie International Edition*, 44(14):2154–2157, 2005.

[13] Jill E Millstone, Sungho Park, Kevin L Shuford, Lidong Qin, George C Schatz, and Chad A Mirkin. Observation of a quadrupole plasmon mode for a colloidal solution of gold nanoprisms. *Journal of the American Chemical Society*, 127(15):5312–5313, 2005.

[14] Colleen L Nehl, Hongwei Liao, and Jason H Hafner. Optical properties of star-shaped gold nanoparticles. *Nano letters*, 6(4):683–688, 2006.

[15] Jin-Ho Choy, Eue-Soon Jang, Jung-Hee Won, Jae-Hun Chung, Du-Jeon Jang, and Young-Woon Kim. Hydrothermal route to zno nanocoral reefs and nanofibers. *Applied physics letters*, 84(2):287–289, 2004.

[16] Yugang Sun and Younan Xia. Shape-controlled synthesis of gold and silver nanoparticles. *science*, 298(5601):2176–2179, 2002.

[17] Rebecca Anthony and Uwe Kortshagen. Photoluminescence quantum yields of amorphous and crystalline silicon nanoparticles. *Physical Review B*, 80(11):115407, 2009.

[18] SK Simakov. Nano-and micron-sized diamond genesis in nature: An overview. *Geoscience Frontiers*, 9(6):1849–1858, 2018.

[19] SK Simakov, A Kouchi, NN Mel'nik, V Scribano, Y Kimura, T Hama, N Suzuki, H Saito, and T Yoshizawa. Nanodiamond finding in the hyblean shallow mantle xenoliths. *Scientific Reports*, 5(1):1–8, 2015.

[20] Ramanathan Nagarajan and T Alan Hatton. *Nanoparticles: synthesis, stabilization, passivation, and functionalization*. ACS Publications, 2008.

[21] John MC Plane. Cosmic dust in the earth's atmosphere. *Chemical Society Reviews*, 41(19):6507–6518, 2012.

[22] Herbert A Zook. Spacecraft measurements of the cosmic dust flux. In *Accretion of extraterrestrial matter throughout EarthâĂŹs history*, pages 75–92. Springer, 2001.

[23] Klaus D Sattler. *Handbook of nanophysics: nanoparticles and quantum dots*. CRC press, 2016.

[24] Liudmila Nickelson. *Electromagnetic theory and plasmonics for engineers*. Springer, 2018.

[25] Michael Faraday. X. the bakerian lecture. experimental relations of gold (and other metals) to light. *Philosophical transactions of the Royal Society of London*, (147):145–181, 1857.

[26] David Thompson. Michael faraday's recognition of ruby gold: the birth of modern nanotechnology: His 1857 lecture to the royal society in london. *Gold Bulletin*, 40(4):267–269, 2007.

[27] Uwe Kreibig and Michael Vollmer. *Optical properties of metal clusters*, volume 25. Springer Science & Business Media, 2013.

[28] Richard Feynman. Nanotechnology. *Caltechs Eng. Sci*, 23:22–36, 1960.

[29] Norio Taniguchi. On the basic concept of nanotechnology. *Proceeding of the ICPE*, 1974.

[30] D Patrick O'Neal, Leon R Hirsch, Naomi J Halas, J Donald Payne, and Jennifer L West. Photo-thermal tumor ablation in mice using near infrared-absorbing nanoparticles. *Cancer letters*, 209(2):171–176, 2004.

[31] Vladimir P Zharov, Elena N Galitovskaya, Carl Johnson, and Thomas Kelly. Synergistic enhancement of selective nanophotothermolysis with gold nanoclusters: potential for cancer therapy. *Lasers in Surgery and Medicine: The Official Journal of the American Society for Laser Medicine and Surgery*, 37(3):219–226, 2005.

[32] Rabih O Darouiche, Issam I Raad, Stephen O Heard, John I Thornby, Olivier C Wenker, Andrea Gabrielli, Johannes Berg, Nancy Khardori, Hend Hanna, Ray Hachem, et al. A comparison of two antimicrobial-impregnated central venous catheters. *New England Journal of Medicine*, 340(1):1–8, 1999.

[33] Ivan H El-Sayed, Xiaohua Huang, and Mostafa A El-Sayed. Surface plasmon resonance scattering and absorption of anti-egfr antibody conjugated gold nanoparticles in cancer diagnostics: applications in oral cancer. *Nano letters*, 5(5):829–834, 2005.

[34] L Tong. Y zhao, tb huff, mn hansen, a. wei, jx cheng. *Adv. Mater. Deerfield*, 19:3136, 2007.

[35] Paul Podsiadlo, Vladimir A Sinani, Joong Hwan Bahng, Nadine Wong Shi Kam, Jungwoo Lee, and Nicholas A Kotov. Gold nanoparticles enhance the anti-leukemia action of a 6-mercaptopurine chemotherapeutic agent. *Langmuir*, 24(2):568–574, 2008.

[36] Jeffrey N Anker, W Paige Hall, Olga Lyandres, Nilam C Shah, Jing Zhao, and Richard P Van Duyne. Biosensing with plasmonic nanosensors. *Nature materials*, 7(6):442–453, 2008.

[37] Koen Raemdonck, Joseph Demeester, and Stefaan De Smedt. Advanced nanogel engineering for drug delivery. *Soft Matter*, 5(4):707–715, 2009.

[38] Hai-Long Jiang, Tomoki Akita, and Qiang Xu. A one-pot protocol for synthesis of non-noble metal-based core–shell nanoparticles under ambient conditions: toward highly active and cost-effective catalysts for hydrolytic dehydrogenation of nh 3 bh 3. *Chemical Communications*, 47(39):10999–11001, 2011.

[39] Thomas Hartman, Caterina S Wondergem, Naresh Kumar, Albert van den Berg, and Bert M Weckhuysen. Surface-and tip-enhanced raman spectroscopy in catalysis. *The journal of physical chemistry letters*, 7(8):1570–1584, 2016.

[40] Prashant V Kamat. Photophysical, photochemical and photocatalytic aspects of metal nanoparticles, 2002.

[41] Emil Prodan, Corey Radloff, Naomi J Halas, and Peter. Nordlander. A hybridization model for the plasmon response of complex nanostructures. *science*, 302(5644):419–422, 2003.

[42] Sara Gómez de Pedro. *(BIo) analytical microsystems based on the use of nanoparticles. Microreactors for the synthesis of nanoparticles*. Universitat Autònoma de Barcelona, 2014.

[43] Hari Singh Nalwa. *Handbook of surfaces and interfaces of materials, five-volume set*. Elsevier, 2001.

[44] Arthur L Aden and Milton Kerker. Scattering of electromagnetic waves from two concentric spheres. *Journal of Applied Physics*, 22(10):1242–1246, 1951.

[45] RH Morriss and LF Collins. Optical properties of multilayer colloids. *The Journal of Chemical Physics*, 41(11):3357–3363, 1964.

[46] Ghasan Fahim Huseien. Potential applications of core-shell nanoparticles in construction industry revisited. *Applied Nano*, 4(2):75–114, 2023.

[47] SJ Oldenburg, RD Averitt, SL Westcott, and NJ Halas. Nanoengineering of optical resonances. *Chemical Physics Letters*, 288(2-4):243–247, 1998.

[48] Austin M Derfus, Warren CW Chan, and Sangeeta N Bhatia. Probing the cytotoxicity of semiconductor quantum dots. *Nano letters*, 4(1):11–18, 2004.

[49] HS Mansur. Wiley interdiscip. *Rev.: Nanomed. Nanobiotechnol*, 2(2):113–129, 2010.

[50] Xiaogang Peng, Michael C Schlamp, Andreas V Kadavanich, and A Paul Alivisatos. Epitaxial growth of highly luminescent cdse/cds core/shell nanocrystals with photostability and electronic accessibility. *Journal of the American Chemical Society*, 119(30):7019–7029, 1997.

[51] Guo-Wei Huang, Chun-Yen Chen, Kun-Chan Wu, Moawia O Ahmed, and Pi-Tai Chou. One-pot synthesis and characterization of high-quality cdse/znx (x= s, se) nanocrystals via the cdo precursor. *Journal of Crystal Growth*, 265(1-2):250–259, 2004.

[52] Bashir O Dabbousi, Javier Rodriguez-Viejo, Frederic V Mikulec, Jason R Heine, Hedi Mattoussi, Raymond Ober, Klavs F Jensen, and Moungi G Bawendi. (cdse) zns core- shell quantum dots: synthesis and characterization

of a size series of highly luminescent nanocrystallites. *The Journal of Physical Chemistry B*, 101(46):9463–9475, 1997.

[53] Klavs F Jensen Chris B Murray Danek, Michal and Moungi G Bawendi. Synthesis of luminescent thin-film cdse/znse quantum dot composites using cdse quantum dots passivated with an overlayer of znse. *Chemistry of Materials*, 8(1):173–180, 1996.

[54] Yong-Ji Lee, Tae-Geun Kim, and Yun-Mo Sung. Lattice distortion and luminescence of cdse/znse nanocrystals. *Nanotechnology*, 17(14):3539, 2006.

[55] Encai Hao, George C Schatz, and Joseph T Hupp. Synthesis and optical properties of anisotropic metal nanoparticles. *Journal of fluorescence*, 14(4):331–341, 2004.

[56] E Stefan Kooij and Bene Poelsema. Shape and size effects in the optical properties of metallic nanorods. *Physical Chemistry Chemical Physics*, 8(28):3349–3357, 2006.

[57] Benjamin J Wiley, Sang Hyuk Im, Zhi-Yuan Li, Joeseph McLellan, Andrew Siekkinen, and Younan Xia. Maneuvering the surface plasmon resonance of silver nanostructures through shape-controlled synthesis, 2006.

[58] Kyeong-Seok Lee and Mostafa A El-Sayed. Gold and silver nanoparticles in sensing and imaging: sensitivity of plasmon response to size, shape, and metal composition. *The Journal of Physical Chemistry B*, 110(39):19220–19225, 2006.

[59] Stephan Link and Mostafa A El-Sayed. Spectral properties and relaxation dynamics of surface plasmon electronic oscillations in gold and silver nanodots and nanorods, 1999.

[60] Craig F Bohren and Donald R Huffman. *Absorption and scattering of light by small particles*. John Wiley & Sons, 2008.

[61] Hendrik Christoffel Hulst and Hendrik C van de Hulst. *Light scattering by small particles*. Courier Corporation, 1981.

[62] Michael Quinten. *Optical properties of nanoparticle systems: Mie and beyond*. John Wiley & Sons, 2010.

[63] Georg Busch and Horst Schade. *Lectures on Solid State Physics: International Series in Natural Philosophy*, volume 79. Elsevier, 2013.

[64] Philip Hofmann. *Solid state physics: an introduction*. John Wiley & Sons, 2022.

[65] S Farjami Shayesteh and Matin Saie. The effect of surface plasmon resonance on optical response in dielectric (core)–metal (shell) nanoparticles. *Pramana*, 85:1245–1255, 2015.

[66] Paul Mulvaney. Surface plasmon spectroscopy of nanosized metal particles. *Langmuir*, 12(3):788–800, 1996.

[67] Gustav Mie. A contribution to the optics of turbid media, especially colloidal metallic suspensions. *Ann. Phys*, 25(4):377–445, 1908.

[68] Alexei A Maradudin, J Roy Sambles, and William L Barnes. *Modern plasmonics*. Elsevier, 2014.

[69] Katherine A Willets and Richard P Van Duyne. Localized surface plasmon resonance spectroscopy and sensing. *Annu. Rev. Phys. Chem.*, 58:267–297, 2007.

[70] Mark I Stockman. Nanoplasmonics: past, present, and glimpse into future. *Optics express*, 19(22):22029–22106, 2011.

[71] Y Wang, EW Plummer, and K Kempa. Foundations of plasmonics. *Advances in Physics*, 60(5):799–898, 2011.

[72] W Lang. Loss of velocity of moderately fast electrons in passing through thin metal foils. *Optik*, 3:233, 1948.

[73] David Pines and David Bohm. A collective description of electron interactions: Ii. collective vs individual particle aspects of the interactions. *Physical Review*, 85(2):338, 1952.

[74] David Pines. Collective energy losses in solids. *Reviews of modern physics*, 28(3):184, 1956.

[75] Rufus H Ritchie. Plasma losses by fast electrons in thin films. *Physical review*, 106(5):874, 1957.

[76] CJ Powell and JB Swan. Origin of the characteristic electron energy losses in magnesium. *Physical Review*, 116(1):81, 1959.

[77] EA Stern and RA Ferrell. Surface plasma oscillations of a degenerate electron gas. *Physical Review*, 120(1):130, 1960.

[78] Andreas Otto. Excitation of nonradiative surface plasma waves in silver by the method of frustrated total reflection. *Zeitschrift für Physik A Hadrons and nuclei*, 216(4):398–410, 1968.

[79] Chris D Geddes. *Reviews in Plasmonics 2010*. Springer, 2012.

[80] Song-Yuan Ding, Jun Yi, Jian-Feng Li, Bin Ren, De-Yin Wu, Rajapandiyan Panneerselvam, and Zhong-Qun Tian. Nanostructure-based plasmon-enhanced raman spectroscopy for surface analysis of materials. *Nature Reviews Materials*, 1(6):1–16, 2016.

[81] Shuwen Zeng, Dominique Baillargeat, Ho-Pui Ho, and Ken-Tye Yong. Nanomaterials enhanced surface plasmon resonance for biological and chemical sensing applications. *Chemical Society Reviews*, 43(10):3426–3452, 2014.

[82] J Zenneck. On the propagation of plane electromagnetic waves along a planar conductor surface and its relationship to wireless telegraphy. *Annalen der Physik*, 23:848–866, 1907.

[83] JJ Hopfield. Theory of the contribution of excitons to the complex dielectric constant of crystals. *Physical Review*, 112(5):1555, 1958.

[84] Eric Le Ru and Pablo Etchegoin. *Principles of Surface-Enhanced Raman Spectroscopy: and related plasmonic effects*. Elsevier, 2008.

[85] Heinz Raether. Surface plasmons on gratings. *Surface plasmons on smooth and rough surfaces and on gratings*, pages 91–116, 2006.

[86] M Fukui, VCY So, and R Normandin. Lifetimes of surface plasmons in thin silver films. *physica status solidi (b)*, 91(1):K61–K64, 1979.

[87] Dror Sarid. Long-range surface-plasma waves on very thin metal films. *Physical Review Letters*, 47(26):1927, 1981.

[88] L Wendler and R Haupt. Long-range surface plasmon-polaritons in asymmetric layer structures. *Journal of applied physics*, 59(9):3289–3291, 1986.

[89] FY Kou and T Tamir. Range extension of surface plasmons by dielectric layers. *Optics letters*, 12(5):367–369, 1987.

[90] Petter Holmström, Lars Thylén, and A Bratkovsky. Dielectric function of quantum dots in the strong confinement regime. *Journal of Applied Physics*, 107(6):064307, 2010.

[91] JC Maxwell Garnett. Xii. colours in metal glasses and in metallic films. *Philosophical Transactions of the Royal Society of London. Series A, Containing Papers of a Mathematical or Physical Character*, 203(359-371):385–420, 1904.

[92] Ari H Sihvola. *Electromagnetic mixing formulas and applications*. Number 47. Iet, 1999.

[93] John David Jackson. *Classical electrodynamics*. John Wiley & Sons, 2021.

[94] AV Korotun, AA Koval', and IN Titov. Optical absorption of a composite based on bilayer metal–dielectric spherical nanoparticles. *Journal of Applied Spectroscopy*, 87(2):240–248, 2020.

[95] Alexandra Boltasseva and Harry A Atwater. Low-loss plasmonic metamaterials. *Science*, 331(6015):290–291, 2011.

[96] Gururaj V Naik, Vladimir M Shalaev, and Alexandra Boltasseva. Alternative plasmonic materials: beyond gold and silver. *Advanced Materials*, 25(24):3264–3294, 2013.

[97] Peter B Johnson and R-WJPrB Christy. Optical constants of the noble metals. *Physical review B*, 6(12):4370, 1972.

[98] PB Johnson and RW Christy. Optical constants of transition metals: Ti, v, cr, mn, fe, co, ni, and pd. *Physical review B*, 9(12):5056, 1974.

[99] Edward D Palik. *Handbook of optical constants of solids*, volume 3. Academic press, 1998.

[100] Heinz Raether et al. Surface plasmons on smooth and rough surfaces and on gratings [electronic resource].

[101] David Andrews, Gregory Scholes, and Gary Wiederrecht. *Comprehensive nanoscience and technology*. Academic Press, 2010.

[102] Jian-Feng Li, Yue-Jiao Zhang, Song-Yuan Ding, Rajapandiyan Panneerselvam, and Zhong-Qun Tian. Core–shell nanoparticle-enhanced raman spectroscopy. *Chemical reviews*, 117(7):5002–5069, 2017.

[103] Stefan A Maier et al. *Plasmonics: fundamentals and applications*, volume 1. Springer, 2007.

[104] Frederick Wooten. Optical properties of solids. *American Journal of Physics*, 41(7):939–940, 1973.

[105] M Kerker and CG Blatchford. Elastic scattering, absorption, and surface-enhanced raman scattering by concentric spheres comprised of a metallic and a dielectric region. *Physical Review B*, 26(8):4052, 1982.

[106] Alexandre Bouhelier, M Beversluis, Achim Hartschuh, and Lukas Novotny. Near-field second-harmonic generation induced by local field enhancement. *Physical review letters*, 90(1):013903, 2003.

[107] Katrin Kneipp, Harald Kneipp, Irving Itzkan, Ramachandra R Dasari, and Michael S Feld. Surface-enhanced raman scattering and biophysics. *Journal of Physics: Condensed Matter*, 14(18):R597, 2002.

[108] Rajib Ghosh Chaudhuri and Santanu Paria. Core/shell nanoparticles: classes, properties, synthesis mechanisms, characterization, and applications. *Chemical reviews*, 112(4):2373–2433, 2012.

[109] Masoud Salavati-Niasari, Fatemeh Davar, and Mehdi Mazaheri. Preparation of zno nanoparticles from [bis (acetylacetonato) zinc (ii)]–oleylamine complex by thermal decomposition. *Materials Letters*, 62(12-13):1890–1892, 2008.

[110] Masoud Salavati-Niasari, Fatemeh Davar, and Noshin Mir. Synthesis and characterization of metallic copper nanoparticles via thermal decomposition. *Polyhedron*, 27(17):3514–3518, 2008.

[111] Dhruba J Bharali, Ilona Klejbor, Ewa K Stachowiak, Purnendu Dutta, Indrajit Roy, Navjot Kaur, Earl J Bergey, Paras N Prasad, and Michal K Stachowiak. Organically modified silica nanoparticles: a nonviral vector for in vivo gene delivery and expression in the brain. *Proceedings of the National Academy of Sciences*, 102(32):11539–11544, 2005.

[112] Carsten Kneuer, Mohammad Sameti, Udo Bakowsky, Thomas Schiestel, Hermann Schirra, Helmut Schmidt, and Claus-Michael Lehr. A nonviral dna delivery system based on surface modified silica-nanoparticles can efficiently transfect cells in vitro. *Bioconjugate Chemistry*, 11(6):926–932, 2000.

[113] Zheng Li, Shiguo Zhu, Kai Gan, Qiuhong Zhang, Zhaoyang Zeng, Yanhong Zhou, Huaying Liu, Wei Xiong, Xiaoling Li, and Guiyuan Li. Poly-l-lysine-

modified silica nanoparticles: a potential oral gene delivery system. *Journal of Nanoscience and Nanotechnology*, 5(8):1199–1203, 2005.

[114] Shi-Guo Zhu, Juan-Juan Xiang, Xiao-Ling Li, Shou-Rong Shen, Hong-bin Lu, Jie Zhou, Wei Xiong, Bi-Cheng Zhang, Xin-Min Nie, Ming Zhou, et al. Poly (l-lysine)-modified silica nanoparticles for the delivery of antisense oligonucleotides. *Biotechnology and applied biochemistry*, 39(2):179–187, 2004.

[115] Faai Zhang, Yunpu Wang, and Chunpeng Chai. Preparation of styrene-acrylic emulsion by using nano-sio2 as seeds. *Polymer international*, 53(9):1353–1359, 2004.

[116] Shuxue Zhou, Limin Wu, Jian Sun, and Weidian Shen. The change of the properties of acrylic-based polyurethane via addition of nano-silica. *Progress in organic coatings*, 45(1):33–42, 2002.

[117] Libang Feng, Yulong Wang, Na Wang, and Yingxia Ma. Preparation of poly (ethylene glycol)-grafted silica nanoparticles using a facile esterification condensation method. *Polymer bulletin*, 63:313–327, 2009.

[118] Shu-Xue Zhou, Li-Min Wu, Jian Sun, and Wei-Dian Shen. Effect of nanosilica on the properties of polyester-based polyurethane. *Journal of Applied Polymer Science*, 88(1):189–193, 2003.

[119] Ali Reza Mahdavian, Mohsen Ashjari, and Ardavan Bayat Makoo. Preparation of poly (styrene–methyl methacrylate)/sio2 composite nanoparticles via emulsion polymerization. an investigation into the compatiblization. *European polymer journal*, 43(2):336–344, 2007.

[120] Clément Sanchez, Beatriz Julián, Philippe Belleville, and Michael Popall. Applications of hybrid organic–inorganic nanocomposites. *Journal of Materials Chemistry*, 15(35-36):3559–3592, 2005.

[121] Mallika Das, Sawitri Mardyani, Warren CW Chan, and Eugenia Kumacheva. Biofunctionalized ph-responsive microgels for cancer cell targeting: rational design. *Advanced Materials*, 18(1):80–83, 2006.

[122] Zhibing Hu, Yuanye Chen, Changjie Wang, Yindong Zheng, and Yong Li. Polymer gels with engineered environmentally responsive surface patterns. *Nature*, 393(6681):149–152, 1998.

[123] Vladimir M Atanasov. *Core-shell macromolecules with dendritic polyphenylene core and polymer shells*. PhD thesis, Johannes Gutenberg-Universität Mainz, 2004.

[124] P Bouillot and B Vincent. A comparison of the swelling behaviour of copolymer and interpenetrating network microgel particles. *Colloid and Polymer Science*, 278:74–79, 2000.

[125] Nurettin Sahiner, WT Godbey, Gary L McPherson, and Vijay T John. Microgel, nanogel and hydrogel–hydrogel semi-ipn composites for biomedical applications: synthesis and characterization. *Colloid and Polymer Science*, 284:1121–1129, 2006.

[126] Tony Y Zhang. Palladium catalysts immobilized on polymeric supports. *Handbook of Organopalladium Chemistry for Organic Synthesis*, pages 3007–3030, 2002.

[127] Guangfeng Wu, Junfeng Zhao, Haitao Shi, and Huixuan Zhang. The influence of core–shell structured modifiers on the toughness of poly (vinyl chloride). *European polymer journal*, 40(11):2451–2456, 2004.

[128] Shailaja Mahamuni, Amit D Lad, and Shashikant Patole. Photoluminescence properties of manganese-doped zinc selenide quantum dots. *The Journal of Physical Chemistry C*, 112(7):2271–2277, 2008.

[129] Celso de Mello Donegá. Synthesis and properties of colloidal heteronanocrystals. *Chemical Society Reviews*, 40(3):1512–1546, 2011.

[130] Divya Vasudevan, Rohit Ranganathan Gaddam, Adrian Trinchi, and Ivan Cole. Core–shell quantum dots: Properties and applications. *Journal of Alloys and Compounds*, 636:395–404, 2015.

[131] Peter Reiss, Myriam Protiere, and Liang Li. Core/shell semiconductor nanocrystals. *small*, 5(2):154–168, 2009.

[132] Amira R AbouElhamd, Khaled A Al-Sallal, and Ahmed Hassan. Review of core/shell quantum dots technology integrated into buildingâĂŹs glazing. *Energies*, 12(6):1058, 2019.

[133] Sungjee Kim, Brent Fisher, Hans-Jürgen Eisler, and Moungi Bawendi. Type-ii quantum dots: Cdte/cdse (core/shell) and cdse/znte (core/shell) heterostructures. *Journal of the American Chemical Society*, 125(38):11466–11467, 2003.

[134] Margaret A Hines and Philippe Guyot-Sionnest. Synthesis and characterization of strongly luminescing zns-capped cdse nanocrystals. *The Journal of Physical Chemistry*, 100(2):468–471, 1996.

[135] Marie-Christine Daniel and Didier Astruc. Gold nanoparticles: assembly, supramolecular chemistry, quantum-size-related properties, and applications toward biology, catalysis, and nanotechnology. *Chemical reviews*, 104(1):293–346, 2004.

[136] Frank Caruso. Nanoengineering of particle surfaces. *Advanced materials*, 13(1):11–22, 2001.

[137] Suchita Kalele, SW Gosavi, J Urban, and SK Kulkarni. Nanoshell particles: synthesis, properties and applications. *Current science*, pages 1038–1052, 2006.

[138] Srinivasan Balakrishnan, Michael J Bonder, and George C Hadjipanayis. Particle size effect on phase and magnetic properties of polymer-coated magnetic nanoparticles. *Journal of magnetism and magnetic materials*, 321(2):117–122, 2009.

[139] Min-Jung Kim, Yong-Ho Choa, Dong Ho Kim, and Ki Hyeon Kim. Magnetic behaviors of surface modified superparamagnetic magnetite nanoparticles. *IEEE transactions on magnetics*, 45(6):2446–2449, 2009.

[140] Veronica Salgueiriño-Maceira and Miguel A Correa-Duarte. Increasing the complexity of magnetic core/shell structured nanocomposites for biological applications. *Advanced Materials*, 19(23):4131–4144, 2007.

[141] Sumant Phadtare, Ashavani Kumar, VP Vinod, Chandravanu Dash, Dnyaneshwar V Palaskar, Mala Rao, Parshuram G Shukla, Swaminathan Sivaram, and Murali Sastry. Direct assembly of gold nanoparticle âĂIJshellsâĂİ on polyurethane microsphere âĂIJcoresâĂİ and their application as enzyme immobilization templates. *Chemistry of materials*, 15(10):1944–1949, 2003.

[142] AR Kortan, R Hull, Robert L Opila, Moungi G Bawendi, Michael L Steigerwald, PJ Carroll, and Louis E Brus. Nucleation and growth of cdse on zns quantum crystallite seeds, and vice versa, in inverse micelle media. *Journal of the American Chemical Society*, 112(4):1327–1332, 1990.

[143] Limin Qi, Jiming Ma, Humin Cheng, and Zhenguo Zhao. Synthesis and characterization of mixed cdsîŮÿ zns nanoparticles in reverse micelles. *Colloids and Surfaces A: Physicochemical and Engineering Aspects*, 111(3):195–202, 1996.

[144] GH Ma, J He, K Rajiv, SH Tang, Y Yang, and M Nogami. Observation of resonant energy transfer in au: Cds nanocomposite. *Applied physics letters*, 84(23):4684–4686, 2004.

[145] Prashant V Kamat and Bhairavi Shanghavi. Interparticle electron transfer in metal/semiconductor composites. picosecond dynamics of cds-capped gold nanoclusters. *The Journal of Physical Chemistry B*, 101(39):7675–7679, 1997.

[146] P Scodeller, Victoria Flexer, R Szamocki, Ernesto Julio Calvo, N Tognalli, H Troiani, and Alejandro Fainstein. Wired-enzyme core- shell au nanoparticle

biosensor. *Journal of the American Chemical Society*, 130(38):12690–12697, 2008.

[147] Sophie Laurent, Delphine Forge, Marc Port, Alain Roch, Caroline Robic, Luce Vander Elst, and Robert N Muller. Magnetic iron oxide nanoparticles: synthesis, stabilization, vectorization, physicochemical characterizations, and biological applications. *Chemical reviews*, 108(6):2064–2110, 2008.

[148] Lucia Babes, Benoıt Denizot, Gisèle Tanguy, Jean Jacques Le Jeune, and Pierre Jallet. Synthesis of iron oxide nanoparticles used as mri contrast agents: a parametric study. *Journal of colloid and interface science*, 212(2):474–482, 1999.

[149] FD De Menezes, AG Brasil Jr, WL Moreira, LC Barbosa, CL Cesar, R de C Ferreira, PMA De Farias, and BS Santos. Cdte/cds core shell quantum dots for photonic applications. *Microelectronics Journal*, 36(11):989–991, 2005.

[150] Ajay Kumar Gupta and Mona Gupta. Synthesis and surface engineering of iron oxide nanoparticles for biomedical applications. *biomaterials*, 26(18):3995–4021, 2005.

[151] Pierre A Dresco, Vladimir S Zaitsev, Richard J Gambino, and Benjamin Chu. Preparation and properties of magnetite and polymer magnetite nanoparticles. *Langmuir*, 15(6):1945–1951, 1999.

[152] Nagarajan Sounderya and Yong Zhang. Use of core/shell structured nanoparticles for biomedical applications. *Recent Patents on Biomedical Engineering (Discontinued)*, 1(1):34–42, 2008.

[153] Eryun Yan, Yin Ding, Changjing Chen, Rutian Li, Yong Hu, and Xiqun Jiang. Polymer/silica hybrid hollow nanospheres with ph-sensitive drug release in physiological and intracellular environments. *Chemical communications*, (19):2718–2720, 2009.

[154] Jyoti K Jaiswal, Hedi Mattoussi, J Matthew Mauro, and Sanford M Simon. Long-term multiple color imaging of live cells using quantum dot bioconjugates. *Nature biotechnology*, 21(1):47–51, 2003.

[155] Xavier Michalet, Fabien F Pinaud, Laurent A Bentolila, James M Tsay, SJJL Doose, Jack J Li, G Sundaresan, AM Wu, SS Gambhir, and S Weiss. Quantum dots for live cells, in vivo imaging, and diagnostics. *science*, 307(5709):538–544, 2005.

[156] Mrinmoy De, Partha S Ghosh, and Vincent M Rotello. Applications of nanoparticles in biology. *Advanced Materials*, 20(22):4225–4241, 2008.

[157] Shun Lien Chuang. *Physics of photonic devices*. John Wiley & Sons, 2012.

[158] M Kuttge, H Kurz, J Gómez Rivas, JA Sánchez-Gil, and P Haring Bolivar. Analysis of the propagation of terahertz surface plasmon polaritons on semiconductor groove gratings. *Journal of applied physics*, 101(2):023707, 2007.

[159] Paul R West, Satoshi Ishii, Gururaj V Naik, Naresh K Emani, Vladimir M Shalaev, and Alexandra Boltasseva. Searching for better plasmonic materials. *Laser & photonics reviews*, 4(6):795–808, 2010.

[160] Ki Young Kim. *Plasmonics: Principles and Applications*. BoD–Books on Demand, 2012.

[161] Rizia Bardhan, Shaunak Mukherjee, Nikolay A Mirin, Stephen D Levit, Peter Nordlander, and Naomi J Halas. Nanosphere-in-a-nanoshell: a simple nanomatryushka. *The Journal of Physical Chemistry C*, 114(16):7378–7383, 2010.

[162] Corey Radloff and Naomi J Halas. Plasmonic properties of concentric nanoshells. *Nano letters*, 4(7):1323–1327, 2004.

[163] Shizhong Wang, Benjamin R Jarrett, Susan M Kauzlarich, and Angelique Y Louie. Core/shell quantum dots with high relaxivity and photolumines-

cence for multimodality imaging. *Journal of the American Chemical Society*, 129(13):3848–3856, 2007.

[164] HUI Wang, Daniel W Brandl, Peter Nordlander, and Naomi J Halas. Plasmonic nanostructures: artificial molecules. *Accounts of chemical research*, 40(1):53–62, 2007.

[165] Jacek Jasieniak, Jessica Pacifico, Raffaella Signorini, Alessandro Chiasera, Maurizio Ferrari, Alessandro Martucci, and Paul Mulvaney. Luminescence and amplified stimulated emission in cdse–zns-nanocrystal-doped tio2 and zro2 waveguides. *Advanced Functional Materials*, 17(10):1654–1662, 2007.

[166] Ankit Kumar Singh. Effects of surface plasmon excitations on photoluminescence by cdse/zns quantum dots. 2016.

[167] David Hilbert and Stephan Cohn-Vossen. *Geometry and the Imagination*, volume 87. American Mathematical Soc., 2021.

[168] Lev Davidovich Landau, John Stewart Bell, MJ Kearsley, LP Pitaevskii, EM Lifshitz, and JB Sykes. *Electrodynamics of continuous media*, volume 8. elsevier, 2013.

[169] A Sihvola and Ismo V Lindell. Polarizability and effective permittivity of layered and continuously inhomogeneous dielectric ellipsoids. *Journal of electromagnetic waves and applications*, 4(1):1–26, 1990.

[170] Matthew Pelton and Garnett W Bryant. *Introduction to metal-nanoparticle plasmonics*. John Wiley & Sons, 2013.

[171] Jian Feng Li, Yue Jiao Zhang, Song Yuan Ding, Rajapandiyan Panneerselvam, and Zhong Qun Tian. Core-shell nanoparticle-enhanced raman spectroscopy. *Chemical Reviews*, 117(7):5002–5069, 2017.

[172] Rajib Ghosh Chaudhuri and Santanu Paria. Core/shell nanoparticles: Classes,

properties, synthesis mechanisms, characterization, and applications. *Chemical Reviews*, 112(4):2373–2433, 2012.

[173] Ibrahim Khan, Khalid Saeed, and Idrees Khan. Nanoparticles: Properties, applications and toxicities. *Arabian Journal of Chemistry*, 12(7):908–931, 2019.

[174] Alagarsamy Pandikumar, Su Pei Lim, Subramaniam Jayabal, Nay Ming Huang, Hong Ngee Lim, and Ramasamy Ramaraj. Titania@gold plasmonic nanoarchitectures: An ideal photoanode for dye-sensitized solar cells. *Renewable and Sustainable Energy Reviews*, 60:408–420, 2016.

[175] Yujun Song, Yinghui Wang, Shaoxia Ji, and Jie Ding. Shell-driven fine structure transition of core materials in Co@Au core-shell nanoparticles. *Nano-Micro Letters*, 4(4):235–242, 2012.

[176] Kenichi Ikeya, Masatoshi Shimoda, and Jin Xing Shi. Multi-objective free-form optimization for shape and thickness of shell structures with composite materials. *Composite Structures*, 135:262–275, 2016.

[177] Francesco Tornabene, Nicholas Fantuzzi, Michele Bacciocchi, and Rossana Dimitri. Dynamic analysis of thick and thin elliptic shell structures made of laminated composite materials. *Composite Structures*, 133:278–299, 2015.

[178] Sioma Debela, Teshome Senbeta, and Belayneh Mesfin. Plasmon Enhanced Internal Quantum Efficiency of CdSe/ZnS Quantum Dots. *International Journal of Recent advances in Physics*, 5(2):17–24, 2016.

[179] Rachel Woods-Robinson, Yanbing Han, Hanyu Zhang, Tursun Ablekim, Imran Khan, Kristin A. Persson, and Andriy Zakutayev. Wide Band Gap Chalcogenide Semiconductors. *Chemical Reviews*, 120(9):4007–4055, 2020.

[180] Akeel M. Kadim. Zinc Selenide Quantum Dots Light Emitting Devices (ZnSe QDs-LEDs) with Different Organic Polymers. *Nano Hybrids and Composites*, 18:11–19, 2017.

[181] Peter Reiss, Joël Bleuse, and Adam Pron. Highly Luminescent CdSe/ZnSe Core/Shell Nanocrystals of Low Size Dispersion. *Nano Letters*, 2(7):781–784, 2002.

[182] B. Urbaszek, A. Balocchi, C. Bradford, C. Morhain, C. B. O'Donnell, K. A. Prior, and B. C. Cavenett. Excitonic properties of MgS/ZnSe quantum wells. *Applied Physics Letters*, 77(23):3755–3757, 2000.

[183] Soon Ku Hong, Elisabeth Kurtz, Ji Ho Chang, Takashi Hanada, Masaoki Oku, and Takafumi Yao. Low stacking-fault density in ZnSe epilayers directly grown on epi-ready GaAs substrates without GaAs buffer layers. *Applied Physics Letters*, 78(2):165–167, 2001.

[184] Oluwatobi Samuel Oluwafemi, Vuyelwa Ncapayi, Sundararajan Parani, and Ncediwe Tsolekile. Facile Synthesis and Characterization of CdSe/ZnSe Core/Shell and ZnxCd1âĹŠxSe Alloy Quantum Dots via Non-organometallic Route. *Journal of Cluster Science*, 30(1):161–169, 2019.

[185] Yong Ji Lee, Tae Geun Kim, and Yun Mo Sung. Lattice distortion and luminescence of CdSe/ZnSe nanocrystals. *Nanotechnology*, 17(14):3539–3542, 2006.

[186] T W Kim, D C Choo, D U Lee, M Jung, J W Cho, K H Yoo, S Lee, K Y Seo, and J K Furdyna. Microstructural and optical studies of multiply stacked CdSe/ZnSe quantum-dot structures with a large ZnSe spacer thickness. *Solid State Communications*, 122(3-4):229–232, 2002.

[187] Gurvir Kaur and S K Tripathi. Spectroscopic studies of CdSe/ZnSe core/shell nanoparticles. In *AIP Conference Proceedings*, volume 1536, pages 45–46, 2013.

[188] Prashant K Jain, Xiaohua Huang, Ivan H El-Sayed, and Mostafa A El-Sayed. Noble metals on the nanoscale: Optical and photothermal properties and some applications in imaging, sensing, biology, and medicine. *Accounts of Chemical Research*, 41(12):1578–1586, 2008.

[189] Nilesh Kumar Pathak, Nikhil Chander, Vamsi K. Komarala, and R. P. Sharma. Plasmonic Perovskite Solar Cells Utilizing Au@SiO2 Core-Shell Nanoparticles. *Plasmonics*, 12(2):237–244, 2017.

[190] Gashaw Beyene Kassahun. Effect of spacer on size dependent plasmonic properties of triple layered spherical core-shell nanostructure. *AIMS Materials Science*, 7(6):788–799, 2020.

[191] Milton Kerker. *The scattering of light and other electromagnetic radiation*, volume 16. 2013.

[192] Pujuan Ma, Dongliang Gao, Yaxian Ni, and Lei Gao. Enhancement of Optical Nonlinearity by Core-Shell Bimetallic Nanostructures. *Plasmonics*, 11(1):183–187, 2016.

[193] Kinde Yeneayehu, Teshome Senbeta, and Belayneh Mesfin. Enhancement of the optical response of Fe3O4@Ag core-shell nanoparticles. *Physica E: Low-Dimensional Systems and Nanostructures*, 134(March):114822, 2021.

[194] Leta Jule, Vadim Mal'nev, Belayneh Mesfin, Teshome Senbeta, Francis Dejene, and Kittesa Rorro. Fano-like resonance and scattering in dielectric(core)-metal(shell) composites embedded in active host matrices. *Physica Status Solidi (B) Basic Research*, 252(12):2707–2713, 2015.

[195] H Khosravi, N Daneshfar, and A Bahari. Theoretical study of the light scattering from two alternating concentric double silica-gold nanoshell. *Physics of Plasmas*, 17(5), 2010.

[196] Richard D Averitt, Sarah L. Westcott, and Naomi J. Halas. Linear optical properties of gold nanoshells. *Journal of the Optical Society of America B*, 16(10):1824, 1999.

[197] Nader Daneshfar and Khashayar Bazyari. Optical and spectral tunability of multilayer spherical and cylindrical nanoshells. *Applied Physics A: Materials Science and Processing*, 116(2):611–620, 2014.

[198] Maryam Saliminasab, Farzad Shirzaditabar, and Rostam Moradian. Electromagnetic field amplification in Al / Ag spherical nanostructures. *Applied Physics A*, 124(12):1–9, 2018.

[199] G B Kassahun. High Tunability of Size Dependent Optical Properties of ZnO@M@Au (M = SiO2, In2O3, TiO2) Core/Spacer/Shell Nanostructure. *Advanced Nano Research*, 2(1):1–13, 2020.

[200] Farzad Shirzaditabar, Maryam Saliminasab, Borhan Arghavani Nia, Farzad Shirzaditabar, Maryam Saliminasab, and Borhan Arghavani Nia. Triple plasmon resonance of bimetal nanoshell Triple plasmon resonance of bimetal nanoshell. *Physics of plasmas*, 21(7):072102, 2014.

[201] Maryam Saliminasab, Marzieh Afkhami Garaei, and Rostam Moradian. The Effect of Bumpy Structure on Optical Properties of Bimetallic Nanoshells. *Plasmonics*, 12(4):1029–35, 2016.

[202] Sisay Shewamare and V N Malnev. Two optical bistability domains in composites of metal nanoparticles with nonlinear dielectric core. *Physica B: Condensed Matter*, 407(24):4837–4842, 2012.

[203] Wei Lv, Patrick E Phelan, Rajasekaran Swaminathan, Todd P Otanicar, and Robert A Taylor. Multifunctional core-shell nanoparticle suspensions for efficient absorption. *Journal of Solar Energy Engineering, Transactions of the ASME*, 135(2):1–7, 2013.

[204] Shayesteh, S Farjami and Matin Saie. The effect of surface plasmon resonance on optical response in dielectric (core)âĂŞ metal (shell) nanoparticles. *Pramana*, 85(6):1245–1255, 2015.

[205] Westcott, S L, J B Jackson, C Radloff and N. J. Halas. Relative contributions to the plasmon line shape of metal nanoshells. *Physical Review B*, 66(15):155431., 2002.

[206] Ma, Ye-Wan, Zhao-Wang Wu, Li-Hua Zhang, Wan-Fang Liu and Jie Zhang. Theoretical Study of Local Surface Plasmon Resonances on a Dielectric-Ag Core-Shell Nanosphere Using the Discrete-Dipole Approximation Method Theoretical Study of Local Surface Plasmon Resonances on a Dielectric-Ag Core-Shell Nanosphere Using the Discrete. *Chinese Physics Letters*, 32(9):094202, 2015.

[207] Sioma Debela, Belayneh Mes, and Teshome Senbeta. Photonics and Nanostructures - Fundamentals and Applications Surface plasmon resonances in ellipsoidal bimetallic nanoparticles. *Photonics and Nanostructures-Fundamentals and Applications*, 33(November):48–54, 2018.

[208] Sara Abalde-Cela, Paula Aldeanueva-Potel, Cintia Mateo-Mateo, Laura Rodríguez-Lorenzo, Ramón A. Alvarez-Puebla, and Luis M. Liz-Marzán. Surface-enhanced Raman scattering biomedical applications of plasmonic colloidal particles. *Journal of the Royal Society Interface*, 7(SUPPL. 4), 2010.

[209] Mohammad Jafar Molaei. The optical properties and solar energy conversion applications of carbon quantum dots: A review. *Solar Energy*, 196(November 2019):549–566, 2020.

[210] Alexandre G. Brolo. Plasmonics for future biosensors. *Nature Photonics*, 6(11):709–713, 2012.

[211] Gashaw Beyene, Teshome Senbeta, Belayneh Mesfin, Ni Han, Gamachis Sakata, and Qinfang Zhang. Rapid synthesis of triple-layered cylindrical zno@ sio2@ ag core-shell nanostructures for photocatalytic applications. *Journal of Nanoparticle Research*, 22(12):1–14, 2020.

[212] Naomi Halas. Playing with plasmons: Tuning the optical resonant properties of metallic nanoshells. *MRS Bulletin*, 30(5):362–367, 2005.

[213] Cecilia Noguez. Surface plasmons on metal nanoparticles: The influence

of shape and physical environment. *Journal of Physical Chemistry C*, 111(10):3606–3619, 2007.

[214] Fenghong Chu, Yage Zhan, Junjie Yang, and Jiyuan Wang. Using Au/SiO2 core-shell structure to enhance the fluorescence of MEH-PPV in the detection of nitrated aromatic explosives. *Optik*, 124(12):1338–1341, 2013.

[215] Nader Daneshfar. The Study of Scattering-to-absorption Ratio in Plasmonic Nanoparticles for Photovoltaic Cells and Sensor Applications. *Plasmonics*, 16(6):2017–2023, 2021.

[216] Steven J Limmer, Tammy P Chou, and Guozhong Cao. Formation and optical properties of cylindrical gold nanoshells on silica and titania nanorods. *Journal of Physical Chemistry B*, 107(48):13313–13318, 2003.

[217] Reena Reena, Yogita Kalra, and Ajeet Kumar. Ellipsoidal all-dielectric Fano resonant core-shell metamaterials. *Superlattices and Microstructures*, 118:205–212, 2018.

[218] Cheng Sun. On the Plasmonic Properties of Ag@SiO2@Graphene Core-Shell Nanostructures. *Plasmonics*, 13(5):1671–1680, 2018.

[219] Xin Zhang, Yongan Niu, Jiupeng Zhao, and Yao Li. Fabrication, structures and molecule detection of gold films coated on γ-Fe2O3@SiO2 ellipsoid ordered arrays. *Colloids and Surfaces A: Physicochemical and Engineering Aspects*, 520(January):343–347, 2017.

[220] Su Pei Lim, Yee Seng Lim, Alagarsamy Pandikumar, Hong Ngee Lim, Yun Hau Ng, Ramasamy Ramaraj, Daniel Chia Sheng Bien, Osama K. Abou-Zied, and Nay Ming Huang. Gold-silver@TiO2 nanocomposite-modified plasmonic photoanodes for higher efficiency dye-sensitized solar cells. *Physical Chemistry Chemical Physics*, 19(2):1395–1407, 2017.

[221] Kun Liu, Xin Xu, Wen Shan, Di Sun, Chengbao Yao, and Wenjun Sun. Study on third-order nonlinear optical properties of the composite films with Ag nanoparticles and CdSe quantum dots. *Optical Materials*, 99(December 2019):109569, 2020.

[222] Ling Liu, Xiaoliang Xu, Yanxia Ye, Yaping Ma, Yansong Liu, Jiemei Lei, and Naiqiang Yin. Electrolysis synthetic silver nanoparticles enhanced light emission from CdSe quantum dots. *Thin Solid Films*, 526:127–132, 2012.

[223] Gashaw Beyene, Gamachis Sakata, Teshome Senbeta, and Belayneh Mesfin. Effect of core size/shape on the plasmonic response of spherical zno@ au core-shell nanostructures embedded in a passive host-matrices of mgf 2. *AIMS Mater Sci*, 7:705–719, 2020.

[224] J L Casas Espínola and X A Hernández Contreras. Effect of dielectric constant on emission of CdSe quantum dots. *Journal of Materials Science: Materials in Electronics*, 28(10):7132–7138, 2017.

[225] Ho Seong Jang, Byoung Hwa Kwon, Heesun Yang, and Duk Young Jeon. Bright three-band white light generated from CdSe/ZnSe quantum dot-assisted Sr3 SiO5: Ce3+, Li+ -based white light-emitting diode with high color rendering index. *Applied Physics Letters*, 95(16):10–13, 2009.

[226] Koichi Okamoto, Saurabh Vyawahare, and Axel Scherer. Surface plasmon enhanced light emission from CdSe quantum dot nanocrystals. In *Optics InfoBase Conference Papers*, volume 23, pages 1674–1678, 2006.

[227] Tong Tong Jiang, Wei Jia Shao, Nai Qiang Yin, Ling Liu, Jiang Lu Qi Song, Li Xin Zhu, and Xiao Liang Xu. Enhanced photoluminescence of CdSe quantum dots by the coupling of Ag nanocube and Ag film. *Chinese Physics B*, 23(8), 2014.

[228] Tayebeh Naseri, Nader Daneshfar, Milad Moradi-Dangi, and Fereshteh Eynipour-Malaee. Terahertz optical bistability of graphene-coated cylindri-

cal coreâĂŞshell nanoparticles. *Journal of Theoretical and Applied Physics*, 12(4):257–263, 2018.

[229] Jian Zhu, Jian Jun Li, and Jun Wu Zhao. Improve the refractive index sensitivity of coaxial-cable type gold nanostructure: The effect of dielectric polarization from the separate layer. *Journal of Nanoparticle Research*, 15(6), 2013.

[230] Jian Zhu, Jian Jun Li, and Jun Wu Zhao. Local dielectric environment dependent local electric field enhancement in double concentric silver nanotubes. *Journal of Physical Chemistry C*, 117(1):584–592, 2013.

[231] Jayanta K. Majhi, Atis C. Mandal, and Probodh K. Kuiri. Theoretical calculation of optical absorption of noble metal nanoparticles using a simple model: Effects of particle size and dielectric function. *Journal of Computational and Theoretical Nanoscience*, 12(10):2997–3005, 2015.

[232] Jian Zhu and Xing-chun Deng. Improve the refractive index sensitivity of gold nanotube by reducing the restoring force of localized surface plasmon resonance. *Sensors and Actuators B: Chemical*, 155(2):843–847, 2011.

[233] A A Ismail, A V Gholap, and Y A Abbo. Enhancement of local electric field in core-shell orientation of ellipsoidal metal/dielectric nanoparticles. *Condensed Matter Physics*, 20(2):1–11, 2017.

[234] Vollmer Michael Uwe Kreibig. *Optical properties of metal clusters.* Number July. Springer, 2013.

[235] Nikolai G Khlebtsov and Lev A Dykman. Optical properties and biomedical applications of plasmonic nanoparticles. *Journal of Quantitative Spectroscopy and Radiative Transfer*, 111(1):1–35, 2010.

[236] Nilesh Kumar Pathak, Gyanendra Krishna Pandey, Alok Ji, and R P Sharma. Study of Light Extinction and Surface Plasmon Resonances of Metal Nanocluster: a Comparison Between Coated and Non-coated Nanogeometry. *Plasmonics*, 10(6):1597–1606, 2015.

[237] Richa Sharma, Sangita Roopak, Nilesh kumar Pathak, R Uma, and R P Sharma. Numerical Simulation of Electromagnetic Wave Interaction with Spheroidal Core-Shell Nanoparticle: Dependence of Surface Plasmon Resonance on Core-Shell Composition. *Plasmonics*, 13(1):335–343, 2018.

[238] Mingzhao Liu and Philippe Guyot-Sionnest. Synthesis and optical characterization of Au/Ag core/shell nanorods. *Journal of Physical Chemistry B*, 108(19):5882–5888, 2004.

[239] Mingzhao Liu and Philippe Guyot-Sionnest. Preparation and optical properties of silver chalcogenide coated gold nanorods. *Journal of Materials Chemistry*, 16(40):3942–3945, 2006.

[240] Hui Wang, Daniel W Brandl, Fei Le, Peter Nordlander, and Naomi J Halas. Nanorice: a hybrid plasmonic nanostructure. *Nano letters*, 6(4):827–832, 2006.

[241] Mina Piralaee, A Asgari, and V Siahpoush. Plasmonic properties of spheroid silicon-silver nanoshells in prolate and oblate forms. *Optik*, 172:1064–1068, 2018.

[242] Jian Zhu, Li-na Meng, Guo-jun Weng, Jian-jun Li, and Jun-wu Zhao. Tuning quadruple surface plasmon resonance in gold nanoellipsoid with platinum coating: from ultraviolet to near infrared. *Applied Physics A*, 127(8):1–10, 2021.

[243] Jian Zhu, Fan Zhang, Jian-Jun Li, and Jun-Wu Zhao. Optimization of the refractive index plasmonic sensing of gold nanorods by non-uniform silver coating. *Sensors and Actuators B: Chemical*, 183:556–564, 2013.

[244] Jian Zhu and Shu-min Zhao. Plasmonic refractive index sensitivity of ellipsoidal al nanoshell: Tuning the wavelength position and width of spectral dip. *Sensors and Actuators B: Chemical*, 232:469–476, 2016.

[245] Nilesh Kumar Pathak, Alok Ji, and RP Sharma. Tunable properties of surface plasmon resonances: the influence of core–shell thickness and dielectric environment. *Plasmonics*, 9(3):651–657, 2014.